

Title	Structural studies of macromolecular assemblies using cryo-electron microscopy: Hierarchical assembly of the virus and the drug efflux mechanism of the multidrug efflux pump
Author(s)	堤, 研太
Citation	大阪大学, 2019, 博士論文
Version Type	VoR
URL	https://doi.org/10.18910/72674
rights	
Note	

Osaka University Knowledge Archive : OUKA

<https://ir.library.osaka-u.ac.jp/>

Osaka University

Structural studies of macromolecular assemblies
using cryo-electron microscopy:
Hierarchical assembly of the virus and
the drug efflux mechanism of the multidrug efflux pump

A doctoral thesis

By

Kenta Tsutsumi

Submitted to the Graduate School of Science

Osaka University

Japan

February, 2019

Structural studies of macromolecular assemblies
using cryo-electron microscopy:
Hierarchical assembly of the virus and
the drug efflux mechanism of the multidrug efflux pump

(クライオ電子顕微鏡による生体超分子の構造研究:
階層的なウイルスの形成機構と多剤排出ポンプの薬剤排出機構)

A doctoral thesis

By

Kenta Tsutsumi

Submitted to the Graduate School of Science

Osaka University

Japan

February, 2019

Acknowledgements

This study has been carried out in the Laboratory of Supramolecular Crystallography in Institute for Protein Research, Osaka University. First of all, I would like to express my heartfelt thanks to my supervisor, Prof. Atsushi Nakagawa and Associate Prof. Eiki Yamashita for their incessant guidance and encouragement throughout this study.

I would thank Prof. Genji Kurisu of Institute for Protein Research, Osaka University and Prof. Katsumi Imada of Osaka university for their suggestive comments.

I would like to express my deep appreciation for Dr. Ryo Yonehara and Dr. Etsuko Ishizaka-Ikeda from Laboratory of Supramolecular Crystallography to provide the data of functional analysis for MexAB–OprM. I express my sincere thanks to Prof. Kenji Iwasaki of University of Tsukuba Life Science Center, Dr. Naoyuki Miyazaki and Dr. Shintaro Maeda for supporting my cryo-electron microscopy work. I also want to thank Assistant Prof. Akifumi Higashiura, Dr. Yusuke Nakamichi, Dr Hirotaka Narita and Associate Prof. Kazuyoshi Murata of National Institute for Physiological Sciences for their helpful suggestion and supporting throughout the *Rice Dwarf Virus* study.

I am grateful to past and present members of Laboratory of Supramolecular Crystallography for their helpful advice and supporting my daily research life. Finally, I really thank my parents for their understanding and supports.

Kenta Tsutsumi

February 2019

Table of Contents

Acknowledgements

Table of Contents

Abbreviations

Chapter 1. General introduction	1
1.1 Cryo-electron microscopy	1
1.2 Single-particle analysis and three-dimensional reconstruction	2
1.3 Phase-contrast electron microscopy	3
1.4 The outline of this doctoral thesis	4
 Chapter 2. An Assembly Intermediate Structure of Rice Dwarf Virus Reveals a Hierarchical Outer Capsid Shell Assembly Mechanism	 6
2.1 Introduction	7
2.1.1 The classification for reoviruses and the futures of their capsids	7
2.1.2 The outline of this study	10
2.1.3 The structure of RDV and the strategy of this study	10
2.2 Material and method	15
2.2.1 Preparation of RDV, RDV Inner Shell Particle, and Native P8	15
2.2.2 Expression and Purification of P8-GFP	15
2.2.3 Binding of Native and Fusion P8-trimers on the Inner Shell Particles	16
2.2.4 Cryo-EM and 3D Reconstruction	16
2.2.5 High Resolution Cryo-EM and 3D Reconstruction	19

2.3 Results	23
2.3.1 Preparation of RDV Assembly Defect P8 Mutant Protein	23
2.3.2 Preparation of the Inner Shell Particle and the Native P8 Trimer from RDV Virion	24
2.3.3 Binding of P8 Trimer and P8-GFP Trimer to the Inner-Particle Layer	25
2.3.4 Structural Analysis by Conventional Cryo-electron Microscopy	28
2.3.5 Structural Analyses by Cryo-EM Equipped with Phase Plates	32
2.4 Discussion	36
2.5 Conclusion	38
 Chapter 3. Structures of the wild-type MexAB–OprM tripartite pump reveal its complex formation and drug efflux mechanism.	 40
3.1 Introduction	41
3.1.1 RND-type Multidrug efflux pump	41
3.1.2 The outline of this study	43
3.2 Material and method	44
3.2.1 Expression and purification of MexA, MexB and OprM	44
3.2.2 Reconstruction of MexAB–OprM	46
3.2.3 Detergents removal and replacement with Amphipol	46
3.2.4 Negative-stain electron microscopy single-particle analysis	47
3.2.5 TEM data acquisition	47
3.2.6 Image processing and 3D reconstruction	49
3.2.7 Model building, map sharpening, and structural validation	53
3.3 Results	54

3.3.1 Structural determination and overall structure of apo-state MexAB–OprM	54
3.3.2 Interaction between OprM and MexA	60
3.3.3 Interaction between each MexA protomer	63
3.3.4 Interaction between MexA and MexB	64
3.3.5 Comparison between the closed and open structures of OprM	66
3.3.6 Comparison between the crystal structure and Cryo-EM structure of MexB	67
3.3.7 MexAB–OprM in the presence of drug	71
3.4 Discussion	75
3.5 Conclusion	80
3.6 Supplementary information	82
3.6.1 Supplementary methods	82
3.6.2 Supplementary figures	82
Reference	90
List of publications	

Abbreviations

2D	two dimensional
3D	three dimensional
ABPC	ampicillin
AcrA	Acridine resistance protein A
AcrB	Acridine resistance protein B
BTV	Bluetongue virus
CCD	charge-coupled device
CP	chloramphenicol
Cryo-EM	cryo electron microscopy
CTF	contrast transfer function
Cymal-7	7-cyclohexyl-1-heptyl- β -D-maltoside
DDM	<i>n</i> -dodecyl- β -D-maltoside
dsRNA	double-stranded RNA
EGFP	enhanced green fluorescent protein
EM	erythromycin
EMDB	Electron Microscopy Data Bank
GFP	green fluorescent protein
HEPES	4-(2-hydroxyethyl)-1-piperazineethanesulfonic acid
IPTG	isopropyl β -D-1-thiogalactopyranoside
MexA	Multidrug efflux component A
MexB	Multidrug efflux component B
MFP	membrane fusion protein

MINO	minocycline
NOV	novobiocin
OG	<i>n</i> -octyl- β -D-glucoside
OMF	outer membrane factor
OprM	Outer membrane protein M
PAGE	polyacrylamide gel electrophoresis
PBS	phosphate-buffered saline
PCR	polymerase chain reaction
PDB	Protein Data Bank
PEG	polyethylene glycol
PMSF	phenylmethylsulfonyl fluoride
PSF	point spread function
R6G	rhodamine 6G
RDV	<i>rice dwarf virus</i>
RELION	REGularised LIkelihood Optimisation
RND	resistance nodulation cell division
SDS	sodium dodecyl sulfate
SEC	size exclusion chromatography
S/N	signal-to-noise
TEM	transmission electron microscope

Chapter 1. General Introduction

1.1 Cryo-electron microscopy

Since the inside of the electron microscope is a vacuum, biomolecules must be embedded in something that hinders evaporation in order to observe hydrated specimens. Among the methods to observe biomolecules with an electron microscopy, the first method developed was a negative staining method to embed it in a heavy metal salt solution such as uranyl acetate¹. This method is widely used as a simple sample observation method because it gives high contrast to the sample, but there is a problem that the original structure of the sample is destroyed by staining. The first method without staining is the glucose embedding method developed for the structural analysis of protein 2D crystals in 1975², and the 2D crystal structure of bacteriorhodopsin at atomic resolution has been reported³. However, since the scattering density of glucose is close to that of protein, the contrast is very poor and it is not suitable for observation other than 2D crystals. Cryo-EM is a technique developed in 1980's: a sample is embedded into vitreous ice and observed at a cryogenic temperature^{4,5}. Although samples can be observed in a state close to the solution state by this method, biomolecules are easily disintegrated by electron beams, so observation with very weak electron beams is required. As a result, the contrast of acquired images is poor and the S/N ratio becomes bad. Since the contrast of Cryo-EM is mostly due to the phase contrast, it is necessary to increase the defocus amount at the time of photographing, and as a result, the acquired image is subject to strong modulation. Therefore, it is necessary to correct the modulation for the interpretation of the image. The modulation can be expressed by the convolution of a true image and PSF, and in the actual correction calculation, the calculation is performed by estimating the CTF obtained by

Fourier transforming the PSF. Furthermore, since the image obtained by the TEM becomes a projected image, image analysis is required to obtain the three-dimensional structure of the specimen⁶.

1.2 Single-particle analysis and three-dimensional reconstruction

Single-particle analysis is an image analysis method developed in the 1970's^{7,8}. The biomacromolecules which are spread on the grid and vitrified randomly face various directions ideally. The signal of the particles can be increased by cutting out the parts of particles from a number of TEM images and classified and averaged for each direction, while the background noise is reduced. Further, by determining the Euler angles of each projected images for the 3D reference structure, it is possible to obtain a 3D structure by back-projection⁹. Through this technique, 3D structures of relatively large biomacromolecules such as viruses^{10,11} and ribosomes^{12,13} have been mainly obtained from TEM images. However, it is a problem that the resolution of this method is relatively poor compared with other structural analysis techniques such as X-ray crystallography and NMR because the sample moves when electron beam is applied. Moreover, the size of protein is smaller, the contrast of the particle becomes worse, making the analysis difficult. Moreover, it was difficult to analyze a membrane protein by this method at a sufficient resolution because a density of detergent which solubilized a membrane protein made correct alignments difficult. Therefore, it was difficult to obtain the 3D structure with near atomic resolution, except for highly symmetric viruses¹⁴ or helical filaments¹⁵.

In recent years, development of a direct electron detector has made it possible to detect electrons with high S/N ratio, and it has become possible to record images at a very fast frame rate. It has become possible to record movies at a fast frame rate, so that blur of

particles can be corrected by calculation. Moreover, there was also development of an electron microscope with automatic measurement function specialized for large volume acquisition of images¹⁶ and evolution of single-particle analysis software¹⁷. Due to these evolution of techniques, the resolution has dramatically improved, and a structural analysis at resolution of 2 Å has been reported^{18,19}. Also, the lower limit of sample size that can be analyzed has been improved to about 100 kDa²⁰, and structural analysis with near atomic resolution of membrane protein with about 200 kDa mass without symmetry has been reported²¹.

1.3 Phase-contrast electron microscopy

The poor image contrast is one of the drawbacks of Cryo-EM, which is attributable to the fact that CTF is a sine wave. This is due to the low frequency component greatly affecting the contrast. Therefore, by shifting the phase by a quarter wavelength, CTF becomes a cosine function, and the contrast of the low frequency component can be restored. A material that enables such conversion is called a phase plate, and the first one developed is the Zernike phase plate comprising a carbon thin film with a central pinhole²². Transmitted electrons focused at the back focal plane pass through the center hole and therefore do not suffer phase shift. On the other hand, elastic scattering electrons generated when an electron beam passes through a rapidly frozen biological sample do not change in wavelength as compared to transmitted electrons, but the phase is delayed by a quarter wavelength. Then, the elastic scattered electrons are further delayed by a phase of 1/4 wavelength by passing through the phase plate without being converged at the back focal plane, and as a result, on the imaging plane, the interference is caused by the elastic scattered electrons that have passed through, resulting in contrast. However, there is a disadvantage that it is difficult to match the focal position

of the transmission hole with the central hole of the Zernike phase plate. The recently developed Volta phase plate generates a phase difference between transmitted electrons and elastically scattered electrons by utilizing the property that a carbon thin film is negatively charged by irradiating an electron beam to a heated carbon thin film²³. This method, which is more stable than a Zernike phase plate for a long period of use, is particularly effective for single-particle analysis of small proteins. Recently, the structure analysis of relatively smaller proteins below 100 kDa with near atomic resolution has been reported²⁴.

1.4 The outline of this doctoral thesis

With such evolution, single-particle analysis using cryo-EM becomes a powerful tool for structural determination of biological macromolecules. Even if samples with various conformations are applied, it is possible to analyze multiple conformations by separating the particles in each state by classification. This is a major advantage not applicable in X-ray crystallographic analysis requiring high quality crystals and in NMR in which the resolution of signal largely depends on sample homogeneity. In this doctoral thesis, I describe two themes using Cryo-EM single-particle analysis. The first one is a study on the virus self-assembly mechanism wrote in Chapter 2. In this study, the benefits of single-particle analysis are fully utilized which make it possible to reconstruct the 3D overall structure even at low resolution. The results of this study revealed how viruses with double-layered capsid form their ordered outer capsids. Moreover, the phase-contrast Cryo-EM has demonstrated its power to analyze the intermediate structure at the outer capsid formation of the virus. The second one is a study on the fully assembled multidrug efflux pump of gram-negative bacteria wrote in Chapter 3. In the structural analysis of this study, the feature of single-particle analysis

was demonstrated which even non-homologous samples can be divided and analyzed separately. This study revealed detailed interactions between each protein constituting of the pump and the mechanism of complex formation, and proposed new insights into the drug elimination mechanism.

Chapter 2.

An Assembly Intermediate Structure of *Rice Dwarf Virus* Reveals a
Hierarchical Outer Capsid Shell Assembly Mechanism

2.1 Introduction

2.1.1 The classification for reoviruses and the futures of their capsids

Accurate assembly of virus particles is essential for their replication and subsequent infection to host cells. Viruses in the family *Reoviridae* (reoviruses), the largest family among the dsRNA viruses, have a wide host range that includes humans, animals, plants, insects, fish, and fungi, with nearly all displaying the characteristic feature of complex concentric multi-layered capsids (except for the single-layered *Cypovirus* and *Dinovernavirus*)^{14,25}. In all reoviruses, the innermost first capsid layer consists of 120 copies of a thin crescent-like protein with a $T = 1$ lattice, with each subunit displaying similar overall shape and a conserved $\alpha + \beta$ fold^{26–30}. The asymmetric unit of the first capsid layer in the $T = 1$ lattice consists of a homo-dimer, in which two monomers are in different conformations. This first capsid layer is highly conserved in almost all dsRNA viruses and particularly in the reoviruses and responsible for enclosing the viral genome along with enzymes required for facilitating their transcription, suggesting that these dsRNA viruses have evolved from a common ancestor with a simple single-layered capsid^{31–33}. Fungal dsRNA viruses in the family *Totiviridae* (the most primitive dsRNA viruses) only possess this conserved first capsid layer, and the situation may explain their lack of an extracellular phase to their life cycle^{34,35}. Presumably, the evolutionary acquirement, by the *Reoviridae*, of an additional one or two outer capsid layers (known as second and third layers) has facilitated the cell adhesion and invasion steps associated with their more complex life cycles. Reoviruses are further categorized into two subfamilies (*Sedoreovirinae* and *Spinareovirinae* subfamilies) according to structural features of the second capsid layers. Although the second capsid layer in both subfamilies consists of tightly bound trimeric proteins,

viruses in the *Sedoreovirinae* subfamily (sedoreoviruses; *Orbivirus*, *Rotavirus*, and *Phytoreovirus*) have a complete $T = 13$ second capsid layer composed of 260 copies of a protein trimer, whereas viruses in the *Spinareovirinae* subfamily (spinareoviruses; *Orthoreovirus*, *Aquareovirus*, and *Oryzavirus*) have an incomplete $T = 13$ second capsid layer in which five trimers around 12 icosahedral vertices are replaced with pentameric RNA-capping enzymes forming turrets on the capsid (200 trimers and 12 pentamers). In terms of maturation process, logically, the second viral capsid layer should, in principle, be created after the formation of the first layer. Toward this point, it has been demonstrated that the proteins of the first capsid layer have an intrinsic ability to form the single-layered capsid, whereas the outer capsid proteins have an obligate requirement to bind to the single-layered capsid prior to second-layer assembly^{36,37}. In the case of the sedoreoviruses, the five icosahedrally independent trimers that exist in the second capsid, sit on the first capsid layer at five different sites (designated P, Q, R, S, and T -trimers). Slight structural variations (induced fits) in the second-layer trimeric proteins have been observed at the inter-capsid molecular interface because of the symmetry mismatch between the first $T = 1$ and second $T = 13$ icosahedral lattices²⁸. This observation raises interesting scientific questions as to both how the trimers of the second layer recognize their positions in the capsid and how the symmetry mismatched multi-layered capsid is accurately assembled.

With regard to these questions, the assembly mechanism of the multi-layered capsid of the sedoreoviruses has been examined by X-ray crystallography and Cryo-EM^{26,28,38}. Atomic structures of the double-layered capsid of BTV²⁶ (genus *Orbivirus*) and RDV (genus *Phytoreovirus*)²⁸ strongly suggested that the T trimers attach tightly to the first capsid layer along the icosahedral three-fold axis. This inference was based on the fact

that the symmetry of the two capsid layers match at that point and the averaged B-factor of each second-layer trimer increases with trimer distance from the icosahedral 3-fold axis. Furthermore, in the case of RDV, the T-type P8 trimer makes the strongest and largest molecular interaction with the first capsid layer, whereas the P-type P8 trimer, which binds around the icosahedral 5-fold axis makes the weakest interaction^{28,39}. Supporting this observation, the T trimers of RDV are resistant to high salt concentrations of MgCl_2 ⁴⁰, whereas the P trimers of BTV are unstable and are often missing from recombinant double-layered particles⁴¹. Based on these observations, the stable T trimers seem capable of acting as nucleation centers for second capsid layer formation. In addition, trimers of the second capsid layer have an intrinsic ability to form hexagonal array structures such as planar two-dimensional or tubular crystals^{39,42–44} similar to that found in the icosahedral form of the virion. Therefore, it was starting hypothesis that binding of T trimers to the first capsid layer initiates the formation of a hexagonal lattice leading to the complete $T = 13$ second capsid layer via lateral inter-trimer interactions. I further hypothesized that the orientation of the T defines the other trimer positions (P, Q, R, and S trimers) on the capsid. However, this proposed hierarchical assembly pathway⁴⁵ has not yet been experimentally proven due to a lack of direct evidence demonstrating (1) that trimers forming the second capsid layer recognize the T-trimer position at the icosahedral 3-fold axis, and (2) that T-trimer binding acts to nucleate the binding of the other trimers. To complicate matters somewhat, since the trimers in the second layer attach to the inner capsid proteins with induced fits at the molecular interface, it is impossible to completely exclude the possibility that the trimers may recognize different sites from the T-trimer position

and/or recognize the detailed sites with non-symmetry defined sites on the outer surface of the first capsid layer.

2.1.2 The outline of this study

To answer these questions, I prepared an artificial assembly intermediate particle of RDV stalled at the second capsid formation stage and then determined the 3D structure of this stalled intermediate by Cryo-EM single-particle analysis using a Cryo-EM equipped with phase plates. The high-contrast Cryo-EM imaging possible with the use of phase plate technology^{23,46} enabled categorical assignment of the hierarchical mechanism of assembly of the second capsid layer of RDV and thus, by inference, the likely mechanism adopted by all members of the Reoviridae family.

2.1.3 The structure of RDV and the strategy of this study

The first and second capsid layers of RDV are respectively composed of 120 copies of P3 proteins and 260 copies of P8 trimers (Figures 2-1 A and B). The P8 trimers may be located at five distinctive surface position types of the first capsid layer, designated as P, Q, R, S, and T trimers (Figure 2-1 B). It can be noted from the 3D structure (Figure 2-1 C) that the bottom surface of the P8 trimer is involved in determining the interlayer interactions between the first and second capsid layers, whereas the side surfaces of the P8 trimer are involved in determining the inter-trimer interactions which define the extent of lateral stabilization afforded to the second capsid layer. With particular regard to the inter-layer interaction strength, I note currently available information as follows: the N-terminal $\alpha 1$ - $\alpha 2$ and $\alpha 2$ - $\alpha 3$ loops (29–33

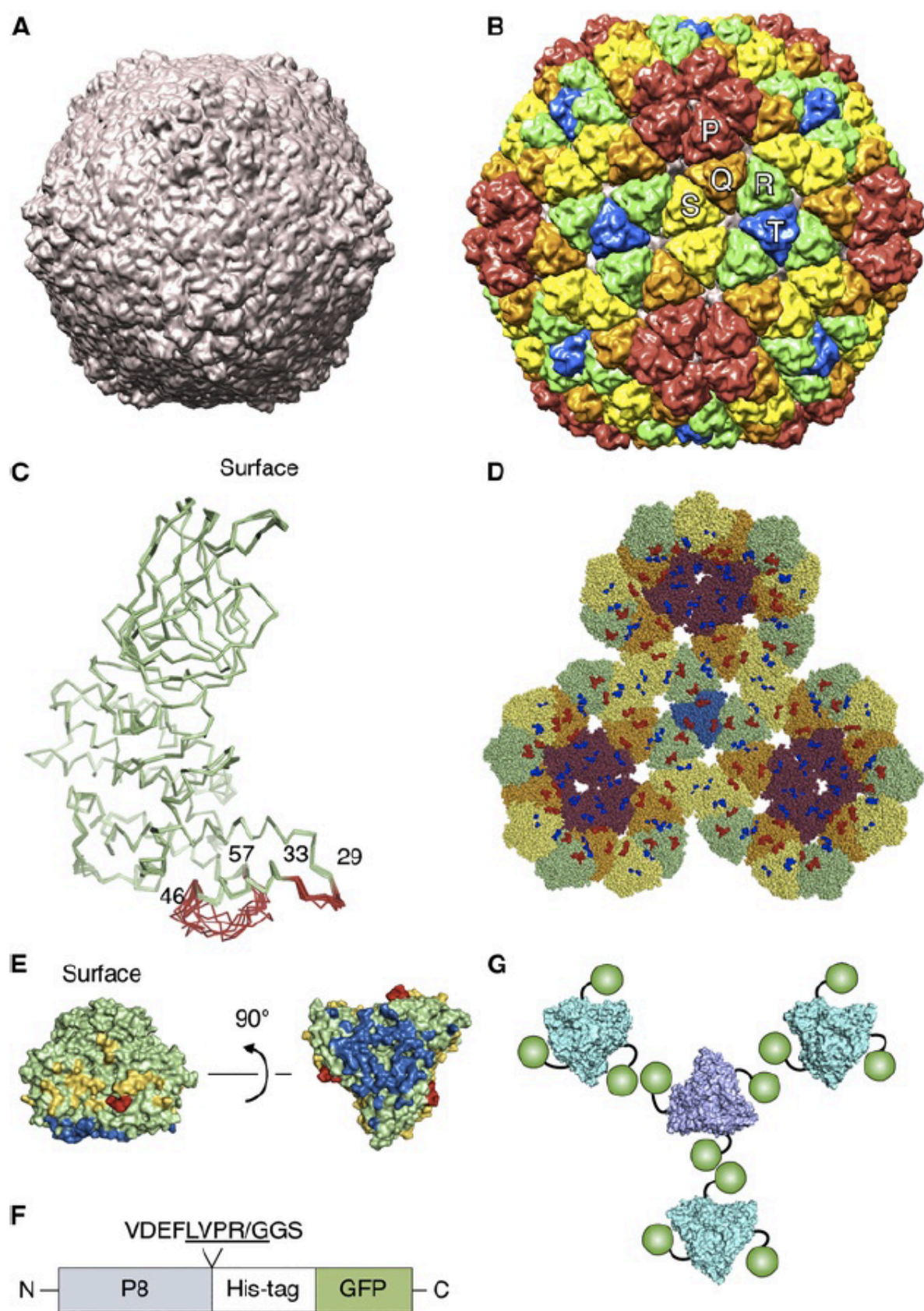


Figure 2-1 The Structure of RDV

(A) The structure of the RDV first capsid layer consisting of 120 copies of the P3 protein. The capsid has icosahedral $T = 1$ symmetry. (B) The structure of the RDV second capsid layer formed from 260 copies of the P8 trimer. P8 trimers are designated P (shown in red), Q (orange), R (green), S (yellow), and T (blue), respectively. (C) Conformational changes in the N-terminal loop region of the P8 outer capsid protein in particle of RDV. Green ribbon models show the superimposition of 13 independent P8 outer capsid proteins. The regions colored in red are the N-terminal loops that can undergo conformational change. Numbers represent the position of the amino acid in the P8 protein chain. (D) The distribution of the N-terminal loops. P8 trimers on the first capsid layer at the icosahedral 3-fold axis are viewed from the central origin of the virus particle (P, Q, R, S, and T trimers are shown in Figure 2-1 B). A red object shows the main region (an amino acid numbering of P8 molecule from 46 to 57) of the induced-fit loop and a blue object shows the partial residues of the disordered loop region. (E) Interfaces among P8 trimers (intra) and between P8 trimers and the first capsid layer (inter) are indicated as yellow and blue, respectively. Red shows C-terminal end of P8. (F) Schematic illustration of the domain structure of the P8-GFP fusion construct. Amino acid sequence between P8 and poly-histidine tag is shown. Underline and slash indicate thrombin recognition and cleavage site, respectively. (G) Schematic of the rationale for interrupting inter P8-trimer interactions using a GFP fusion at the P8-C-terminal. Green circles show GFP inhibiting lateral interactions between P8 trimers.

and 46–57 residues, respectively) are capable of undergoing induced fits with the first capsid layer to maximize the extent of interaction in slightly different manners (Figure 2-1 C), even to the point of being disordered in some trimers (Figure 2-1 D). Seven of the possible 15 different P8 loop regions located within residues 46 to 57 of each monomer in the five structurally independent types of trimers, are disordered with eight loops being structured according to an induced-fit paradigm, with the breakdown as follows: P trimer (three loops disordered [residues 48–54, 49–54, and 50–53], no

ordered loops), Q trimer (one loop disordered [residues 47–53], two loops ordered), R trimer (one loop disordered [residues 49–52], two loops ordered), S trimer (two loops disordered [residues 51–52 and 48–55], one loop ordered), T trimer (three loops ordered). The loops, enable to approach the surface of the core capsid, make induced-fit but other loops, unable to approach the surface of the core capsid, are disordered. The intra-layer lateral interactions of the second capsid layer are mediated by residues located on the side surfaces of the P8 trimer (Figure 2-1 E).

I hypothesized that inhibition of the inter-trimer interactions might provide insight into the relative strengths of the different modes of inter-layer molecular recognition between the P8 trimers and the first capsid layer by producing assembly intermediate particles stalled at an initial step(s) of second capsid layer assembly. However, since P8 trimers closely interact with their neighbors over a large contact interface, it is difficult to interrupt their interactions by site-directed mutation (Figure 2-1 E). Indeed, the P8 trimer of *Rice gall dwarf virus*, which has an amino acid sequence identity to RDV of 51% (but which has a similar surface distribution of electrostatic potential) can successfully interact with the RDV P8 trimer in the second capsid layer^{37,47}. Such a demonstration of hetero second-layer capsid formation strongly indicates that inter-trimer interactions could be maintained even if some amino acid residues were substituted. With these complications in mind, to interrupt the inter-trimer interactions, I decided to modify the C-terminal end of the P8 protein, which is both proximally close to the interface between P8 trimers and distant from the interaction sites between the P8 trimer and the inner capsid P3 protein (Figure 2-1 E, highlighted in red). Due to its positioning, I hypothesized that introducing a protein tag to the C-terminal end of P8 would not impede the molecular interactions between the P8 trimer and the inner capsid

layer of P3 but would impede further outer capsid assembly via the inter-trimer interactions. To test this hypothesis, I designed and produced a construct of P8 containing a GFP tag at the C-terminal to interrupt the inter-trimer interactions (Figures 2-1 F and G).

2.2 Material and method

2.2.1 Preparation of RDV, RDV Inner Shell Particle, and Native P8

Intact double-layered RDV virions were purified as described previously⁴⁸ with the following exceptions. Native outer capsid P8-trimers were disassembled from the intact RDV particles in a high magnesium histidine buffer (1.7 M MgCl₂, 100 mM histidine, pH 6.0), and the resultant single-layered RDV particles and native P8-trimers were isolated by SEC (HiLoad 16/600 Superdex 200 pg, GE Healthcare) equilibrated with the same high magnesium histidine buffer. After the SEC step, single-layered RDV particles were collected by centrifugation at $200,000 \times g$ for 10 min at 4°C (S100AT4, Hitachi) and the precipitant containing the single-layered particles was suspended in PBS at pH 7.4. To completely remove any unbound P8-trimer from the solution, these particles were once again subjected to another round of centrifugation at $200,000 \times g$ for 10 min at 4°C (S100AT4). Precipitant from this second round of centrifugation (containing single-layered RDV particles) was resuspended in PBS. Native P8-trimers isolated from the particles by size exclusion chromatography were collected and dialyzed against PBS.

2.2.2 Expression and Purification of P8-GFP

An RDV P8 protein with a poly-histidine tagged EGFP⁴⁹ described henceforth as the RDV-P8 GFP fusion construct (P8-GFP) was cloned into the vector pFastbac1 (Thermo Fisher Scientific). A poly-histidine EGFP tag was added to the C-terminal end of P8. A thrombin recognition sequence was inserted between the P8 and poly-histidine-EGFP. The P8-GFP fusion protein was produced in Sf9 cells using the Bac-to-Bac Baculovirus Expression System (Thermo Fisher Scientific). Cells expressing P8-GFP were collected by centrifugation, re-suspended in a solution containing 50 mM imidazole, 150 mM

NaCl, and 50 mM Tris-HCl (pH 7.5) and disrupted by sonication. After centrifugation the supernatant was collected and then sequentially subjected to nickel affinity chromatography (Ni-NTA, Qiagen – 300 mM imidazole was used for elution) and size exclusion chromatography (Superdex 200, 10/300 GL, GE Healthcare) equilibrated with a solution containing 150 mM NaCl, and 50 mM Tris-HCl (pH 7.5). Finally, purified P8-GFP was dialyzed overnight against large volumes of PBS, prior to its usage in binding assays.

2.2.3 Binding of Native and Fusion P8-trimers on the Inner Shell Particles

Either native or GFP-fusion P8-trimers were mixed with single-layered particles at a 3,000:1 number ratio. Single-layered particles mixed with P8-GFP-trimers were incubated in PBS overnight on ice whereas single-layered particles mixed with native P8-trimers were incubated in 10 mM MgCl₂ containing 100 mM histidine-buffer (pH 6.0) due to the fact that double-layered RDV particles are more stable in this buffer. After incubation, each sample solution was centrifuged at $200,000 \times g$ for 10 min (S100AT4, Hitachi) in order to remove unbound P8-trimers from the inner shell particles. Precipitants containing assembled particles decorated with either P8-GFP or native P8 proteins were respectively resuspended in either PBS or 10 mM MgCl₂, 100 mM histidine-buffer at pH 6.0. Centrifugation was repeated a second time to wash the samples. The amount of P8-trimer bound to single-layered particles was examined by SDS-PAGE with the image analysis done by using imageJ⁵⁰. The particles before and after binding of P8-trimers were examined under an electron microscope (JEM-1010; JEOL) after negative staining with 2% uranyl acetate.

2.2.4 Cryo-EM and 3D Reconstruction

For the Cryo-EM experiments, 3 μL of each sample solution was applied to a Quantifoil holey carbon grid (Mo, R1.2/1.3, 200 mesh, Quantifoil Micro Tools GmbH), then plunge-frozen into liquid ethane using a Vitrobot mark IV (Thermo Fisher Scientific). The TEM grids were examined at liquid nitrogen temperature with a Cryo-electron microscope (JEM-2200FS, JEOL), incorporating a field emission gun, an omega-type energy filter, and a Zernike phase plate operated at 200 kV and a nominal magnification of $\times 50,000$. A slit width of 20 eV was used to obtain a zero energy loss electron beam. Images were recorded with a $4,096 \times 4,096$ pixels CCD (TVIPS GmbH) with an estimated total electron dose of 20 electrons/ \AA^2 . In the 3D refinement process, the program `sxpdb2em.py`⁵¹ was used to generate a starting model for the inner shell particle with the previously determined RDV crystal structure of chains A and B of the innermost capsid protein P3 and chain K of the P7 protein (PDB ID: 1UF2). To create a model for the single-layered particle, 925 particles were boxed from 160 images using the semi-automatic particle picking option in the program `e2boxer.py`, supplied in the EMAN2 program package⁵² and used in swarm mode. Defocus values were determined using the program CTFFIND3⁵³. All of the following processes were performed using the RELION-1.4 software⁵⁴. Particles were extracted in 350 pixels \times 350 pixels. Extracted particles were subjected to reference-free 2D classification. Three to six representative 2D class averages were selected and 784 particles belonging to these classes were subjected to 3D refinement, starting with the initial model which used a low-pass filter of 60 \AA . An icosahedral symmetry requirement was applied throughout the 3D refinement process. Using the ‘soft auto-mask’ feature an estimate of 13.43 \AA for the resolution was made using the FSC technique with a 0.143 cutoff⁵⁵ (Figure 2-2 and 2-3 A). For analysis of the virion particle with P8-GFP bound to its surface, 1,462

particles were boxed from 121 images. Particles were extracted using a 400×400 pixels matrix. After 2D classification, 4 to 8 representative 2D class averages were selected and 1,388 particles were subjected to 3D refinement with the same conditions applied for the inner shell particle. With the same approach a final resolution of 14.75Å was achieved for the map (Figure 2-2 and 2-3 B).

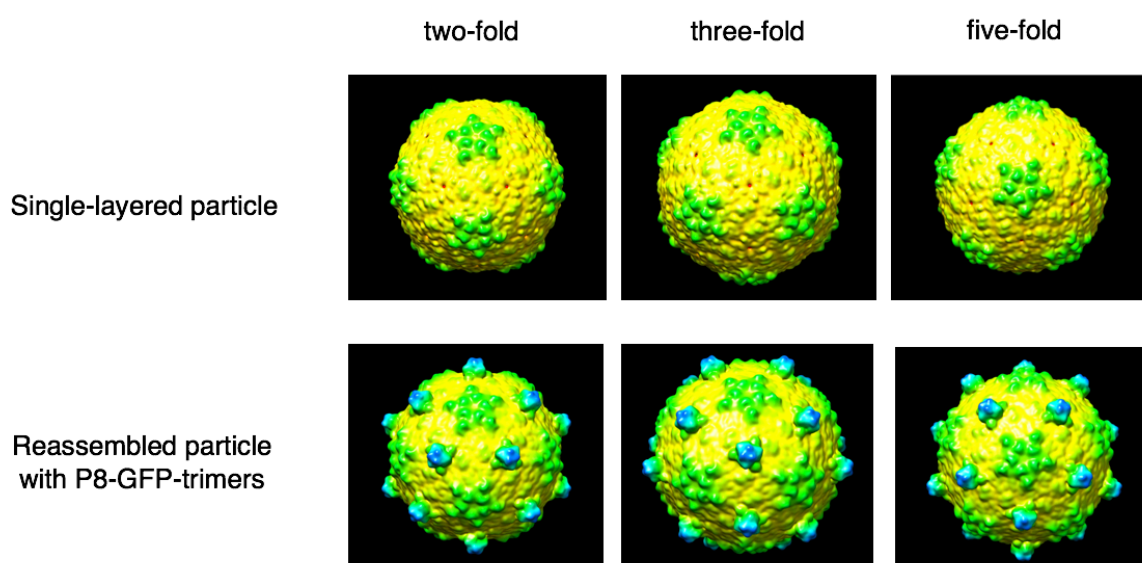


Figure 2-2 The respective views of reconstructed maps

EM structures of the single-layered RDV particle before (upper) and after binding with P8-GFP-trimers (middle). Icosahedral two-, three-, and five-fold axis views are placed at the left, middle, and right columns, respectively.

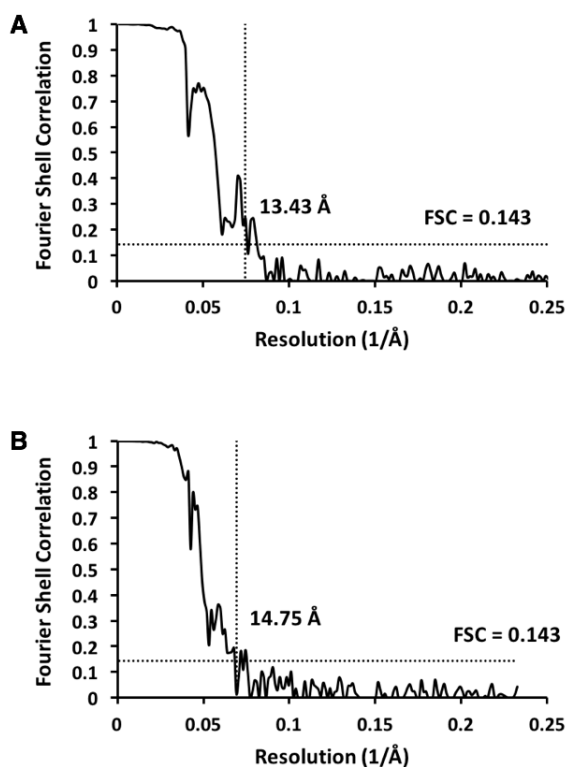
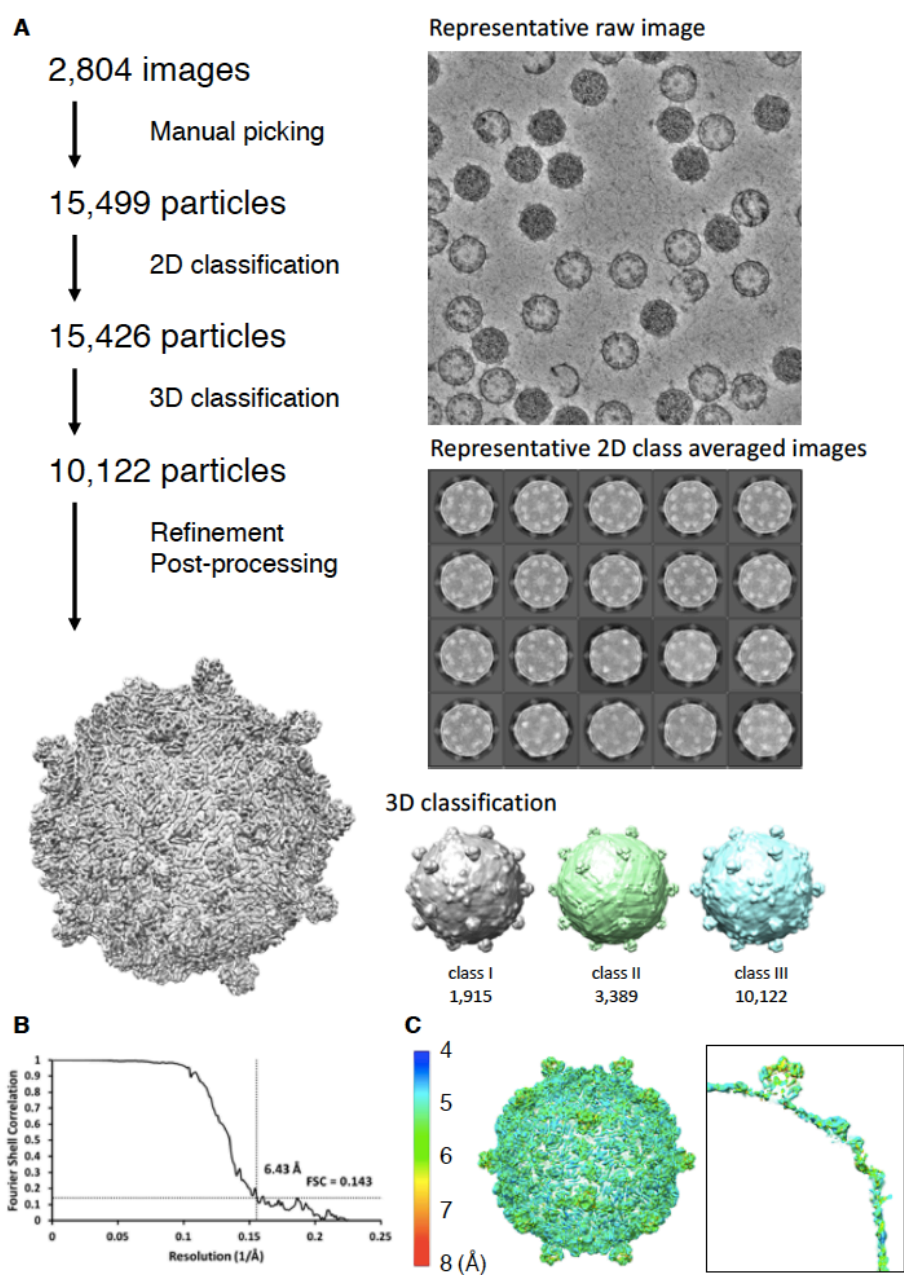


Figure 2-3 FSC curves of the 3D reconstructions created using conventional cryo-EM images. (A) Single-layered RDV particle. (B) Reassembled RDV particle with P8-GFP-trimers.

2.2.5 High Resolution Cryo-EM and 3D Reconstruction

TEM samples for the high resolution Cryo-EM experiments were prepared identically to those used in the lower resolution experiments. However, these Cryo-EM grids were examined at liquid nitrogen temperature with a state-of-the-art cryo-electron microscope (Titan Krios, Thermo Fisher scientific) incorporating a field emission gun, an image corrector, and Volta phase plate. The microscope was operated at 300 kV and a nominal magnification of $\times 47,000$. Images were recorded using a direct electron detector (Falcon II, Thermo Fisher scientific) measuring 32 frames, each with 2.0 s exposure, with a total electron dose of 40 electrons/Å², applied with a nominal underfocus value

ranging from -1.0 to -1.2 μm . The images (1.39 $\text{\AA}/\text{pixel}$) were subsequently aligned and summed using the MOTIONCORR2 software⁵⁶ to obtain a final dose weighted image. Estimation of the contrast transfer function was performed using the Gctf program⁵⁷. Micrographs exhibiting poor power spectra (based on the extent and regularity of the Thon rings) were rejected. Empty and full particles were separately selected, because they could be clearly distinguished by the density apparent at the particle center. All particles were manually picked using the EMAN2 software suite (Figures 2-4 A and 2-5 A). All of the following processes were performed using the RELION-2.0 software^{17,58}. All picked particles were subjected to reference-free 2D classification to remove distorted particles. Selected particles were then subjected to 3D classification, resulting in the assignment into 3 or 4 classes. Finally, the 3D structures of the full and empty particles after binding P8-GFP-trimers were respectively reconstructed at 6.4 and 6.3 \AA resolutions using 10,122 and 13,364 particles (Figures 2-4 B and 2-5 B). Local resolution variations were calculated using the ResMap⁵⁹ program (Figures 2-4 C and 2-5 C).



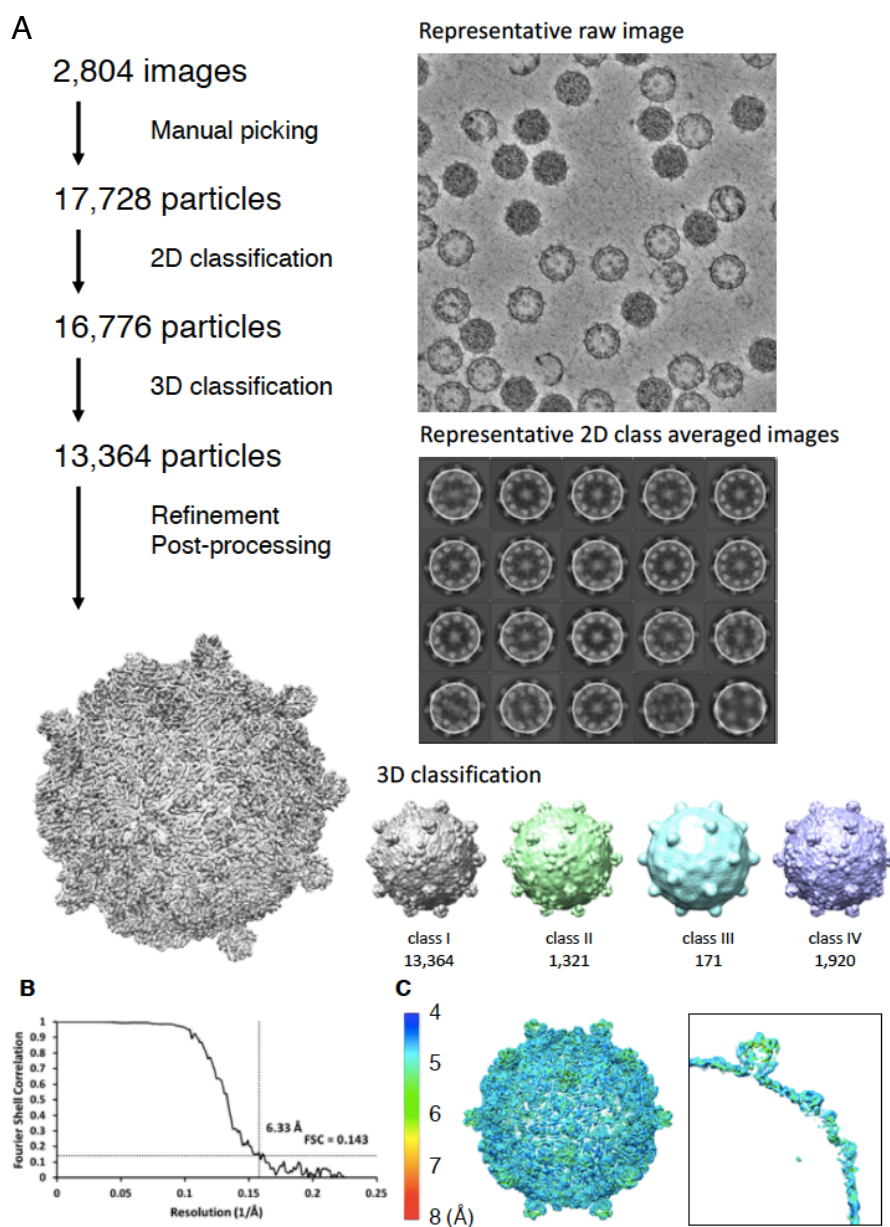


Figure 2-4 and 2-5 Volta phase plate cryo-EM data collection, processing, and validation for the reassembled RDV particle with P8-GFP-trimers (2-4 and 2-5 for full and empty particles, respectively).

(A) Flow chart of the cryo-EM data processing procedure. (B) FSC curve of the final reconstruction.

(C) Local resolution map calculated by *ResMap*.

2.3 Results

2.3.1 Preparation of RDV Assembly Defect P8 Mutant Protein

To interfere with the inter-trimer interactions in the second capsid layer of RDV, GFP was connected to the C-terminus of RDV P8 protein via a linker sequence containing a polyhistidine tag and a thrombin recognition sequence (Figure 2-1 F). The mutant P8-GFP protein was successfully overexpressed using a baculovirus/Sf9 insect cell expression system. The overexpressed P8-GFP protein was purified by serial performance of nickel affinity chromatography and SEC procedures (Figures 2-6 A and 2-6 B, lane 3). The elution volume of the P8-GFP fusion protein indicated a molecular weight of 255,000, highly suggestive of a trimeric state (theoretical molecular weights of a monomer and a trimer of P8-GFP are 77,420 and 232,260, respectively). Upon removal of the GFP and histidine tag (by thrombin affected proteolysis) the estimated molecular weight of the resultant P8 protein by SEC was 133,000, a value close to the theoretical molecular weight of a trimer without GFP proteins (141,510; Figure 2-6 A). These results strongly suggested that P8-GFP proteins form a stable trimer as shown in a native P8 structure^{28,39}.

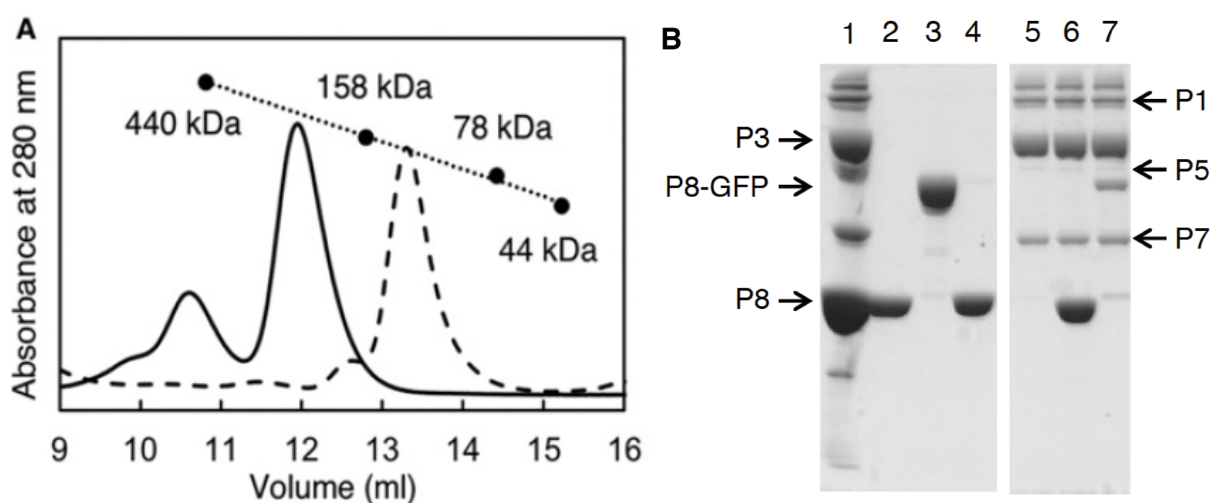


Figure 2-6 Preparation of the P8-GFP (A) SEC elution profiles of P8-GFP and the protein digested by thrombin are shown by solid and dashed curves, respectively. Numbers with a dot indicate the elution volume and molecular mass of the molecular weight marker proteins used to calibrate the column (SDS-PAGE analyses of each sample are shown in B). (B) SDS-PAGE sample analysis. Lane 1, intact RDV particle; lane 2, native P8 trimer separated from RDV particle by size exclusion chromatography; lane 3, purified P8-GFP; lane 4, P8-GFP digested by thrombin; lane 5, single-layered RDV particle; lane 6, reassembled RDV particle, which is made by mixing single layered RDV particles and P8 trimers or P8-GFP trimers, after binding with native P8 trimers; lane 7, reassembled RDV particle after binding with P8-GFP trimers. P3 (114 kDa), P8-GFP (77 kDa), and P8 (46 kDa) are indicated by arrows. P1 (164 kDa), P5 (91 kDa), P7 (55 kDa) proteins which are enclosed within the capsid shell and are involved in a transcriptional complex at the icosahedral 5-fold axes are also indicated.

2.3.2 Preparation of the Inner Shell Particle and the Native P8 Trimer from RDV

Virion

It has been previously reported⁴⁰ that all P8 trimers in the second layer may be dissociated via inclusion of high concentrations of MgCl_2 (≥ 1.6 M) in the buffer solution, with this feature allowing for an easy production route for single-layered RDV virus particles. However, we noticed that P8 T trimers are more tightly bound to the inner capsid than P-, Q-, R-, and S-type P8 trimers and only fully dissociated from the inner capsid at a concentration greater than 1.6 M MgCl_2 and the core particle dissociated at a concentration greater than 2.2 M MgCl_2 ⁶⁰ and so therefore this slightly higher concentration (1.7 M) was used in this study. Following removal of the second capsid layer, the resultant single-layered particles were separated by SEC. Upon collection, the SEC void fraction containing single-layered particles was immediately ultra-centrifuged, and the precipitate resuspended in PBS at pH 7.4. SDS-PAGE

analysis confirmed that P8 trimers were completely removed from the particles (Figure 2-6 B, lane 5). Furthermore, negative-staining EM observations showed that no P8 trimers were bound to the inner capsid layer (Figure 2-8 B). The native P8 trimers eluted in the SEC experiment were also collected and dialyzed against PBS in order to remove MgCl_2 (Figures 2-6 B, lane 2 and 2-7).

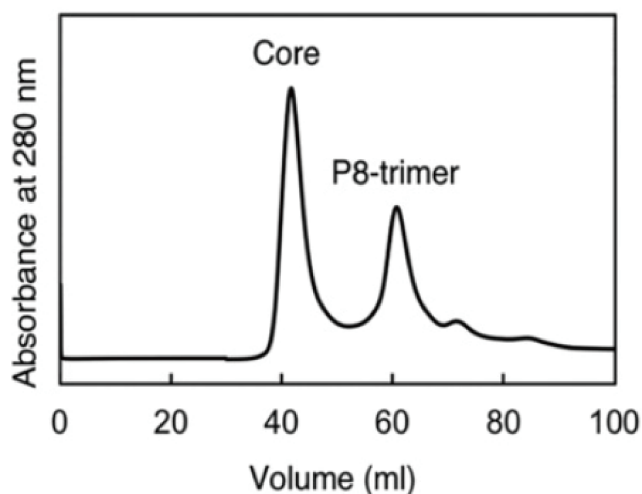


Figure 2-7 Preparation of the Single-Layered RDV Particle

The size exclusion chromatography elution profile of RDV in buffer containing 1.7 M MgCl_2 , monitored by absorbance at 280 nm. The first and second peaks contain single-layered RDV particles and native P8 trimers, respectively (SDS-PAGE analyses of each sample are shown in Figure 2-6).

2.3.3 Binding of P8 Trimer and P8-GFP Trimer to the Inner-Particle Layer

To examine the binding of P8 trimers to the first capsid layer, excess P8 trimers were mixed with the single-layered particles at a 3,000:1 molecular number ratio (P8 trimer: single-layered particle) (recalling that in an intact particle the ratio of P8 trimers to single-layered particles is 260:1). Unbound P8 trimers were removed by multiple differential ultracentrifugation. The amount of bound P8 protein was measured by SDS-PAGE analyses (Figure 2-6 B). In these experiments we found that the number of native P8-trimers bound to the single-layered particles was the same as for the case of

the intact RDV virion (Figure 2-6 B, lane 6), suggesting that native P8 trimers bound to the particle and then formed a second capsid layer. In contrast, when the same excess mixing experiment was performed with P8-GFP trimers, image analysis of the SDS-PAGE bands indicated that 13-fold less molecules of P8-GFP trimers were bound to the single-layered particle than the case for the native P8 trimer (Figure 2-6 B, lane 7). The SDS-PAGE results were confirmed by negative-staining electron microscopy observations which indicated that the mixture of native P8 trimers and single-layered particles resulted in the formation of the complete double-layered spherical particles indistinguishable from the RDV virion (Figures 2-8 A and C), whereas the corresponding mixing experiment involving P8-GFP trimers yielded inner-layer-like structures featuring small protrusions on the surface of the single-layered particles (Figure 2-8 D, arrows), which were clearly distinguishable from single- and double-layered particles (Figures 2-8 A and B).

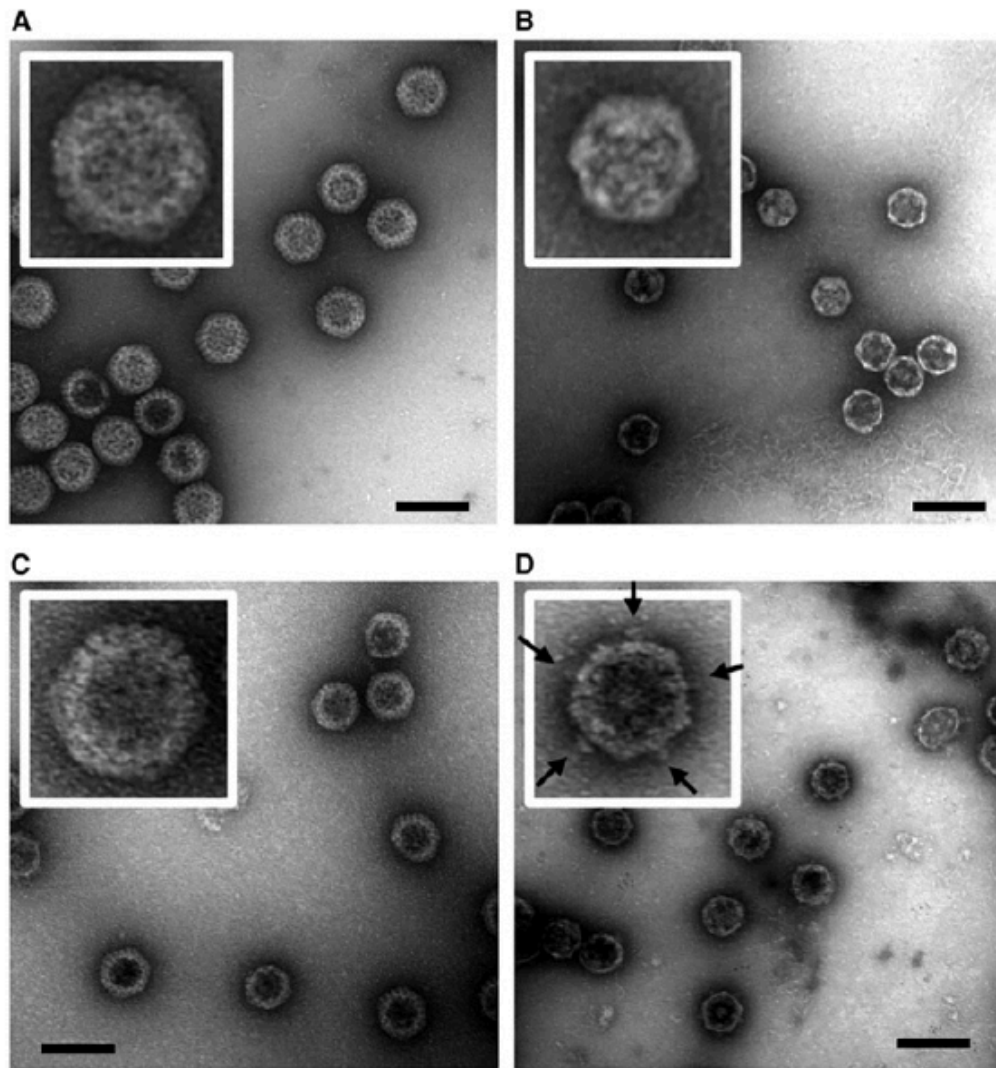


Figure 2-8 Electron Micrographs of Uranyl Acetate-Stained Particles

(A) Intact RDV. (B) Single-layered RDV particle. (C) Reassembled RDV particle after binding with native P8 trimers. (D) Reassembled RDV particle after binding with P8-GFP trimers. Arrows indicate the protrusions on the first capsid layer, corresponding to the P8 trimers. Typical particles are enlarged in upper left boxes. Bars represent 100 nm.

2.3.4 Structural Analysis by Conventional Cryo-electron Microscopy

To elucidate each of the P8-trimer binding positions on the first capsid layer, Cryo-EM single-particle analysis was performed for the inner-layer particles before and after -interaction with the P8-GFP proteins (Figure 2-9). Three-dimensional reconstruction of both particles was performed using capsids containing genomic dsRNA, as these particles demonstrated greater stability than empty particles prepared lacking their dsRNA core. Structures of the single-layered particles, before and after binding with P8-GFP trimers, were respectively determined at 13.4 Å and 14.8 Å resolution using 748 and 1,462 particles. The assessment of resolution was made using a threshold of 0.143 within the Fourier shell correlation⁵⁵ (Figure 2-2). As can be noted, the outer surface of the single-layered particle before binding with P8-GFP trimers is smooth with no visible protrusion being apparent (Figure 2-9 C). An atomic structural model of the RDV virion single-layered capsid (PDB ID: 1UF2) was well accommodated into the Cryo-EM map (Figure 2-10 A). This result showed that P8 trimers were completely removed from the particles by exposure to 1.7 M MgCl₂, confirming the findings of the SDS-PAGE and negative-staining electron microscopy analyses described above. By contrast, 20 protrusions were observed in the structure after allowing for its interaction with the P8-GFP trimers (Figure 2-9 D). The protrusions were located on the icosahedral 3-fold axes, which are exactly the positions at which the P8 T trimers bind in the second capsid layer. An atomic model of the single-layered particle with P8 trimers bound at the T position was produced by superimposing the RDV virion structure (PDB ID: 1UF2) into the Cryo-EM map. The positions of the protrusions were found to precisely coincide with the T trimers without any positional adjustments (Figures 2-3 and 2-10 B). In addition, the shape of the protrusion density also agrees

well with the atomic structure of the P8 trimer. However, contoured at lower density level, additional densities, not found in the truncated atomic model of a single-layered RDV particle with T trimers, were found to spread radially from the P8 C-termini position (Figure 2-10 C, arrow). These additional densities were too small for the P8 trimers at the R-position but were well described by a model of GFP fused to the C-terminus of P8⁵⁵ (PDB ID: 2Y0G; Figure 2-10 D). It should be noted that the sample solution was a mixture of “full” virion particles, containing genomic dsRNA, and “empty” particles, lacking the genomic dsRNA (Figures 2-9 A and 2-9 B). With regard to this point a small number of empty particles are always found in RDV particles isolated from rice plants. However, empty particle numbers were significantly increased upon removal of the second-layer P8 trimers by exposure to high concentrations of MgCl₂. I assumed that leakage of the dsRNA genome from the capsid to produce empty particles was enhanced by the intrinsically lower stability of the single-layered particle and/or capsid damage caused by exposure to high concentrations of MgCl₂.

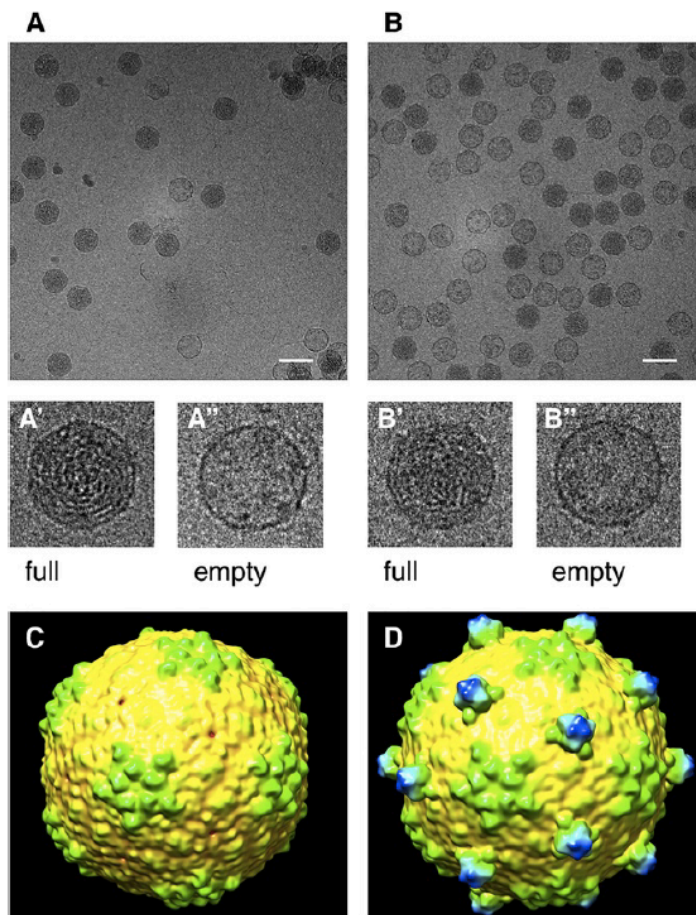


Figure 2-9 Cryo-EM micrographs and 3D reconstructions of reassembled single-layered RDV particle and single-layered RDV particle with P8-GFP trimers. Electron Micrographs of Uranyl Acetate-Stained Particles

(A and B) Cryo-EM micrographs of ice-embedded particles at $-2.0\ \mu\text{m}$ defocus. (A) Single-layered RDV particle. (B) Reassembled single-layered RDV particle with P8-GFP trimers. Full (A' and B') and empty (A'' and B'') indicate the particle with and without genomic dsRNA, respectively. Bars represent 100 nm. (C and D) 3D structures of (C) single-layered RDV particle reconstructed at $13.4\ \text{\AA}$ resolution and (D) single-layered RDV particle with P8-GFP trimers reconstructed at $14.8\ \text{\AA}$ resolution. Images are colored according to the distance from the center of the particle.

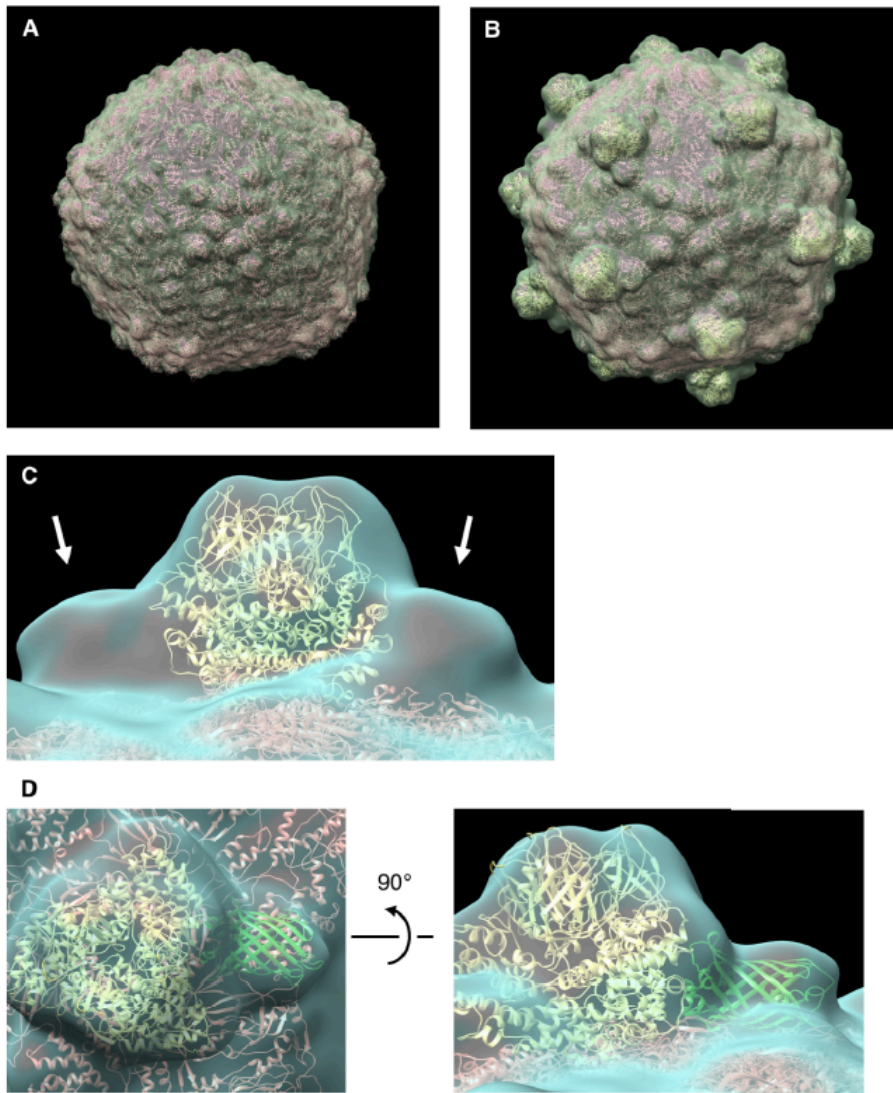


Figure 2-10. The atomic structures of RDV P3 proteins in the first capsid layer (shown in pink), T-trimers (yellow), and GFP (green) are fitted into the Cryo-EM map of the single-layered and reassembled RDV particle with P8-GFP-trimers.

(A and B) Overall view of fitting single-layered RDV particles before (A) and after (B) binding with P8-GFP-trimers, respectively. (C) Enlarged view of fitting for a P8-trimer at an icosahedral 3-fold axis. Arrows show extra-densities around the P8-trimer. (D) GFP is manually fitted into the extra-density with UCSF Chimera.

2.3.5 Structural Analyses by Cryo-EM Equipped with Phase Plates

The Cryo-EM 3D structure showed that the P8 trimers preferentially bound to the T site on the outer surface of the first capsid layer. However, the possibility that the P8 trimers can recognize and bind to the other sites was not completely excluded due to the fact that the densities of other P8 trimers might be averaged out in the process of 3D reconstruction. To eliminate the possibility of artifacts introduced by the averaging process, the particles were examined by Zernike phase-contrast Cryo-EM before and after binding P8-GFP proteins (Figure 2-11). The high image contrast that is possible with phase plate enhancement allowed for the identification of P8-GFP trimer density on the single-layered particles without any requirement for averaging (Figure 2-11 B). The results of these phase-contrast experiments indicated that all particles with P8-GFP trimers bound to their surface exhibited symmetrically arranged protruding densities only at the T-trimer positions (center of the icosahedral facet; Figures 2-11 B and C). In particular, empty particles with bound P8-GFP trimers clearly showed 20 densities of P8-GFP trimers on the particle, in direct accordance with the curtailed atomic model of a single-layered RDV particle featuring the 20 T trimers in place (Figure 2-11 C). By contrast, the particles without any bound P8-GFP trimers showed no protrusion of the dense material on the outer surface of the particles (Figure 2-11 A). These observations strongly support the notion that P8-GFP trimers only bind to the T-trimer positions. To determine higher resolution structure, the assembly intermediate particles were examined by a state-of-the-art Cryo-EM incorporating a field emission gun, an image corrector, Volta phase plate, and a direct electron detecting camera. Indeed, the performance of the Volta phase-contrast Cryo-EM single-particle analysis with the direct electron-detecting camera enabled the determination of the 3D structure of the

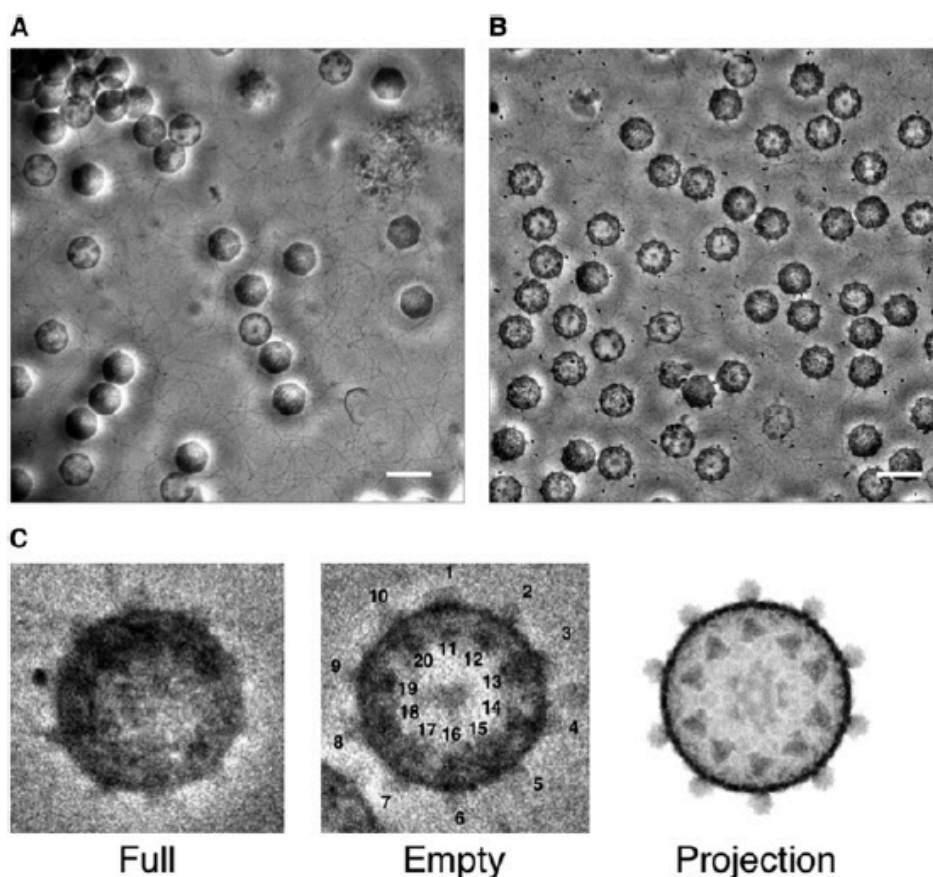


Figure 2-11 Zernike Phase-Contrast Cryo-EM Micrographs

(A and B) Single-layered RDV particles (A) before and (B) after binding with P8-GFP trimers. Bars represent 100 nm. (C) Left, reassembled RDV particle with P8-GFP trimers filled with dsRNA genome (full particle). Middle, reassembled RDV particle with P8-GFP trimers lacking dsRNA genome (empty particle). Right, a projection image generated from the atomic model of the single-layered RDV particle with T trimers located at the icosahedral 3-fold axes, which coincides well with the Cryo-EM images

full and empty particles with bound P8-GFP trimers were reconstructed at 6.4 Å and 6.3 Å resolutions, respectively (Figures 2-4 and 2-5). The high-resolution density map allowed for the identification of α -helix structures and as such the atomic model of the first capsid layer with T trimers could be precisely fitted into the 3D density map at the

secondary structure level (Figures 2-12 A–C). Furthermore, as for the low-resolution structural analyses described above, extra-densities were observed around the P8 trimers radially spreading from the C-termini of the P8 proteins (Figure 2-12 D). These results, obtained by Volta phase-contrast Cryo-EM, confirm that the extra-densities observed around the P8 trimers are indeed due to GFP proteins fused to the P8 proteins' C-termini.

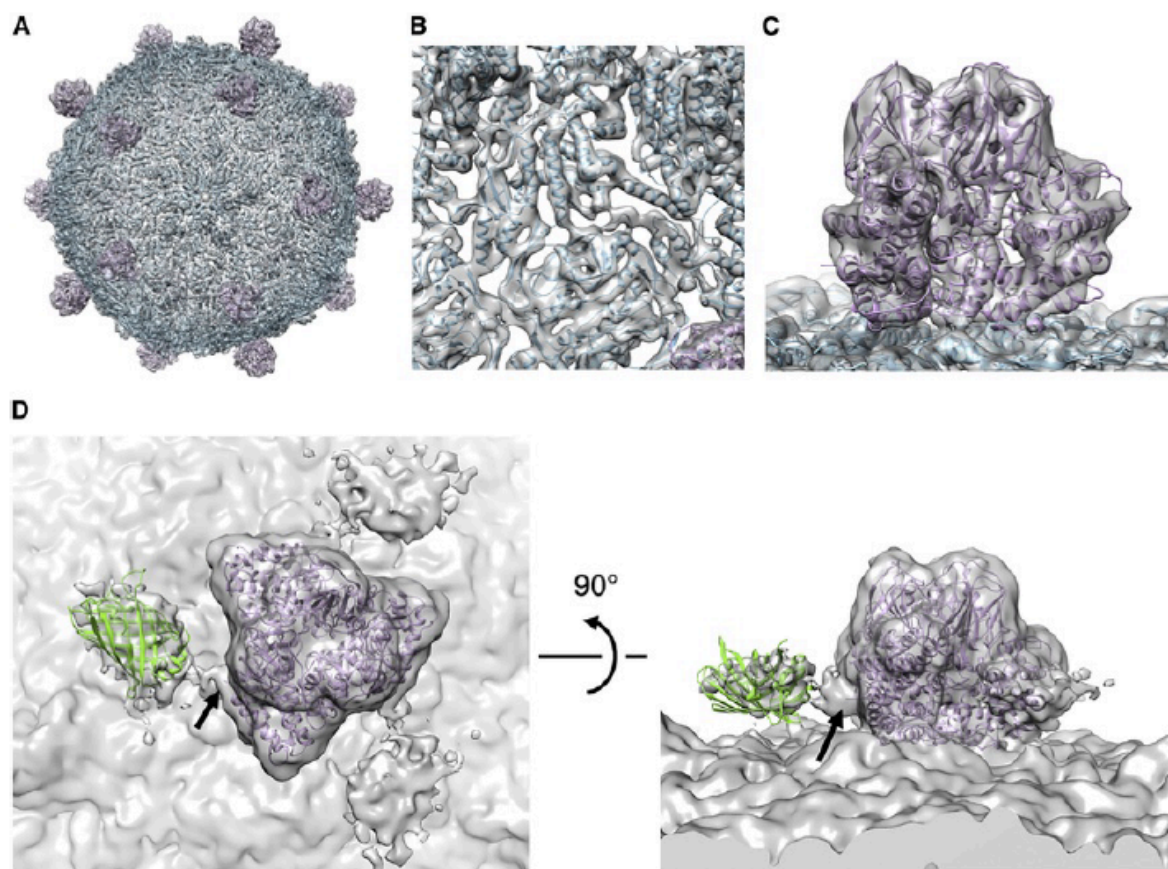


Figure 2-12 High-Resolution map of the Reassembled RDV Particle with P8-GFP Trimers

The atomic structures of P3 proteins in the first capsid layer (shown in cyan), T trimers (purple), and GFP (green) are fitted into the Cryo-EM map (cyan) of the inner shell particle with P8-GFP trimers. (A) Overall view of fitting. (B and C) Enlarged views of fitting around P3 (B) and P8 trimer (C). (D) GFP manually fitted into the density at lower contour level using UCSF Chimera. Arrows indicate the C-terminus of P8.

2.4 Discussion

The RDV outer capsid P8-protein fused with GFP (P8-GFP mutant) was successfully expressed using a baculovirus expression system and was shown to form a stable trimer in a manner similar to the native RDV P8 protein. Analysis by SDS-PAGE demonstrated that in relation to native P8 trimers, P8-GFP trimers bound to the single-layered particle to a 13-fold lower extent such that only 20 copies of P8-GFP trimer existed on the surface of the particle. Cryo-EM single-particle analysis showed that these 20 copies of the P8 trimer were uniquely located at the icosahedral 3-fold axes (the T-trimer position), indicating that second-layer formation initially involves P8-trimer adsorption to the T-trimer position on the single-layered particle. These results suggest that the mechanism of second-layer formation is the traditional epitaxial nucleated-growth type involving an initial nucleation step, in which P8 trimers recognize only the T-trimer positions via inter-layer contact formation, followed by a series of growth steps, in which the P8 trimers bind to the other P-, Q-, R-, and S-trimer positions, in a manner involving both intra- and inter-layer molecular contact formation. In these subsequent growth type interactions, the differently located P8 trimers undergo induced fits (to varying degrees) to increase their extents of bonding contact with the surface of the inner layer. In particular, the Q trimers, after the T trimers, are considered to make the second greatest level of contact with the first capsid layer via an induced-fit process. Despite this enhancement of inter-layer contact formation, the Q trimers could not bind to the inner-layer particles without additional stabilizing lateral inter-trimer (intra-layer) interactions that result from cooperative second-layer formation following the initial P8 trimer T-state occupation. On the basis of the preceding observations I suggest that the assembly sequence of the RDV outer shell proceeds as follows (Figure

2-13). (1) An initial nucleation event involving T-trimer binding to the inner shell particle. (2) A first growth step involving R-trimer attachment to both the inner shell and T trimers. (3) A second growth step involving Q trimers and S trimers attach to the inner shell surface via interactions with the inner-layer particle and bound R trimers. Due to a greater extent of interactions between the Q trimer and the inner core surface (versus the S trimer and surface), the Q trimer may attach prior to S trimer. (4) A third (and final) growth step involving P trimers binding to the icosahedral 5-fold axis on the particle.

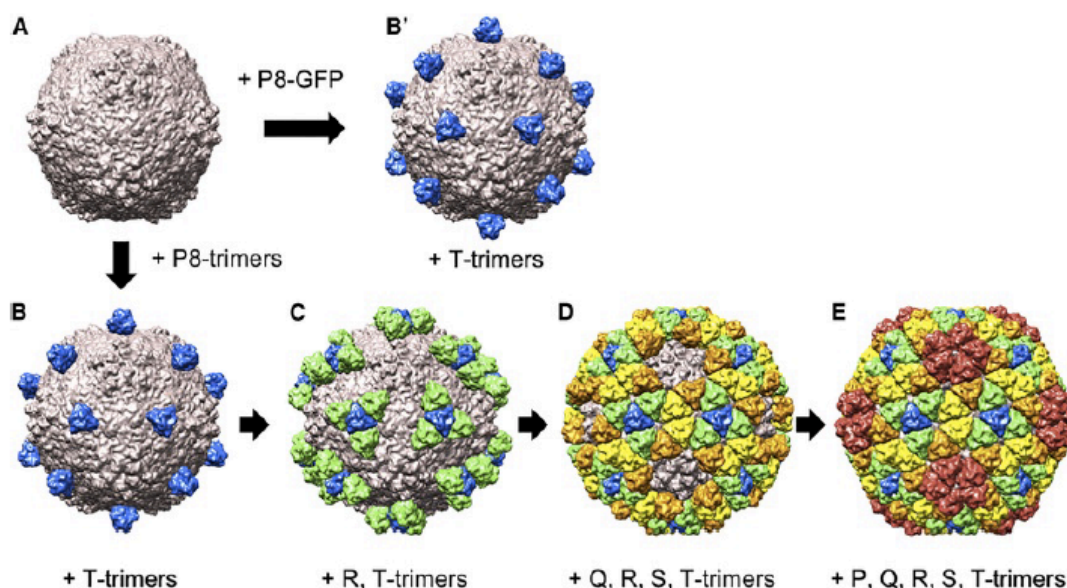


Figure 2-13 Assembly Sequence of the RDV Outer Shell

(A) Single-layered RDV is constructed. (B) P8 trimers bind to the icosahedral 3-fold axis positions as T trimers. (C) R trimers then attach via interactions with the T trimers and the inner shell particle. (D) Q and S trimers further bind to the particle mainly via lateral inter-trimer interactions. (E) Finally, P trimers attach around the icosahedral 5-fold axes. (B') P8-GFP trimers bind to the icosahedral three-fold axis at the T site completing the second shell.

2.5 Conclusion

In this paper I used experimentally derived structural data to determine both the assembly mechanism and mode(s) of molecular recognition between the proteins making up the two capsid layers of the RDV. Interestingly, the assembly order coincides with a model proposed by our group previously²⁸ based on X-ray crystallographic assessment of the binding energy between each P8 trimer and the first capsid layer. Other sedoreoviruses in the family *Reoviridae*, such as *Rotavirus* and *Bluetongue virus*, also feature multilayer capsid structures in which the second capsid shell is composed of protein trimers with an identical arrangement to RDV^{26,38}. Based on this high structural similarity, there is a strong possibility that the protein-trimer sequential assembly model, developed here for RDV, may act as a general paradigm for second-layer assembly across the *Reoviridae* family of viruses. High-contrast Cryo-EM imaging with phase plates allowed us to identify small structural features even at the solution interface. Indeed, the densities of the P8 trimers located at the T-trimer positions on each single-layered particle could be clearly observed in the raw electron micrographs taken by Zernike and Volta phase-contrast Cryo-EM without any averaging^{22,23,46,61} (Figures 2-4, 2-5 and 2-11). Therefore, I could, with high confidence, exclude the possibility that a small amount of P8 trimer was bound at any of the other positions (P-, Q-, R-, and S-trimer positions; Figure 2-11). Furthermore, Volta phase-contrast Cryo-EM single-particle analysis²³ enabled the determination of the 3D structure of the RDV assembly intermediates at sub-nanometer resolution. Interrogation of these structures revealed that the extra-densities around the T trimers are wholly attributable to the GFP fusion product located at the C-termini of the P8 protein. In closing, I highlight what I think to be an important general point to emanate from this

study, namely that high-contrast single-particle Cryo-EM imaging performed using phase plates is an incredibly useful supplementary and/or standalone technique in the structural analysis of biopolymers that are (1) either hard to crystallize or (2) that may exhibit limited structural diversity that would be lost in symmetry-based reconstruction and averaging processes involving many particles.

Chapter 3

Structures of the wild-type MexAB–OprM tripartite pump reveal its complex formation and drug efflux mechanism.

3.1 Introduction

3.1.1 RND-type Multidrug efflux pump

Gram-negative bacteria have a rigid outer membrane consisting of lipid-bilayer and peptidoglycan in addition to an inner membrane, and they express several types of tripartite efflux pumps that penetrate both membranes and release foreign substances⁶². Multidrug efflux pumps of the RND superfamily, which are expressed specifically in Gram-negative bacteria, consist of an RND transporter that penetrates the inner membrane and plays a major role in drug efflux via proton gradient; an OMF that penetrates the outer membrane and secures the efflux route for drugs; and a MFP that is anchored to the inner membrane and connects the RND transporter and OMF^{63,64}. Overexpression of RND-type multidrug efflux pumps is a primary cause of multidrug resistance⁶⁵. *Pseudomonas aeruginosa*, a common Gram-negative bacterium, causes nosocomial infections and has particularly high drug resistance⁶⁶. MexAB–OprM, the only constitutively expressed pump in *P. aeruginosa*, is thought to contribute significantly to drug resistance in this species⁶⁷. The crystal structures of the three proteins constituting MexAB–OprM, MexA, MexB, and OprM, have already been determined^{68–73}.

OprM forms a trimer with three-fold symmetry. Two coiled-coils of helices 3 and 4 (H3-H4) and helices 7 and 8 (H7-H8) in the α -barrel domain form a gate on the periplasmic side. Since H7–8 blocks the gate in the crystal structure, it is thought that the gate is opened by interacting with the MFP⁷². MexA consists of four domains: the membrane-proximal (MP), β -barrel, lipoyl, and α -hairpin domains⁶⁹; it is thought that MexA forms a hexamer in MexAB–OprM. MexB is composed of three domains: a transmembrane (TM) domain with 12 α -helices, a porter domain containing the

drug-binding pocket, and a funnel-like (FL) domain involved in interactions with other components⁷⁰. MexB forms an asymmetric trimer in crystal structure, and it is thought that each protomer shifts conformational states (Access, Binding, and Extrusion) during drug efflux, similar to the functional rotation mechanism proposed based on the structure of the *Escherichia coli* homolog AcrB⁷⁴. On the other hand, based on structural analysis of an RND pump derived from *Campylobacter jejuni*⁷⁵, a distinct efflux mechanism was proposed, suggesting that the mechanisms of action of RND family members are not uniform.

AcrAB–TolC, a major RND-type multidrug efflux pump in *E. coli*, has been extensively investigated, and its structure was solved by Cryo-EM^{76,77}. These studies revealed that OMF and the RND transporter do not directly interact. Furthermore, recent work revealed the asymmetric structure of AcrAB–TolC with closed or open TolC at medium resolution, as well as the symmetric structure of open AcrAB–TolC in the presence of inhibitor, at near-atomic resolution⁷⁸. Based on these structures, it was suggested that AcrAB–TolC initially forms a complex in the closed state, and then TolC opens via rearrangement of the AcrA hexamer induced by a conformational change in AcrB. However, because these studies used genetically engineered or disulfide linked MFP-RND fusion proteins for structural analysis, no structural information was obtained from a wild-type RND-type multidrug efflux pump. Moreover, although 3D structure of MexAB–OprM using a negative-stain method was reported previously⁷⁹, no (near-) atomic resolution structure of a multi-drug efflux pump derived from *P. aeruginosa* has been elucidated to date. Therefore, there was insufficient information to discuss the function of RND-type multidrug efflux pump derived from *P. aeruginosa* in detail.

3.1.2 The outline of this study

In order to investigate the detailed drug efflux mechanism of MexAB–OprM, I prepared intact MexAB–OprM complex without any peptide linker or chemical crosslink by an *in vitro* reconstruction method. Structural analysis was carried out with Cryo-EM single-particle analysis. I obtained Cryo-EM maps at near-atomic resolution, which revealed the detailed interactions between each protein. Surprisingly, there were two binding state between MexA and OprM, and MexB had a different conformation from the crystal structure. To ascertain the effect of the presence of the drug, I vitrified MexAB–OprM in the presence of drug and analyzed its structure in the same way as the apo-state. Based on a structural comparison, I propose a mechanism for complex formation, as well as a mechanism for drug release that differs from previously proposed mechanisms for RND-type multidrug efflux pump complexes.

3.2 Material and method

3.2.1 Expression and purification of MexA, MexB and OprM

MexA, MexB, and OprM were expressed and purified as previously described^{68,70,72} with slight modifications. The gene encoding MexA (a.a., 2–360), which lacks the region containing the signal peptide and the first cysteine, was cloned into vector pET28 (b+) with an N-terminal 6xHis-tag followed by a TEV protease cleavage site. The resultant plasmid was transformed into BL21-RILP (DE3). The bacterial cells were cultured in LB medium, and the protein expression was induced with 0.4 mM IPTG. Collected cells were suspended in buffer A (50 mM Na-phosphate [pH 7.4], 300 mM NaCl) supplemented with 10 mM imidazole and 1 μ M PMSF, and then disrupted by sonication and centrifuged at 39,000 *g* for 30 min. The supernatant was purified with Ni-NTA (QIAGEN), which was eluted with 250 mM imidazole. The 6xHis-tag was removed with TEV-protease, and the de-tagged sample was subjected to a Superdex200 16/60 column (GE healthcare) with buffer B (20 mM Na-phosphate [pH 7.4], 150 mM NaCl). Peak fractions were concentrated to ~50 mg/mL using a VIVASPIN 20 mL (10,000 MWCO).

The gene encoding full-length MexB was cloned into vector pET22 (b+) vector with a C-terminal 6xHis-tag, and the resultant plasmid was transformed into C43 (DE3). The bacterial cells were cultured in TB medium, and protein expression was induced with 1.2 mM IPTG. Collected cells were disrupted in a French press (SMT CO., LTD.), and debris was removed by centrifugation at 10,000 *g* for 10 min at 4°C. Membrane fractions were collected by ultracentrifugation at 45,000 rpm for 1 h at 4°C (45 Ti rotor, Beckman). Collected membrane fractions were washed with high-salt buffer (50 mM Na-phosphate [pH 7.4], 1 M NaCl), and then collected by ultracentrifugation. This wash

step was repeated three times. The washed membranes were resuspended in buffer A supplemented with 30% (v/v) glycerol, flash frozen in liquid nitrogen, and stored at -80°C. Thawed membranes were suspended in buffer A, and then 1% (w/v) DDM (Anatrace) was added for additional washing. After ultracentrifugation at 30,000 rpm for 1 h at 4°C (SW32 Ti rotor, Beckman), soluble impurities were discarded. The precipitate was resuspended in buffer A and supplemented with 2% (w/v) DDM and 40 mM imidazole (pH 7.4). The mixture was stirred at 4°C for 1 h, and the insoluble fraction was removed by ultracentrifugation as described above. The soluble fraction was subjected to Ni-chelating Sepharose (GE Healthcare) in an Econo-column (Bio-Rad). The resin was washed with buffer A containing 150 mM imidazole and 0.1% (w/v) CYMAL-7 (Anatrace), and then purified MexB was eluted with buffer A containing 350 mM imidazole and 0.02% CYMAL-7. Eluted samples were gathered, concentrated using a SPIN-X 20 mL (100,000 MWCO), and subjected to a Superdex200 16/60 column with buffer C (buffer B supplemented with 0.02% CYMAL-7). Peak fractions were concentrated to ~25 mg/mL.

The gene encoding full-length OprM was cloned into vector pET21(b+) vector with a C-terminal 6x His-tag, and the resultant plasmid was transformed into C43 (DE3). The bacterial cells were cultured in 2x YT medium, and the protein expression was induced with 1.2 mM IPTG. Disruption, membrane fractionation, and first wash were performed as described above for MexB. The inner membrane fraction was solubilized with 2% (v/v) Triton X-100 at 4°C for 20 min. Solubilized inner membrane was removed by ultracentrifugation, and then washed once with 50 mM Na-phosphate [pH 7.4] supplemented with 5% glycerol. The washed membranes were resuspended with buffer A supplemented with 30% (v/v) glycerol, flash frozen in liquid nitrogen, and stored at

-80°C. Thawed membranes were suspended with buffer A supplemented with 2.5% OG (Anatrace) and imidazole (pH 7.4) to 20 mM. The mixture was stirred at 4°C for 1 h, and the insoluble fraction was removed by ultracentrifugation at 45,000 rpm for 1 hour at 4°C (50.2 Ti rotor, Beckman). The soluble fraction was subjected to Ni-NTA in an Econo-column. The resin was washed with buffer A containing 40 mM imidazole and 0.1% CYMAL-7, and then purified OprM was eluted with buffer A containing 250 mM imidazole and 0.02% CYMAL-7. Eluted fractions were gathered and subjected to a Superdex200 16/60 column with buffer C. Peak fractions were concentrated to ~10 mg/mL using a SPIN-X 20 mL (100,000 MWCO).

3.2.2 Reconstruction of MexAB–OprM

Purified MexA, MexB, and OprM were mixed at a molar ratio of 3:1:1 in buffer C, and the mixture was dialyzed against buffer D (20 mM Na-citrate, 300 mM KCl, 0.02% CYMAL-7) at 4°C. Unreconstructed proteins were removed by SEC on a Superdex200 16/60 column or Superose6 Increase 10/300 column (GE healthcare) in buffer D. Peak fractions were concentrated with a SPIN-X 20 mL (100,000 MWCO).

3.2.3 Detergents removal and replacement with Amphipol

Reconstructed MexAB–OprM (~4 mg) was precipitated by mixing buffer D supplemented with 20% (v/v) PEG-3350 at a volume ratio of 1:2 and then centrifuging at 20,400 g for 30 min at 4°C. After removal of the supernatant, 250 µL of 50 mM HEPES-K (pH 7.5) containing 20 mg of Amphipol A8-35 (Anatrace) was added to the pellet, and the sample was incubated at 4°C for 4 h with gentle rotation. Subsequently, ~125 mg of Bio-Beads SM2 (Bio-Rad) was added to the sample, which was rotated at

4°C overnight. The beads were removed with a poly-prep column (Bio-Rad). The sample was subjected to a Superose6 Increase 10/300 column with 50 mM HEPES-K (pH 7.5). Peak fractions were concentrated with an Amicon Ultra-0.5 mL 100K (Merck Millipore).

3.2.4 Negative-stain electron microscopy single-particle analysis

The purified MexAB–OprM was diluted to ~20 µg/mL. The sample was applied onto 200 -mesh copper grid (Nisshin-EM) with homemade continuous carbon film and stained with 2% uranyl acetate. The data sets were collected on a H-7650 (Hitachi) operated at 80 kV, equipped with a 1024 × 1024 pixels CCD (TVIPS). Images were recorded at a nominal magnification of 60,000x (corresponding to a pixel size of 5.1 Å). Images were recorded for exposure times of 1 s, with defocus value ranging from -1.0 to -4.0 µm. Defocus values were determined using the program CTFFIND3⁵³. All of the following processes were performed using the RELION-1.3⁵⁴ software unless otherwise noted. A total of 1,750 particles were extracted from micrographs by auto-picking and manually selection. An initial model for first 3D reconstruction was created by e2initialmodel.py supplied in the EMAN2 program package⁵². A C3 symmetry requirement was applied throughout the following 3D classification or refinement process. The selected particles were subjected to 3D classification, resulting in the assignment into 3 classes. Finally, the 3D structure of the MexAB–OprM was reconstructed at 22.5 Å resolution using the FSC technique with a 0.143 cutoff.

3.2.5 TEM data acquisition

For the apo-state, 2 µL of sample solution (9.1 mg/mL) was applied to a glow-discharged holey carbon film (Quantifoil 1.2/1.3 R, 300-mesh Mo grid). The grid

was blotted for 6 s and flash-frozen in liquid ethane using a Vitrobot Mark IV (FEI). The data sets were collected on a Titan Krios G2 (FEI) operated at 300 kV, equipped with an FEI Falcon II direct detector. Images were recorded at a nominal magnification of 75,000x (corresponding to a pixel size of 0.875 Å). Thirty-two frames were recorded for exposure times of 2 s, with defocus value ranging from -1.25 to -3.0 µm; the total dose was 40 e⁻/Å² (Figure 3-1 A).

For the NOV-binding state, the sample (10.2 mg/mL) was mixed with 100 mM NOV in 500 mM HEPES-K (pH 7.5) at a volume ratio of 9:1 1 hour before grid preparation. As a result, the final concentrations of protein and NOV were 9.2 mg/mL and 10 mM, respectively. Grids were prepared as described above for the apo-state. The data sets were collected on a Titan Krios G2 operated at 300 kV, equipped with an FEI Falcon III direct detector (linear mode). Images were recorded at a nominal magnification of 59,000x (corresponding to the pixel size of 1.125 Å). Thirty-two frames were recorded for exposure times of 2 s, with defocus value ranging from -1.25 to -2.5 µm; the total dose was 40 e⁻/Å² (Figure 3-1 B).

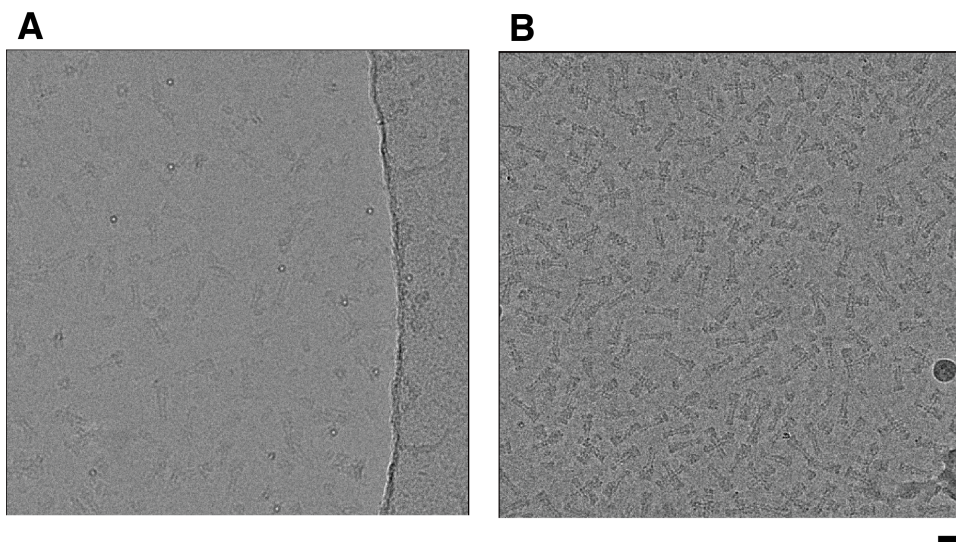


Figure 3-1 Representative Cryo-EM micrographs

Representative Cryo-EM micrograph of MexAB–OprM in apo-state (A) and in NOV-binding state (B) at about -2.5 µm defocus. The bar represents 20 nm.

3.2.6 Image processing and 3D reconstruction

Movies were motion-corrected using MOTIONCORR2 (version 0130217)⁵⁶ with dose fraction. CTF values were estimated with Gctf (version 1.06)⁵⁷. The following processes were performed in RELION-2.0^{17,58}. For the apo-state, 8,772 micrographs were used for particle picking. A total of ~20,000 manually picked particles were subjected to 2D class averaging to create a reference for auto-picking. A total of 535,948 particles were extracted from micrographs by auto-picking, and 2D class averaging was performed to remove false particles. After 2D classification, the remaining 420,182 particles were subjected to 3D classification. Three-dimensional reconstruction of MexAB–OprM by negative-stained electron microscopy single-particle analysis which was described above with low-pass filter of 60 Å was used for the initial model. I performed 3D refinement on the 174,534 particles remaining after 3D classification. Although the Cryo-EM map of MexAB–OprM at this step had a resolution of ~4 Å resolution, several ambiguous regions, including the upper region of OprM and the bottom region of MexB, were present. To remove ambiguity, I performed sequential local 3D classification of 155,822 particles, which were subjected to additional whole 3D classification to remove bad particles. First, we performed local classification of the OprM–MexA region, enabling separation of the two binding states of OprM (0° state: 57,499 particles; 60° state: 69,224 particle). Second, I attempted to remove the ambiguity in the MexB region by local classification, but this approach failed because of a symmetry mismatch in the α -hairpin domain of MexA (C6 symmetry) and MexB trimer (pseudo-C3 symmetry). Therefore, I used a symmetry expansion method to apply the correct angles to the particles⁸⁰: The data set was enlarged threefold by adding 0°, 120°, or 240° to the first Euler angle for each particle (172,347 particles in the 0° state; 207,672 particles in the

60° state), and subjected to local 3D classification of the MexB region. Finally, particle sets with good homogeneity and correct angles were selected (37,971 particles in the 0° state; 42,338 particles in the 60° state). These particles were subjected to 3D refinement, yielding maps with near-atomic resolution (for the 0° state, 4.21 Å in unmask and 3.72 Å in mask; for the 60° state, 4.55 Å in unmask and 3.93 Å in mask). To calculate maps at better resolution, I subtracted the density corresponding to Amphipol and performed a final 3D refinement. This approach yielded improved maps: 4.12 Å in unmask and 3.64 Å in mask for the 0° state, and 4.17 Å in unmask and 3.76 Å in mask for the 60° state. Figure 3-2 shows a whole process of these calculation.

For the NOV-binding state, I performed single-particle analysis as described above for the apo-state. A total of 4,681 micrographs were used for particle picking, and 902,901 particles were extracted by auto-picking. After 2D classification, 659,742 particles remained, and 445,966 particles were subjected to the first 3D refinement after 3D classification. The calculated map had same ambiguities as the apo-state, so I performed local classification for OprM–MexA, resulting in separation of the 0° state (230,289 particles) and 60° state (215,677 particles). After symmetry expansion and two rounds of local classification for the MexB region, good particle sets with 31,409 (0° state) or 31,466 (60° state) particles were subjected to 3D refinement. In these refinements, Cryo-EM maps was calculated for the 0° state at 4.04 Å in unmask and 3.60 Å in mask, and for the 60° state, 4.14 Å in unmask and 3.71 Å in mask. After density subtraction and final refinement, resolution was improved to 3.95 Å in unmask and 3.50 Å in mask (0° state) and 4.09 Å in unmask and 3.60 Å in mask (60° state). Figure 3-3 shows a whole process of these calculation.

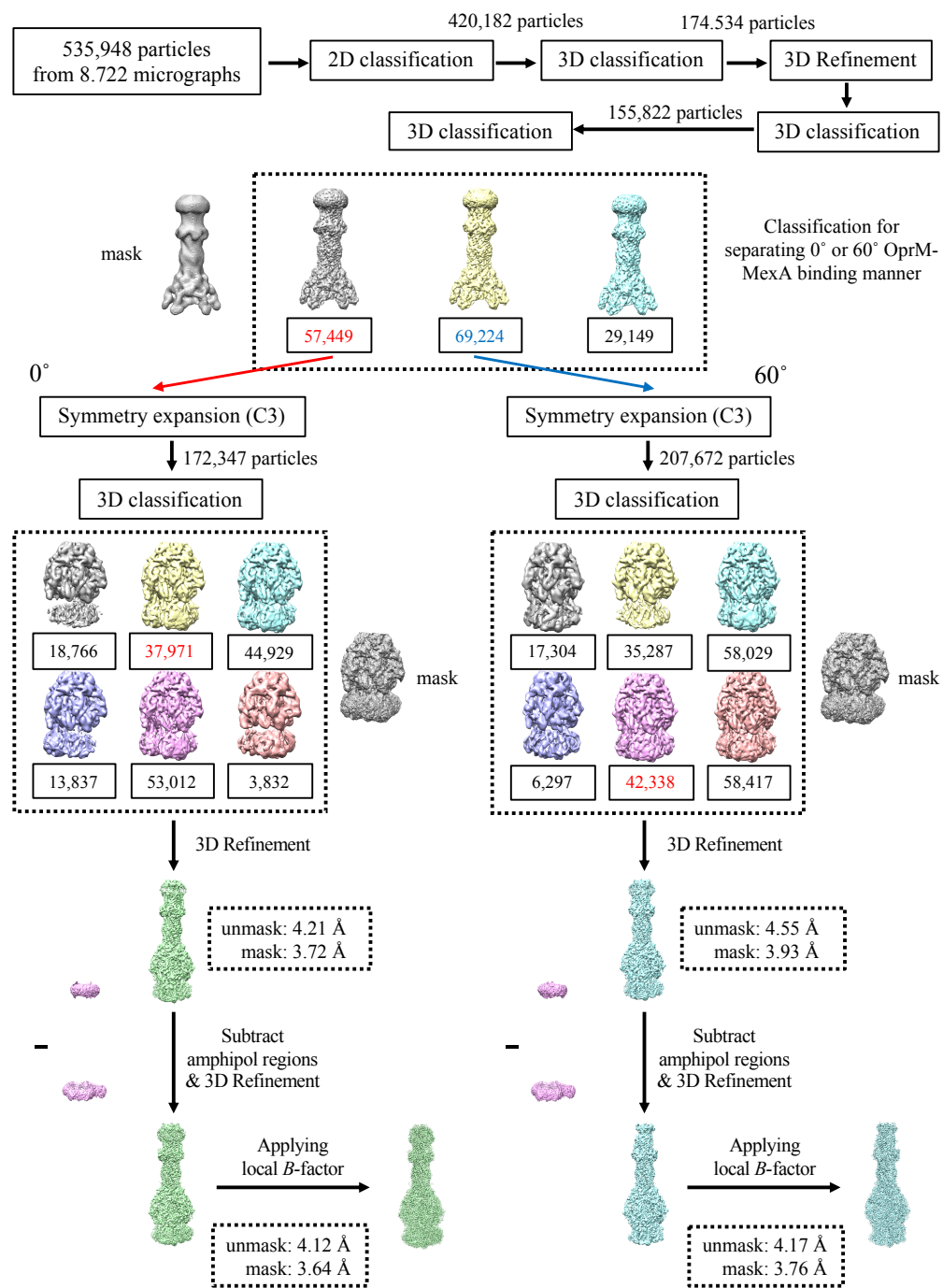


Figure 3-2 Single-particle analysis of the apo-state.

Overview of image processing, 3D reconstruction, and map sharpening.

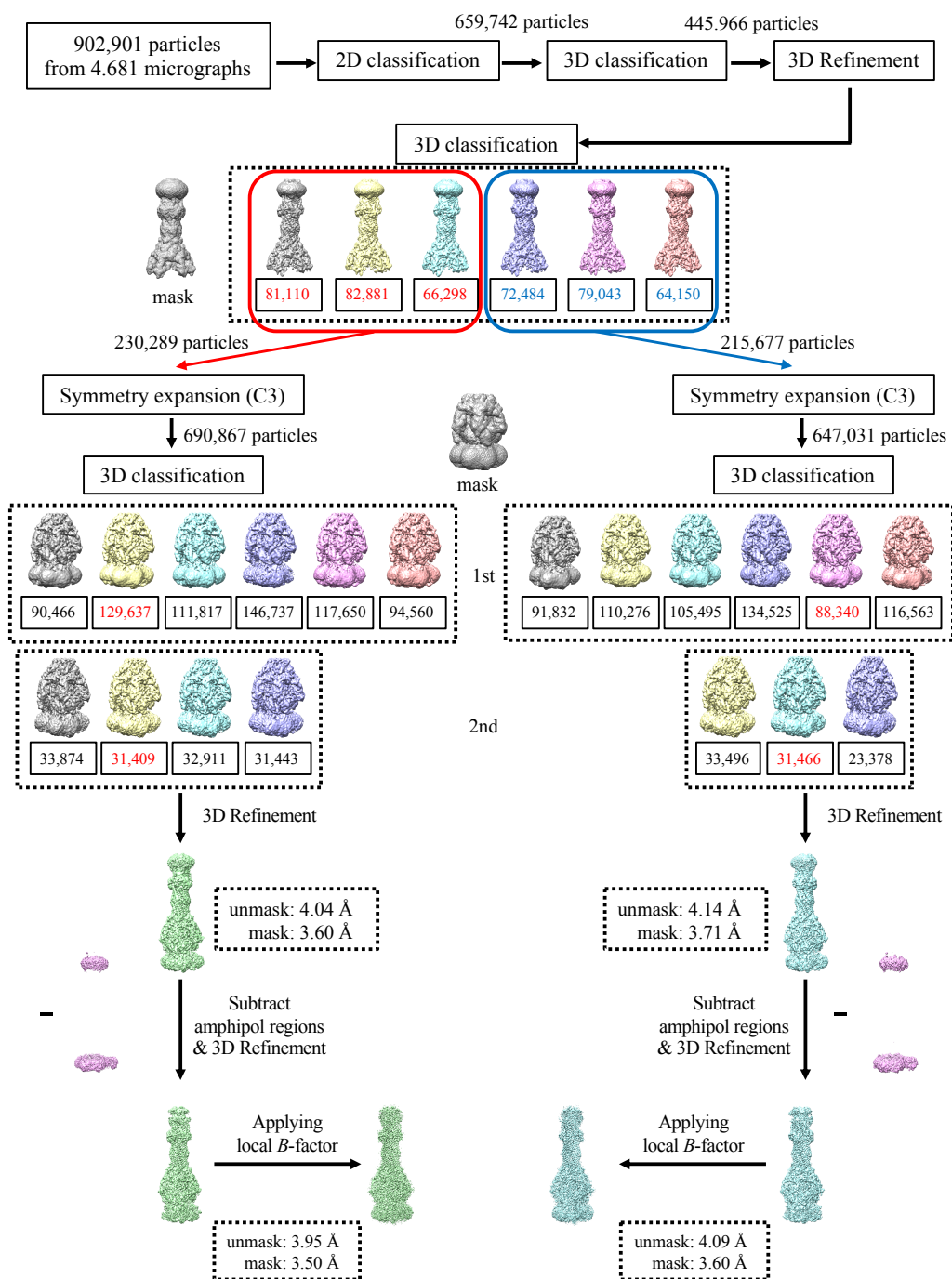


Figure 3-3 Single-particle analysis of the NOV-binding state.

Overview of image processing, 3D reconstruction, and map sharpening.

3.2.7 Model building, map sharpening, and structural validation

Models of fully opened OprM trimer and MexA hexamer were prepared using molecular dynamics flexible fitting (MDFF)⁸¹. Closed OprM (PDB ID: 3d5k) was fitted into the calculated map (apo-state, 0° state) by rigid-body fitting using Chimera⁸², followed by flexible fitting using MDFF. Six MexA protomers (PDB ID: 2v4d, B chain) were fitted into the map using Chimera, and subsequently fitted using MDFF. The crystal structure of MexB (PDB ID: 3w9i) was simply fitted into the map using Chimera. The coordinate files were gathered and subjected to one round of real-space refinement by *phenix.real_space_refine*⁸³ and reciprocal space refinement by *phenix.refine*⁸⁴. The atomic model that performed this process was used for local *B*-factor sharpening of the Cryo-EM map using the program *locscale*⁸⁵. Final models were obtained after several rounds of manual correction by *coot*⁸⁶ and real-space refinement against the locally sharpened maps. Local resolution validation was performed with ResMap⁵⁹. The pathways for drug efflux in MexB were estimated using *caver* 3.0.1.

3.3 Results

3.3.1 Structural determination and overall structure of apo-state MexAB–OprM

MexA, MexB and OprM were expressed and purified respectively (Figure 3-4). Fully assembled MexAB–OprM pump was prepared by *in vitro* reconstruction method (Figure 3-5). The detergents used in each preparation of MexB and OprM were replaced with amphipol A8-35⁸⁷. The 3D structure of apo-MexAB–OprM was determined by Cryo-EM single-particle analysis (Figure 3-3). During this analysis, I identified two modes of binding of OprM to MexA; accordingly, I determined the structures of both states of MexAB–OprM pumps at resolutions of 3.64 Å (state A; Figure 3-6 A) and 3.76 Å (state B; Figure 3-6 B). These maps are of sufficient quality to C α -trace, and I could identify orientations of almost all of bulky side chains (Supplementary Figure 4). Particle distributions and local resolution validations indicated that these maps had good quality. (Figure 3-7). I build the atomic model of MexAB–OprM from respective crystal structures. The refinement statics are summarized in Table 1. The FSC curves for final models versus final maps indicate that the models are well matched to the reconstructed maps (Figure 3-8).

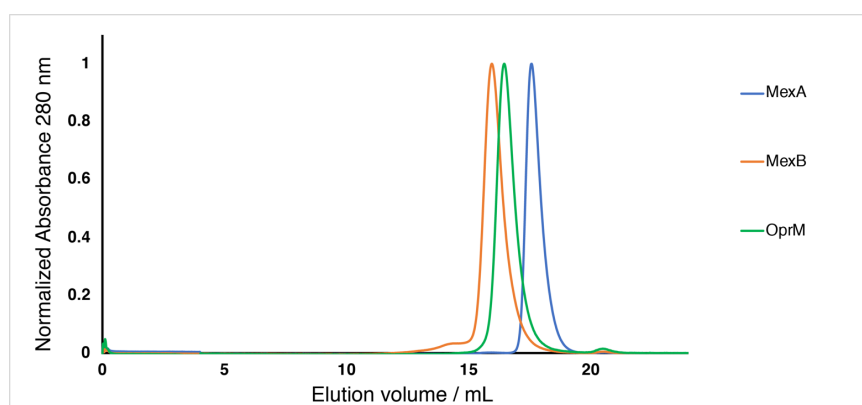


Figure 3-4 SEC charts of purified protein

SEC chart of MexA, MexB, and OprM on a Superose6 Increase 10/300 column with buffer B (MexA) or buffer C (MexB and OprM), respectively.

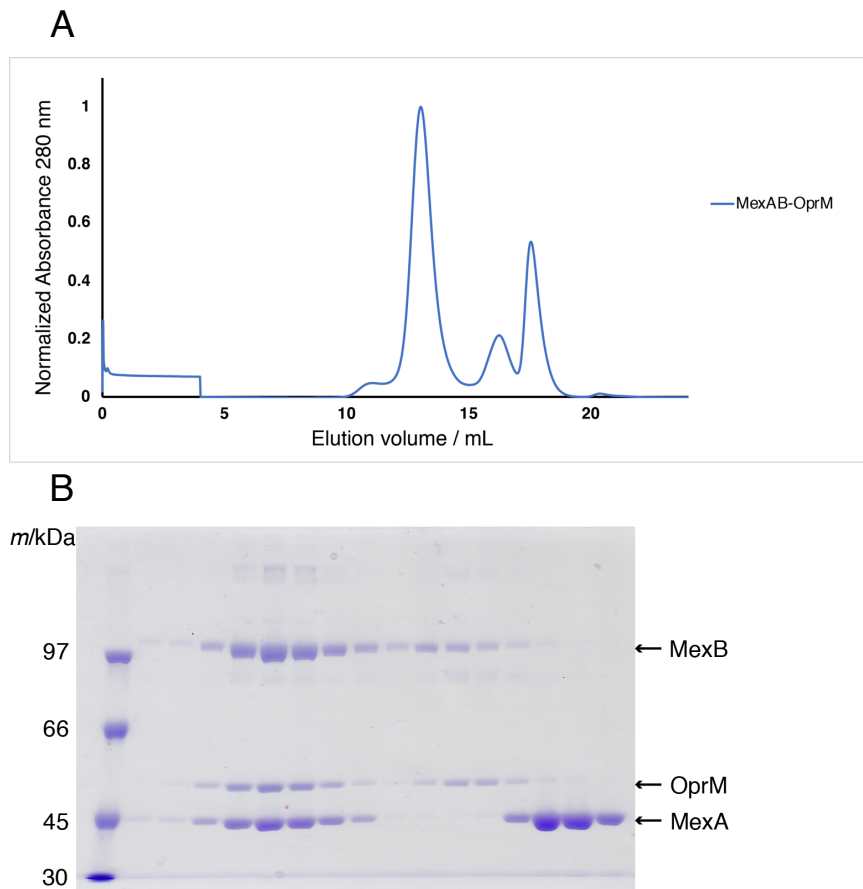


Figure 3-5 Reconstruction of MexAB–OprM.

(A) and (B) SEC chart of the reconstructed sample (A) and SDS-PAGE of its fractions (B).

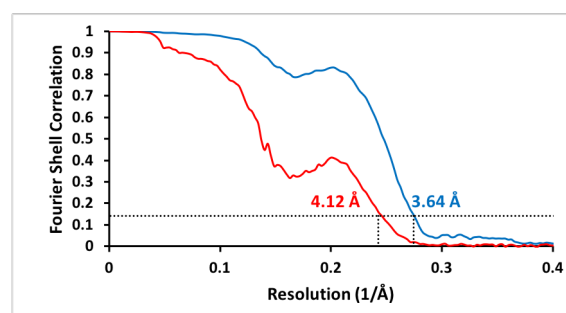


Figure 3-6 FSC curves of final reconstructions

Fourier shell correlation (FSC) curves before (red) and after (blue) postprocessing of state A (A) or state B (B), respectively

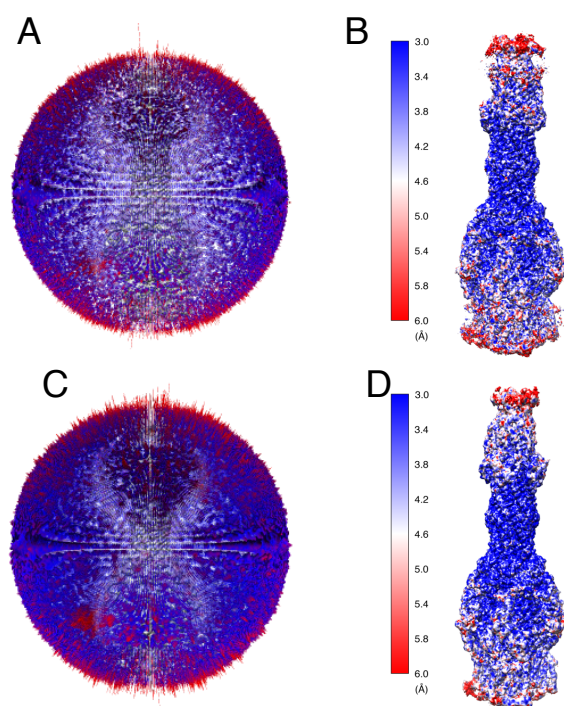


Figure 3-7 Angular distributions and local resolution validation

(A, C) Angular distribution histograms of state A (A) and state B (C)

(B, D) Local resolution estimation of state A (B) and state B (D), calculated using ResMap

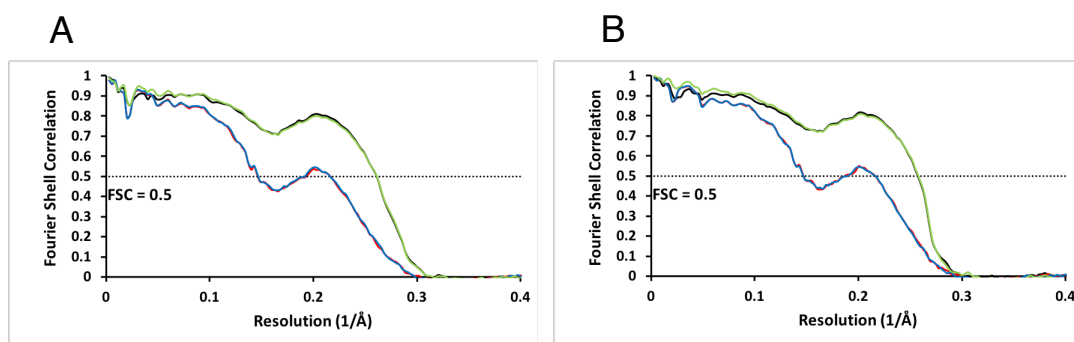


Figure 3-8 FSC curves for models versus maps

FSC curves for final model versus final *locscale* map (black), masked map (green), half map 1 (red), and half map 2 (blue), respectively.

Table 1. Summary of apo-state MexAB–OprM structures

	state A (0°) EMDB: EMD-9695 PDB: 6IOK	state B (60°) EMDB: EMD-9696 PDB: 6IOL
Data collection and processing		
Microscope	FEI Titan Krios	
Magnification	75,000x	
Voltage (kV)	300	
Electron exposure (e ⁻ /Å ²)	40	
Detector	FEI Falcon II	
Pixel size (Å/pixel)	0.875	
Defocus range (μm)	-1.25 to -3.0	
Number of used micrographs	8,722	
Initial number of particles	535,948	
Final number of particles for reconstruction	37,971	42,338
Symmetry imposed	C1	C1
Box size (pixels)	400	
Map resolution (Å)	3.64	3.76
FSC threshold	0.143	0.143
Refinement		
Model composition		
Number of non-H atoms	49,014	49,077
Protein residues	6,441	6,450
Ligands	-	-
<i>B</i> factors (Å ²)		
Proteins	24.49	22.99
Ligands	-	-
R.M.S deviations		
Bond lengths (Å)	0.007	0.005
Bond angles (°)	1.036	0.961
Ramachandran plot		
Favored (%)	95.40	94.44
Allowed (%)	4.60	5.56
Outliers (%)	0	0
Validation		
MolProbity score	1.59	1.65
Clashscore	5.10	4.68
Poor rotamers (%)	0.35	0.33
Model resolution (Å)	3.85	3.89
FSC threshold	0.5	0.5
Real Space CC	0.757	0.760

The overall structure of MexAB–OprM is a vertically elongated rod shape, ~ 320 Å along the long axis and ~ 110 Å along the short axis, and the stoichiometry of OprM, MexA, and MexB is 1:2:1 (Figure 3-9). MexB does not directly contact OprM; instead, MexA joins MexB and OprM by forming a funnel-like hexamer. Among the four domains of MexA, only the α -hairpin domain interacts with OprM; the β -barrel domain interacts with the FL domain of MexB, and the MP domain interacts with the porter domain of MexB. The lipoyl domain of MexA does not connect with either OprM or MexB, but it forms a hexameric ring along with the β -barrel domains. MexA protomers are divided into two classes according to the area of their interaction surface with MexB: the large-contact (LC) protomer (~ 1450 Å²) and the small contact (SC) protomer (~ 950 Å²). The MP domains of the LC protomers are located in the PC1 domains of each MexB protomer (Figure 3-9, colored by orange), whereas the MP domains of the SC protomers were located between each protomer of MexB (Figure 3-9, colored in magenta). Each protomer of MexB is in one of three different states in the crystal structure (Figure 3-14). On the other hand, the periplasmic gate of OprM is opened and the drug efflux route is secured unlike the crystal structure. State A and state B are quite similar ($C\alpha$ RMSD: 0.47); however, the relative positions of OprM in each state are related by a 60° rotation. Hereafter, I denote state A as the 0° state and state B as the 60° state.

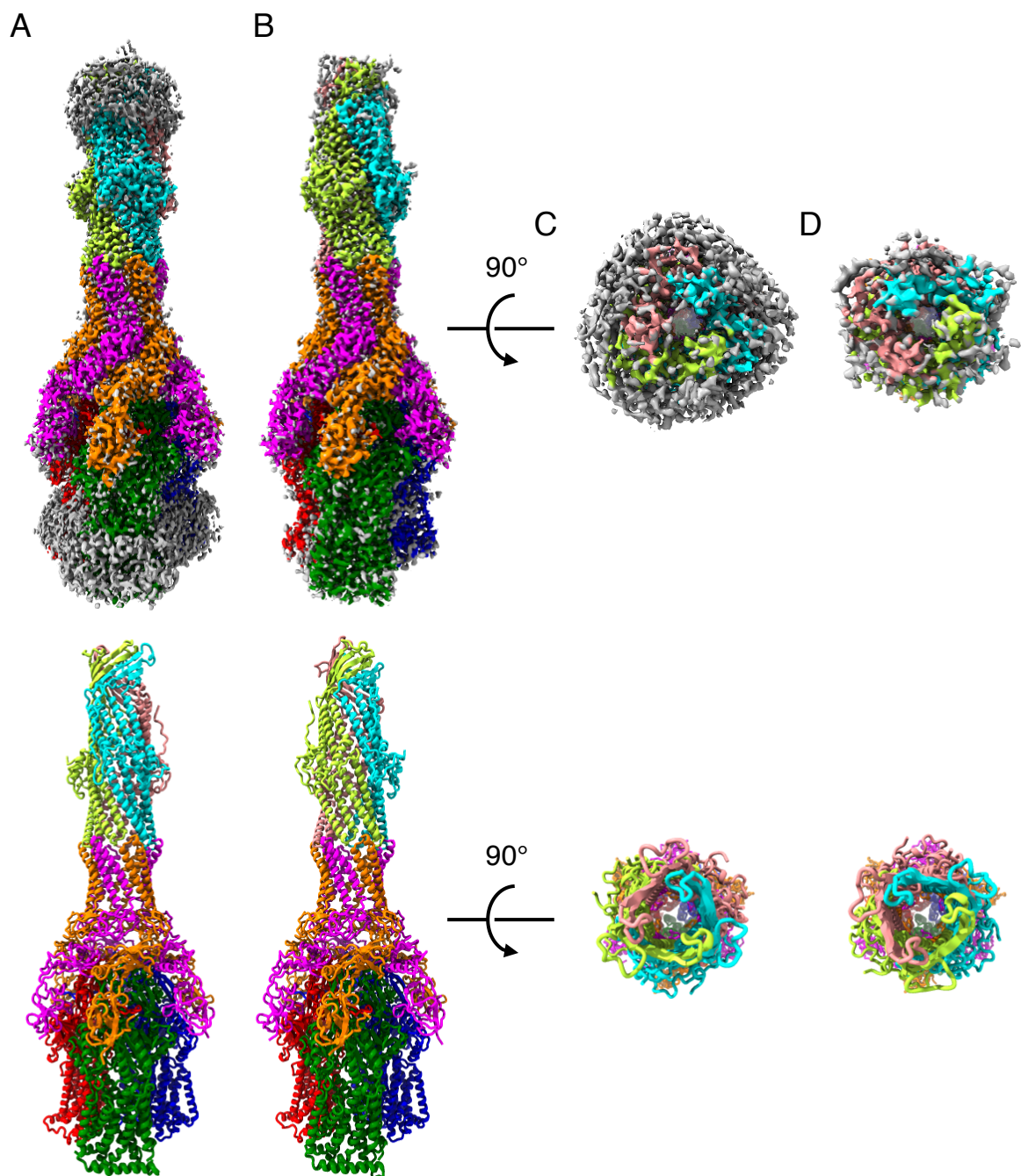


Figure 3-9 Overall structure of MexAB–OprM

Single-particle Cryo-EM reconstruction (top) and model of MexAB–OprM (bottom) in the 0° state (A) or 60° state (B) viewed from the periplasmic space [(A) and (B)] or from the outside of the cell [(C) and (D)]. The OprM protomers are colored in cyan, salmon, and lemon. MexA protomers are colored in magenta (SC protomer) or orange (LC protomer). MexB protomers in the Access, Resting, and Extrusion states are colored in green, blue, and red, respectively.

3.3.2 Interaction between OprM and MexA

In the 0° state, H3-H4 of OprM face the α -hairpin tips of the LC protomers, whereas H7-H8 face the α -hairpin tips of the SC protomers. In the 60° state, on the other hand, H3-H4 of OprM face the α -hairpin tips of the SC protomers, and H7-H8 face the α -hairpin tips of the LC protomers. The C α RMSD between periplasmic tips of the OprM protomer (S188–E214: H3-H4; Y396–F422: H7-H8) is 1.1 Å, and the C α RMSD between α -hairpin domains of hexameric MexA (A74–F134) is 0.33 Å. The contact surface areas between the MexA hexamer and OprM trimer are 2992 Å² (0° state) and 2983 Å² (60° state). Several hydrogen bonds are present between main chains: Q104 in MexA binds to A203 or Y411 in OprM, and K108 in MexA binds to G199 or G407 in OprM (Figure 3-10 A and B). Also, L100 in MexA engages in hydrophobic interactions with V198 and V200 on H3-H4 or V408 on H7-H8. Moreover, the side chain of R403 in OprM extends inward from H7 and seems to form a hydrogen bond with the main chain of A105 in MexA. These results suggest that the two modes of binding between MexA and OprM do not differ significantly. In addition, the number of particles in the 3D classification of both states was not much different (Figure 3-2), and I conclude that these two binding modes exist equally within bacterial cells.

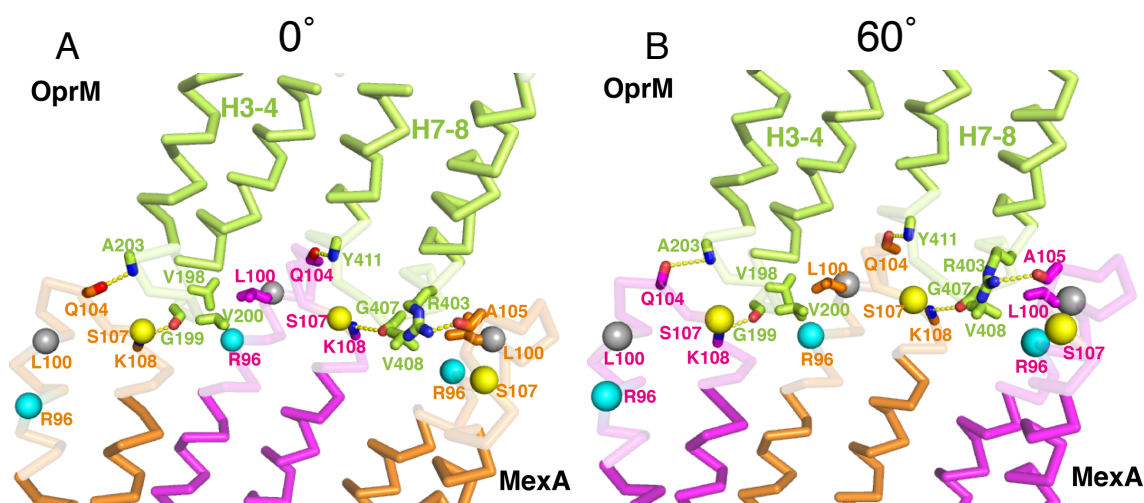


Figure 3-10 Interaction between OprM and MexA

Close up views of the α -hairpin of OprM (shown in lemon) and the α -hairpin of MexA [shown in magenta (SC protomer) or orange (LC protomer)] in the 0° state (A) or 60° state (B). Previously proposed RLS motifs are shown as balls colored in cyan (R96), gray (L100), and yellow (S107).

Regarding the interaction between OprM and MexA, several residues that were thought to be important for interactions, as well as a few models of complex formation, have been proposed based on previous mutation experiments and molecular dynamics (MD) simulations of tripartite efflux pumps^{88–93}. To identify the residues involved in complex formation, a functional analysis for residues previously proposed to be required^{89,92,93} or that seemed important based on the Cryo-EM structure was performed by my coworkers (Dr. Ryo Yonehara and Dr. Etsuko Ishizaka-Ikeda). Specifically, *in vitro* complex formation analysis using site-point mutation and SEC was performed (Supplementary Figure 1) and experiments to determine the *in vivo* survival assay was conducted (Supplementary Figure 2). Alanine mutations for G199 and G407 in OprM, which were proposed to be critical residues in a previous study⁹², completely abolished complex formation. These glycine residues are located at equivalent positions between

the H3-H4 and H7-H8 loops, and the main chains of these glycine residues and the K108 residue of MexA were at a distance suitable for formation of a hydrogen bond (Figure 3-10). Aspartate mutation of the L100 residue of MexA, one of the RLS motifs proposed to be important for complex formation of MFP based on structural analysis of AcrAB–TolC^{77,89}, also completely abolished complex formation and drug resistance (Supplementary Figures 1 C and 2). By contrast, aspartate mutation of the adjacent residue L99 had no effect on complex formation, highlighting the importance of L100. Because L100 contacts H3 or H7 of OprM from the side, and its side chain is close to V200 on H3 or V408 on H7 (Figure 3-10), I speculated that L100 binds MexA and OprM via hydrophobic interactions. R403 of OprM, not previously proposed to be important, was critical for complex formation: alanine mutation at this position abolished complex formation (Supplementary Figure 1 D). S107 in MexA, one of the RLS motifs, was also proposed to be important residue based on MD simulation⁹³. Although aspartate mutation of this residue disrupted complex formation and decreased drug resistance in the survival assay, I could confirm no specific interaction of S107 in Cryo-EM structure. The side chain of S107 is located at the narrow gap between MexA tip and OprM tip (4–5.5 Å), so the inhibition of complex formation ability by the aspartate mutation is thought to be due to steric hindrance of the side chain. Like L100 and S107, the remaining RLS motif, R96, is also conserved, but its alanine mutants formed a complex as efficiently as the wild type. By contrast, aspartate mutation at this residue decreases its minimum inhibitory concentration (MIC) experiments⁸⁹, consistent with the experimental results (Supplementary Figure 2), and also diminished complex formation. Based on these results, I can conclude that R96 in MexA is not essential for complex formation, and that the decrease in complex-forming ability caused by the

aspartate mutation was due to charge repulsion. Furthermore, D103 and Q104 in MexA were predicted to be important for complex formation based on previous MD simulations⁹³; however, alanine mutations of these residues did not show significant effects in either *in vitro* or *in vivo* functional analysis (Supplementary Figures 1 C and 2). Therefore, the tip-to-tip interaction of MexA and OprM is based mainly on the interaction between the main chains, such as Q104–A203 or -Y411 and the aforementioned K108–G199 or -G407 (Figure 3-10). In addition, the interactions between the side faces of OprM and MexA, such as the hydrophobic interaction centering on L100 in MexA or the hydrogen bond between the side chain of R403 in OprM and the main chain of A105 in MexA, are also essential for complex formation.

3.3.3 Interaction between each MexA protomer

Except for the MP domains, the MexA hexamer has C₆ symmetry, and is formed by arrangement of the β -barrel domains in a ring shape via electrostatic interactions (area of contact surface: 1254 Å²). For example, R39 or R147 interacts with E152 or E226 of the adjacent protomer (Figure 3-11). Repelling charge mutations (R39D or R147D) prevented complex formation, as determined by SEC experiments (Supplementary Figure 1 B), and decreased drug resistances in the survival assay (Supplementary Figure 2). The hexameric assembly in the lipoyl and β -barrel domains were similar to those in MacA, an MFP of the ABC-type multidrug efflux pump MacAB–TolC in *E. coli*, which forms hexamer in the single crystal structure⁹⁴.

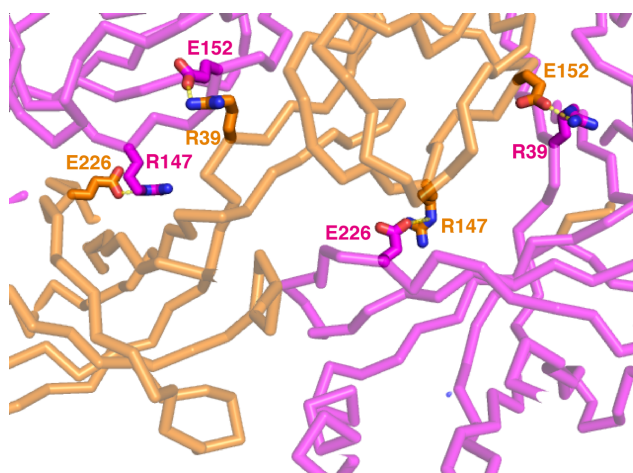


Figure 3-11 Detailed views of the MexA–MexA

Detailed view of the lipoyl domains of MexA [shown in magenta (SC protomer) or orange (LC protomer)]. Side chain atoms of residue pairs identified in Cryo-EM model of complex formation are shown as stick models.

3.3.4 Interaction between MexA and MexB

MexA and MexB have two interacting faces: the β -barrel domain of MexA with the FL domain of MexB, and the MP domain of MexA with the porter domain of MexB. The interaction area between the β -barrel and FL domains is about 600 \AA^2 , and did not differ significantly between the SC and LC protomers. However, the area of the MP domain and porter domain was significantly different: $\sim 360 \text{ \AA}^2$ for the SC protomer vs. $\sim 860 \text{ \AA}^2$ for the LC protomer. Note that there is little difference in these interactions regardless of the states of MexB.

For complex formation between the SC protomer and MexB, I observed two specific interactions in the Cryo-EM structure. The key loop (L252–V260), located at the top of the FL domain of MexB, shifts onto the side of the adjacent protomer in comparison with the crystal structure, and sticks in the hollow formed by the β -barrel domain of the SC protomer (Figure 3-12 A). The side chains of R34 and T233 in this hollow are

positioned at a distance suitable for formation of a hydrogen bond, with the carbonyl groups of P255 or N254 and S258 located in the key loop. In addition, the side chain of R277 in the MP domain is about 3 to 4 Å from the side chain of E244 in MexB, sufficient to form a hydrogen bond (Figure 3-12 B). Indeed, the alanine or aspartate mutant of R34 or R277, as well as the alanine or valine mutant of T233, lost the ability to form a complex (Supplementary Figure 1 A and E). These mutations also decreased drug resistance, as determined by in the survival assay (Supplementary Figure 2). Therefore, I can conclude that these three residues are essential for SC protomer binding. On the other hand, in the LC protomer, the entire MP domain faces PC1 of MexB, forming an interaction across the entire plane (Figure 3-12 C). PC1 undergoes no conformational change relative to the crystal structure except for a shifted helix (M653–A661), which was pushed out by F328 in the LC protomer (Figure 3-12 D).

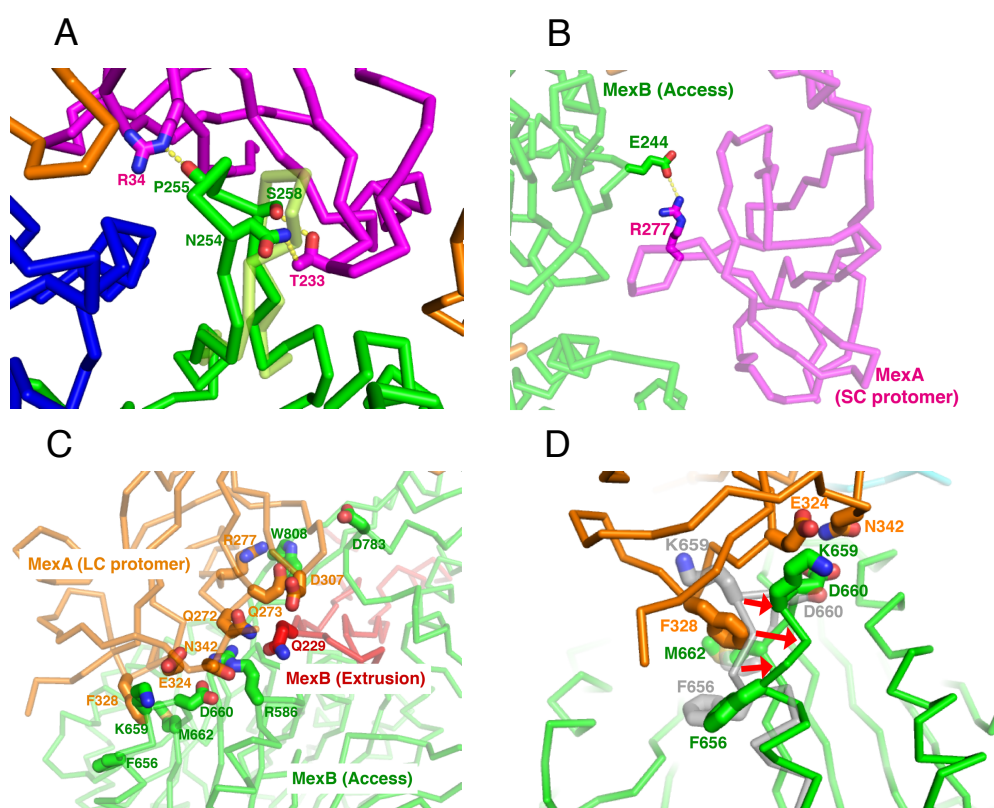


Figure 3-12 Detailed views of MexA–MexB interactions

(A) Close-up view of the interaction between the FL domain in MexB (green) and the SC protomer (magenta). The key loop in the crystal structure (PDB ID: 3w9i) is shown in transparent lemon. Side chain atoms of critical residues identified in the complex formation experiment are shown as stick models. (B) Interaction between the porter domain of MexB (green) and the SC protomer (magenta). (C) and (D) Interaction between the PC1 domain (green) and LC protomer (orange) viewed from the side of PC1 (C) or top of PC1 (D). The adjacent MexB protomer is shown in red. The shifted helix from the crystal structure of MexB in the Access state is shown in gray. The red arrow indicates a movement of shifted helix.

3.3.5 Comparison between the closed and open structures of OprM

In the crystal structure of isolated OprM (PDB ID: 3d5k), the periplasmic gate is closed by the hydrophobic interaction of L412 between the protomers and the salt bridge between D416 and the adjacent R419⁷³. In the protomers, the side chains of S188

and T192 on H3 form a hydrogen bond with R405 on H7. In the Cryo-EM structure, H3-H4 opens $\sim 9^\circ$ compared to the crystal structure with T178 and Q222 acting as the fulcrum, and the hydrogen bond with the side chain of R405 disappeared (Figure 3-13 A and B). Also, H7-H8 rotated $\sim 19^\circ$, with R376 and R432 as the fulcrum. Consequently, the C α atom of L412 moved 11.4 Å outward, and the salt bridge between R419 and D416 disappeared.

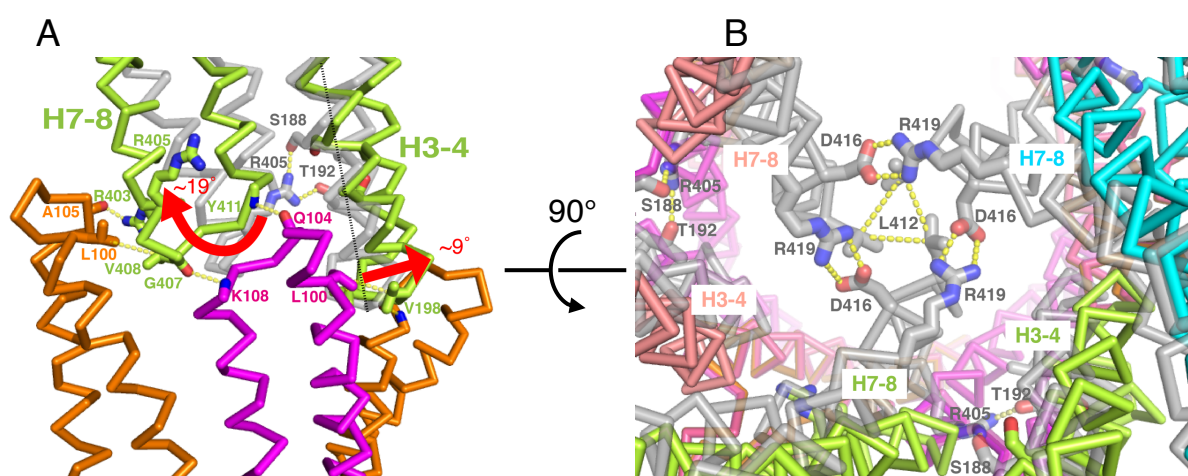


Figure 3-13 Comparison of OprM in the crystal structure and Cryo-EM structure

Superposition of the OprM crystal structure (PDB ID: 3d5k, gray) and Cryo-EM structure (0° state, colored according to Fig. 3-9) viewed from the periplasmic space (A) or from outside the cell (B). Red arrows indicate helix movements of H3-H4 or H7-H8 from the closed crystal structure to the open Cryo-EM structure.

3.3.6 Comparison between the crystal structure and Cryo-EM structure of MexB

In apo-state structures, MexB is asymmetric: specifically, the structures of the FL domain (excluding the key loop) and the TM domain were very similar to the Access, Bind, and Extrusion states in the previously reported crystal structures (Figure 3-14). By

contrast, with respect to the porter domain, although the Access and Extrusion states are very similar, except for shifted helices, a slight difference can be observed in the protomer corresponding to the Bind state. Compared to the crystal structure, PC2 is shifted by ~ 3 Å toward PC1 and the cleft between PC1 and PC2 does not exist (Figures 3-15 and 3-16 A). Also, because PC2 approaches PC1, the gate loop (G675–F680) connecting PC1 and PC2 is bent upward, and N676 interacts with F617 on the switch loop (Figure 3-15). Note that a similar interaction is observed in the Extrusion state in the MexB crystal structure. Consequently, in the Cryo-EM structure, all three MexB protomers are closed toward the outside, representing a state that cannot accommodate drug molecules. Based on this evidence, I concluded that this is a “resting state” in which drug efflux does not occur.

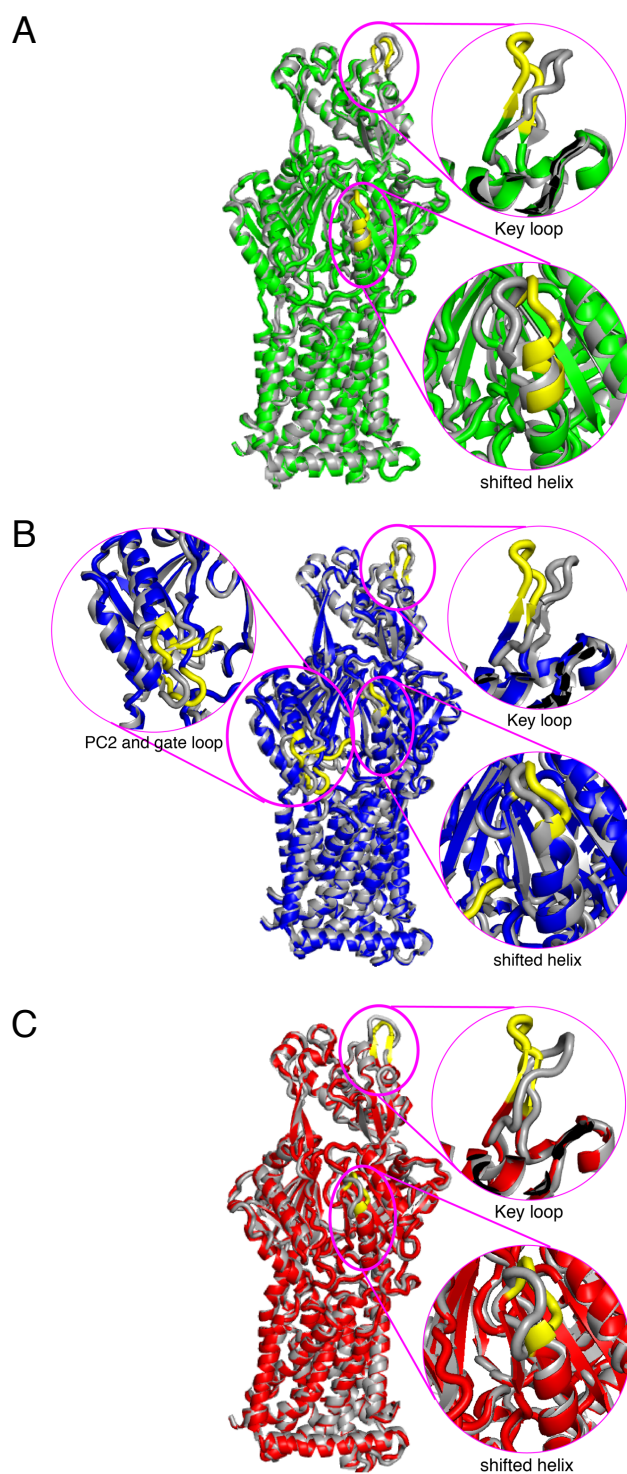


Figure 3-14 Comparison of individual MexB protomers in the apo-MexAB-OprM or isolated crystal structure Superposition of each MexB protomer in the crystal structure (PDB ID: 3w9i) and complex structure (apo-state, 0°). (A) Superposition of Access protomers in the apo-MexAB-OprM (green) and the crystal structure (gray). (B) Superposition of the resting protomer in apo-MexAB-OprM (blue) and the Binding protomer in the crystal structure (gray). (C) Superposition of Extrusion protomers in apo-MexAB-OprM (red) and the crystal structure (gray).

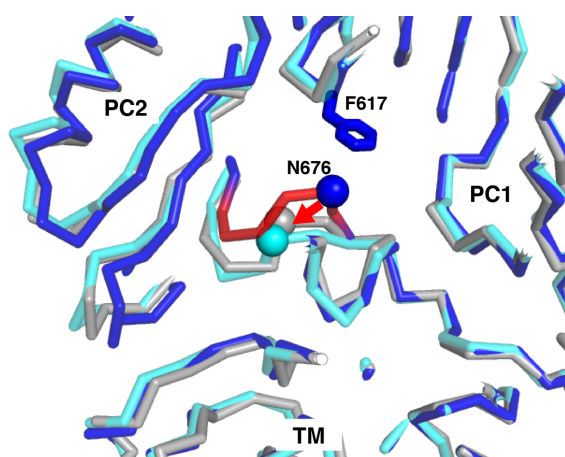


Figure 3-15 Conformational change of MexB from the Resting state to the Binding state

Superposition of the Resting state in the Cryo-EM structure (blue), the Binding state in the crystal structure (PDB ID: 3w9i, gray), and the Binding state in the Cryo-EM structure (cyan). Gate loops are colored in red. Red arrows indicate conformational changes of the gate loop.

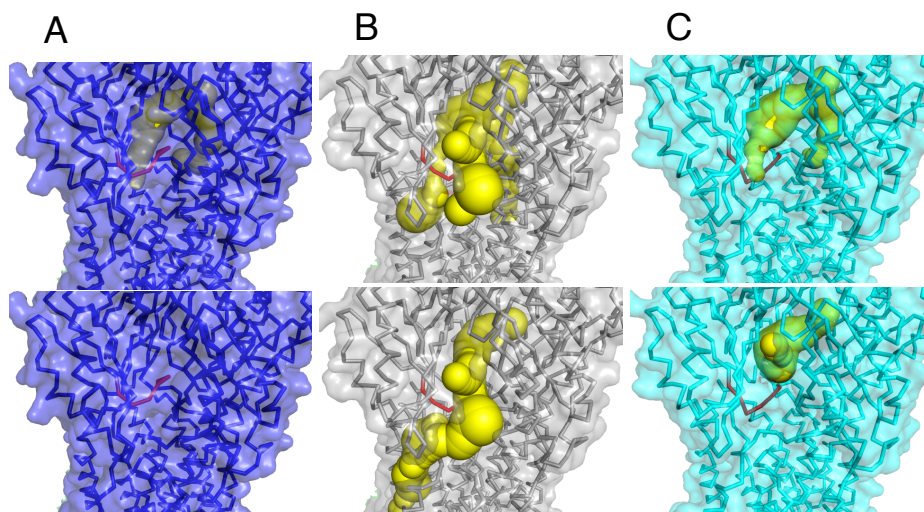


Figure 3-16 Visualization of channels

Visualization of channels to the distal binding pocket, generated using *caver* v. 3.0.1⁹⁶. Shown are the Resting state in the Cryo-EM structure (A), the Binding state in the crystal structure (B), and the Binding state in the Cryo-EM structure (C). Channels are shown as yellow spheres with diameters greater than 1.6 Å (top panels) and 2.0 Å (bottom panels). Atomic models are shown in ribbon diagram, and surface views are transparent with the same color as in (Figure 3-15). Gate loops are colored in red.

3.3.7 MexAB–OprM in the presence of drug

To determine how the presence of drug affects the structure of MexAB–OprM, I added novobiocin (NOV), an aminocoumarin antibiotic, to the sample to create a grid for Cryo-EM. Data collection and single-particle analysis were performed in the same manner as for the drug-free state, and maps with resolutions of 3.5 Å (0° state) and 3.6 Å (60° state) were acquired (Figure 3-3). The structural validations of maps and models of MexAB–OprM in NOV-binding state were examined as a same manner of MexAB–OprM in apo-state (Figure 3-15 and Table 2). Overall, each structure is very similar to the corresponding drug-free structure, with large differences only at the gate loop and the PC2 domain of the Bind protomer of MexB. In the presence of NOV, the corresponding MexB protomer is similar to the crystal structure; the PC2 opened outward, the cleft between the PC1 and the PC2 opened, and the gate loop was stretched and descended (Figure 3-15 and 3-16 C). In addition, a density corresponding to NOV appears in the distal binding pocket (Figure 3-18).

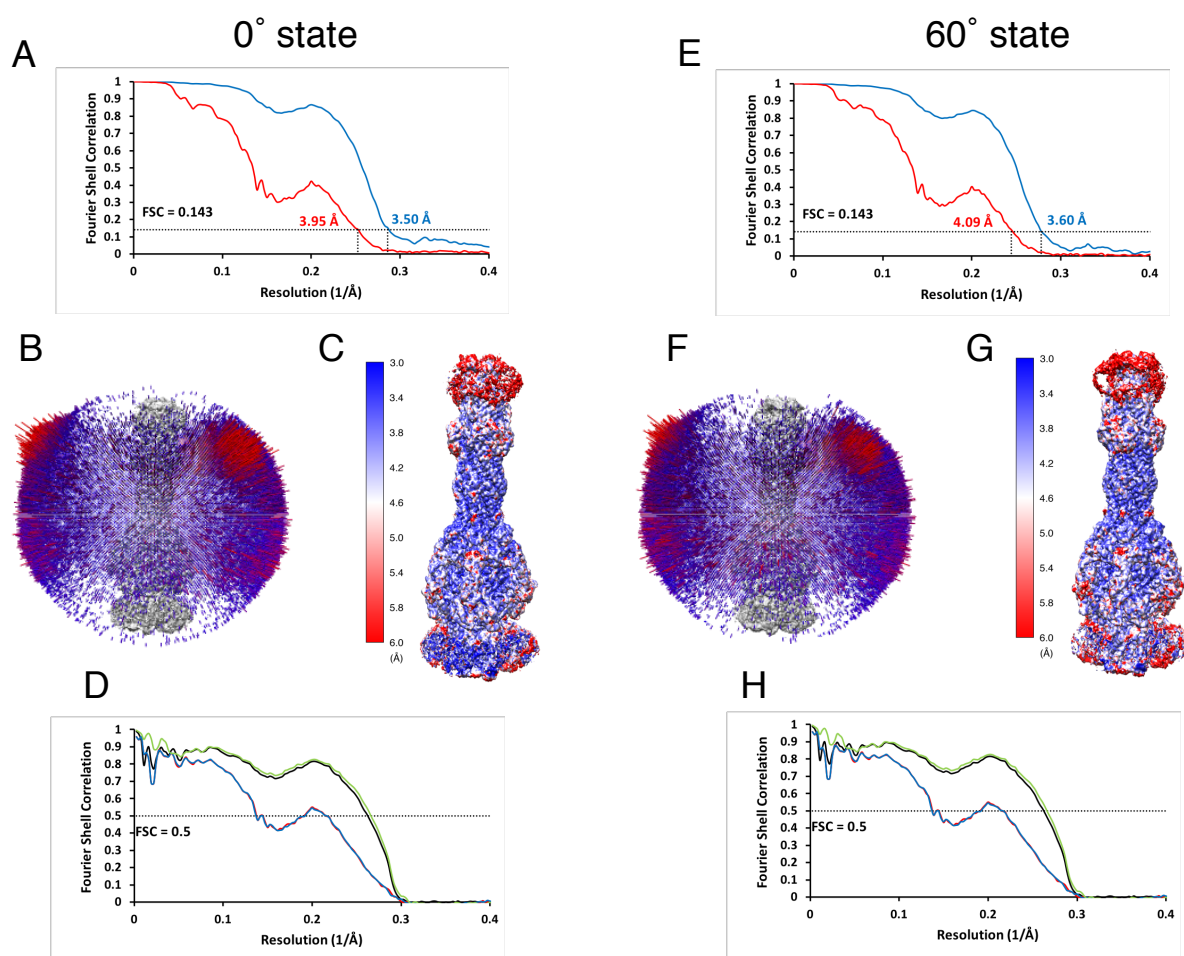


Figure 3-17 Structural validations for MexAB-OprM in NOV-binding state

Maps and model validation of the 0° state (A–D) and 60° state (E–H) of the NOV-binding state of MexAB-OprM. (A, E) FSC curves before (red) and after (blue) postprocessing. (B, F) Angular distribution histograms. (C, G) Local resolution estimation calculated using ResMap. (D, H) FSC curves for final model versus final *locscale* map (black), masked map (green), half map 1 (red), and half map 2 (blue), respectively.

Table 2. Summary of NOV-binding state MexAB–OprM structures

	NOV binding state (0°)	NOV binding state (60°)
Data collection and processing		
Microscope	FEI Titan Krios	
Magnification	59,000x	
Voltage (kV)	300	
Electron exposure (e ⁻ /Å ²)	40	
Detector	FEI Falcon III (linear mode)	
Pixel size (Å/pixel)	1.125	
Defocus range (µm)	-1.25 to -2.5	
Number of used micrographs	4,681	
Initial number of particles	902,901	
Final number of particles for reconstruction	31,409	31,466
Symmetry imposed	C1	C1
Box size (pixels)	320	
Map resolution (Å)	3.50	3.60
FSC threshold	0.143	0.143
Refinement		
Model composition		
Number of non-H atoms	49,126	49,126
Protein residues	6,453	6,453
Ligands	1	1
B factors (Å ²)		
Proteins	88.04	96.24
Ligands	87.92	20.00
R.M.S deviations		
Bond lengths (Å)	0.017	0.006
Bond angles (°)	1.130	1.107
Ramachandran plot		
Favored (%)	93.62	94.46
Allowed (%)	6.38	5.54
Outliers (%)	0	0
Validation		
MolProbity score	1.71	1.64
Clashscore	5.38	5.03
Poor rotamers (%)	0.96	0.83
Model resolution (Å)	3.83	3.87
FSC threshold	0.5	0.5
Real Space CC	0.766	0.770

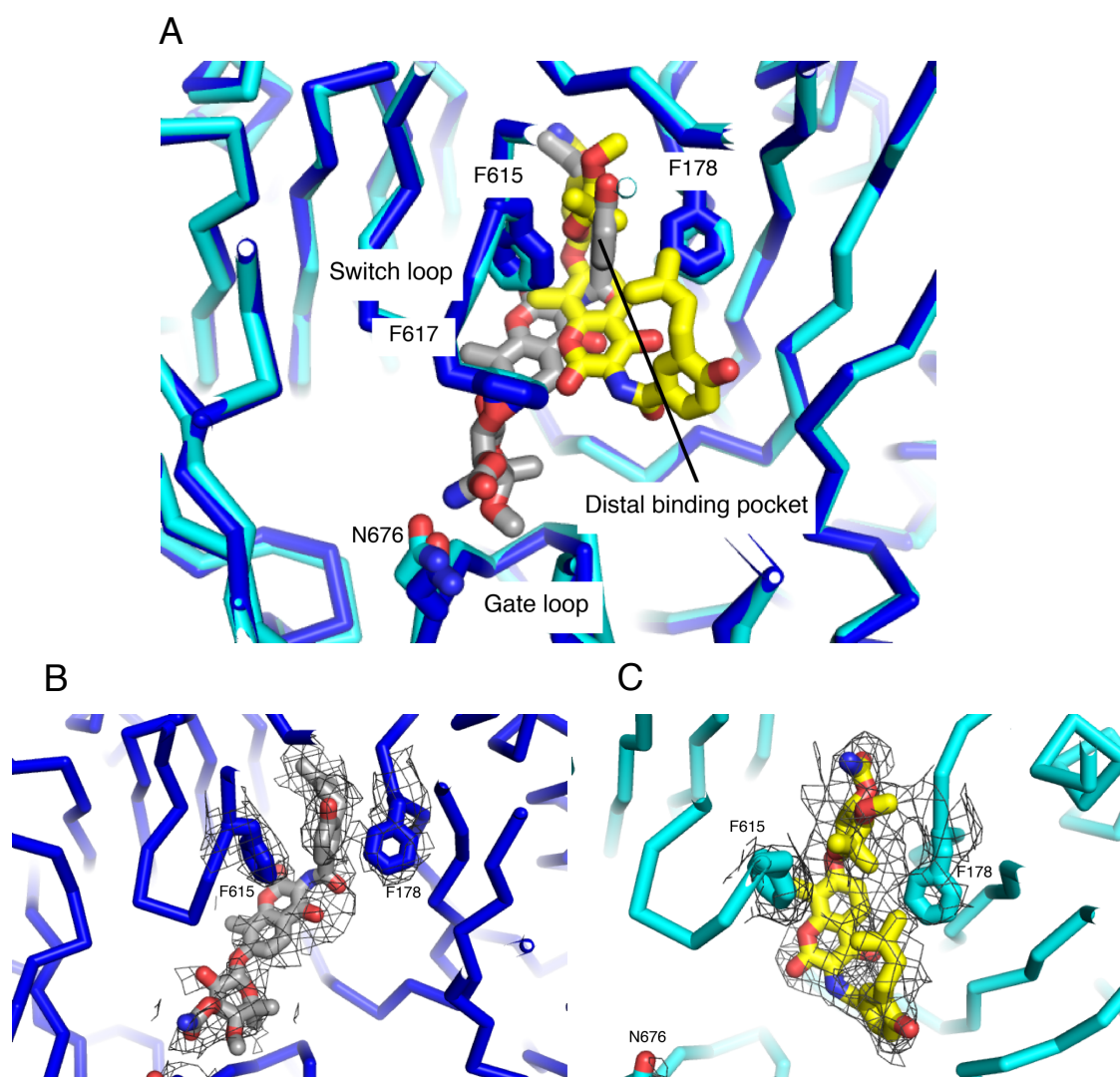


Figure 3-18 Binding modes in the distal binding pocket of the NOV-binding state.

(A) Superposed view of the distal binding pocket of the MexB protomer in the Binding state in the 0° state (blue) and the 60° state (cyan). Models of novobiocin are shown in gray (0° state) and yellow (60° state). (B) and (C) Map and model fit around novobiocin in the 0° state (B) and the 60° state (C). Cryo-EM map within 1.6 Å around novobiocin, shown as a gray mesh contoured at 3.0 σ . Models are colored as (A).

3.4 Discussion

In Cryo-EM structure, OprM exhibits two types of binding states in both the presence and absence of the drug. When OprM states were separated in single-particle analysis, the ratio of particles in the 0° vs. 60° states was 45:55 (in the absence of drug) and 58:42 (in the presence of novobiocin), suggested an overall ratio of nearly 1:1. MexB, which is embedded in the inner membrane, and MexA, which is anchored to the inner membrane, can move freely on the inner membrane, whereas OprM, which penetrates the hard outer membrane, is remarkably restricted in terms of lateral movement and rotation. The presence of two binding modes in OprM is likely to increase the chances of contact between MexA and OprM.

In the crystal structure of OprM alone, the periplasmic gate is closed, whereas in the complex structure obtained by Cryo-EM, the gate is open. In *E. coli* AcrAB–TolC, a structure of the complex structure in which TolC is closed has been reported, but in my single-particle analysis, I could not observe such a complex. Based on my native complex structure and mutagenesis experiments, I propose the following mechanism by which OprM opens while binding MexA:

The side face of the H3 helix in OprM and residue L100 in MexA clash when the crystal structure of OprM and the Cryo-EM structure are superposed (Figure 3-13 A). Because the functional analyses showed that L100 is essential for complex formation, and H3-H4 opens slightly outward in the Cryo-EM structure, clash between L100 and H3-H4 may be responsible for the initial movement. After H3-H4 is pushed out by L100, and the tip of H3-H4 interacts with the confronting α -hairpin tip of MexA (Figure 3-19, 2). Subsequently, hydrogen bonds between H3 and H7 (S188 or T192–R405) in the protomer are broken by opening H3-H4 (Figure 3-19, 3). Meanwhile, H7-H8

becomes unstable, causing the hydrophobic interaction of L412 and the D416–R419 salt bridge between protomers to be broken; consequently, H7-H8 starts to rotate dramatically (Figure 3-19, 4). This rotation is stopped by a side interaction with MexA, which is fixed by a tip-to-tip interaction with H3-H4 on the left adjacent protomer (due to a hydrophobic interaction of L100 in MexA or the hydrogen bond between A105 in MexA and R403 in OprM). Finally, by interacting with the side of H3-H4, a tip-to-tip interaction forms between H7-H8 and the fixed MexA α -hairpin (Figure 3-19, 5). As a result, OprM with a fully opened periplasmic gate is formed.

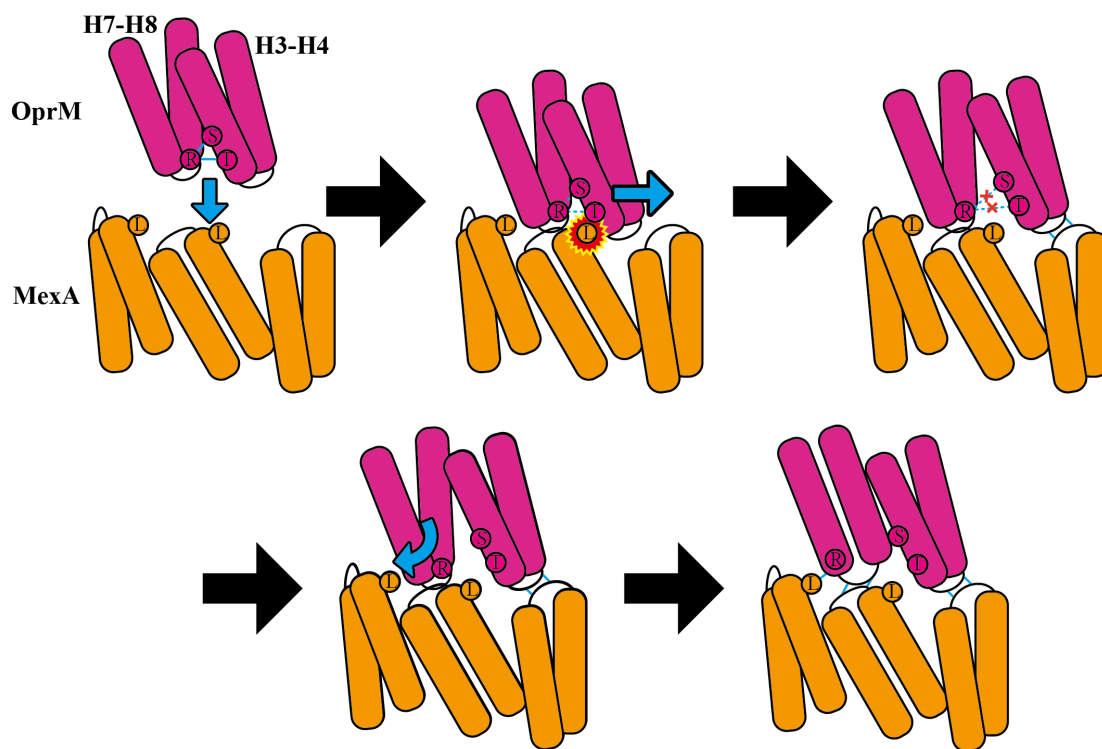


Figure 3-19 A model of OprM channel opening

Schematic cartoon of the channel-opening mechanism of OprM. Enclosed letters with circles indicate critical residues for channel opening and complex formation: L indicates L100 in MexA, and S, T, and R indicate S188, T192, and R405 in OprM, respectively.

Based on the results of this study, I propose a mechanism for MexAB–OprM complex formation and a model for drug efflux, as follows. In the complex formation experiment, SEC peak shifts were observed for MexA and MexB, but not for MexA and OprM or OprM and MexB (Figure 3-20), indicating that the MexA–MexB complex is formed first. MexA is sequentially bound by MexB via interactions between the MP and β -barrel domains in MexA and the FL domain in MexB, and the bound MexA engages in mutual interactions between lipoyl domains to form a hexameric ring, resulting in formation of the MexA–MexB intermediate (Figure 3-21A). When OprM comes in contact with the ring formed by the α -hairpin domain of the MexA hexamer, MexA L100 clashes with the H3 helix in OprM, and the H3-H4 helix is pushed outward (Figure 3-21 B). After that, as described above, the H7-H8 helix rotates, the interaction between the OprM trimer and the MexA hexamer is completed, and the periplasmic gate opens (Figure 3-21 C and D). When the surrounding drug concentration becomes high, the gate loop of MexB shifts downward, and the binding pocket is opened to the molecular surface. After that, MexB ejects drugs into the tunnel of MexA–OprM via a functional rotation mechanism. When the concentration of drugs in this tunnel becomes higher than their concentration outside the cell, they diffuse out of the cell via the concentration gradient (Figure 3-21 E). As the concentration of drug in the cell decreases, the drug entrance of the binding protomer of MexB is closed by the structural change of the gate loop, and the complex shifts from the Binding state to the Resting state. Under these conditions, because the pump is completely closed to the periplasm, backflow of drugs is prevented. When the concentration of drug in the environment rises, the resting protomer again undergoes a structural change to the binding state, and drugs are taken in and released.

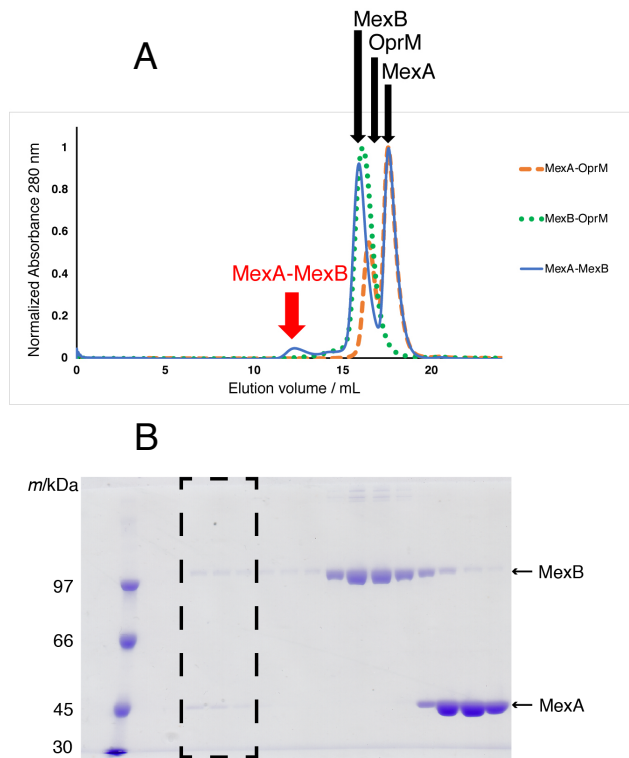


Figure 3-20 Reconstruction of the MexA–MexB complex.

(A) SEC charts of samples dialyzed in the same manner as in the complex formation experiment, except that only MexA and MexB (blue), MexA and OprM (orange), or MexB and OprM (green) were present. Red arrow indicates a peak corresponding to the MexA–MexB complex. (B) SDS-PAGE of fractions of the MexA–MexB sample. A black dashed box indicates fractions corresponding to the peak shown in (A)

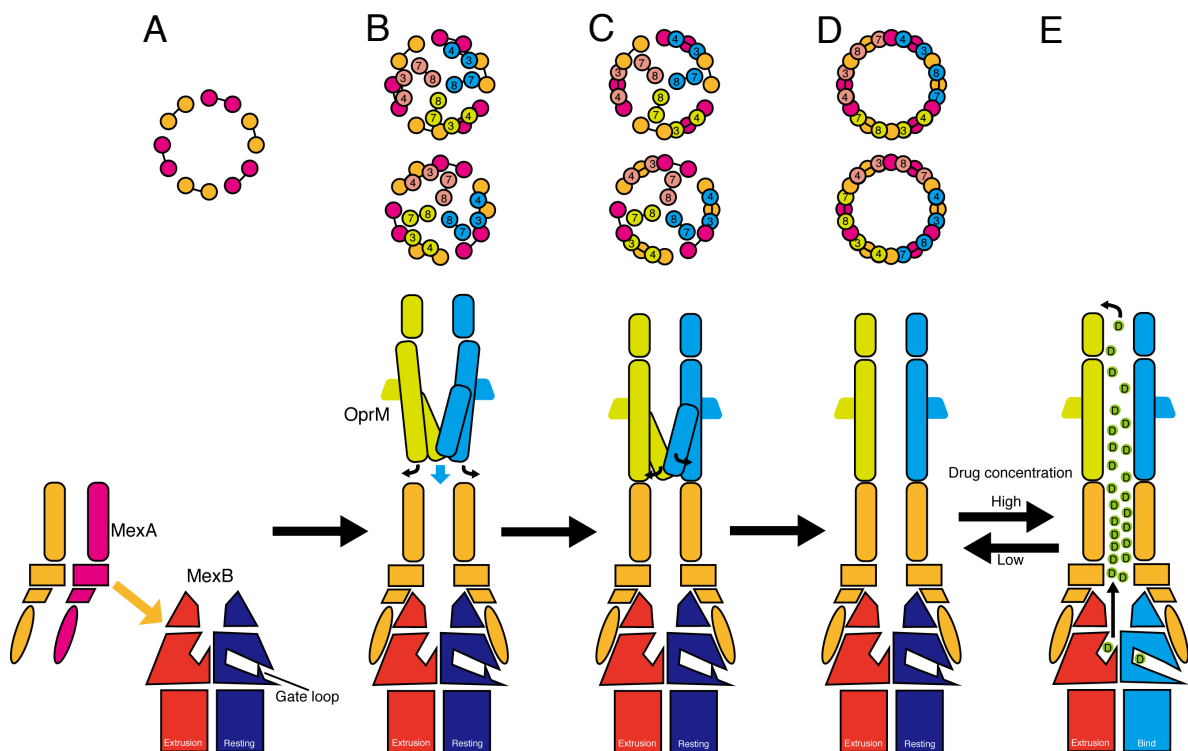


Figure 3-21 Proposed model for complex formation and drug efflux by MexAB–OprM Sectional views of the MexA–OprM interaction surface section in the 0° state (top panels) and 60° state (middle panels), and views from the periplasmic space of the complex in the 0° state (bottom panels). Each protomer is colored as in Fig. 3-9. (A) Six MexA protomers bind to the MexB trimer and form a hexameric tube. (B) The closed OprM trimer interacts with the MexA hexamer by opening the H3-H4 helices. (C) The H7-H8 helices revolve outward and are trapped against the side of MexA via hydrophobic interactions. (D) Formation of the fully opened MexAB–OprM pump is completed. (E) Depending on the drug concentration, the resting protomer in MexB changes its conformation, resulting in formation of the Binding state. Drugs are taken into MexB and pass through the MexA–OprM tube, and are then ejected outside the cell according to their concentration gradients.)

3.5 Conclusion

In *P. aeruginosa*, MexAB-OprM plays a central role in multidrug resistance by ejecting various drug compounds, resulting in serious nosocomial infections. Although the structures of the components of MexAB-OprM have been solved individually by X-ray crystallography, no structural information for fully assembled pumps from *P. aeruginosa* were previously available. In this study, I solved the structure of wild-type MexAB-OprM in the presence or absence of drugs at near-atomic resolution by Cryo-EM single-particle analysis.

The overall structure of MexAB-OprM is similar to AcrAB-TolC. OprM does not interact with MexB directly, and six protomers of MexA are divided into SC protomer and LC protomer depending on the way of interaction with MexB.

The single-particle analysis allowed me to classify apo-state MexAB-OprM into two classes according to their binding manner of OprM. In both states, since almost the same interaction is observed and particles in a ratio of approximately 1: 1 are separated into each class in the single-particle analysis, it is considered that both states are present in the bacterial cells.

The Cryo-EM structure of MexAB-OprM revealed a detailed interaction between each protein. In particular, the key loop, located at the top of the FL domain of MexB, sticks in the hollow formed by the β -barrel domain of the SC protomer. In addition, it is considered that the side chain of R277 in the MP domain forms a hydrogen bond with the side chain of E244 in MexB and this hydrogen bond is essential for binding between the MexB and the SC protomer. On the other hand, in the LC protomer, the entire MP domain faces PC1 of MexB, forming an interaction across the entire plane.

Compared to the crystal structure, the gate loop, located between the PC1 and PC2 of MexB protomer in Binding state of apo-state MexAB–OprM, bent upward and was located in the vicinity of the switch loop. Consequently, in the Cryo-EM structure, all three MexB protomers are closed toward the outside, representing a state that cannot accommodate drug molecules. To determine how the presence of drug affects the structure of MexAB–OprM, I determined the structures of NOV-binding state MexAB–OprM. In the presence of NOV, the corresponding MexB protomer is similar to the crystal structure; the PC2 opened outward, the cleft between the PC1 and the PC2 opened, and the gate loop was stretched and descended. Therefore, I propose the drug efflux model that the gate loop changes its conformation according to the concentration of drug in the cell to prevent backflow of drugs.

From the comparison with the crystal structure, I considered the mechanism by which OprM opens its gate while interacting with MexA. Finally, based on the results of this study, I propose the complex formation model of MexAB–OprM. Through this study, I could show important findings that clarify the functional mechanism of multidrug efflux pump of *P. aeruginosa*.

3.6 Supplementary information

3.6.1 Supplementary methods

(The following experiments were held by Dr. Ryo Yonehara and Dr. Etsuko Ishizaka-Ikeda.)

3.6.1.1 Complex formation experiment

Plasmids for each mutant were prepared by a standard PCR method. Expression, purification, and reconstruction of each mutant was performed as described above. Reconstruction experiments for MexA–MexB, MexA–OprM and MexB–OprM were performed as described for the reconstruction of MexAB–OprM, except for the omission of OprM, MexB, and MexA, respectively.

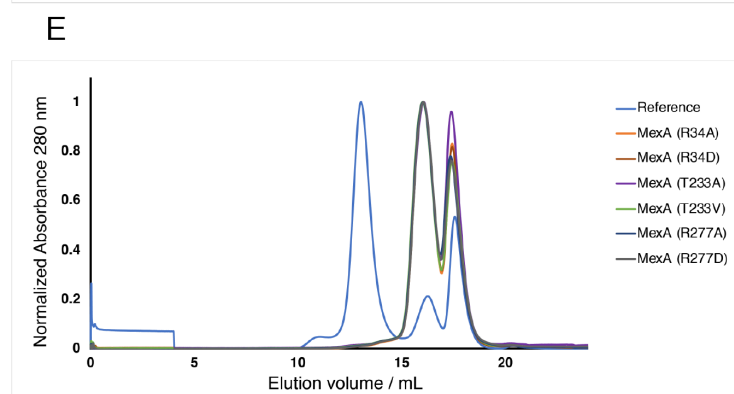
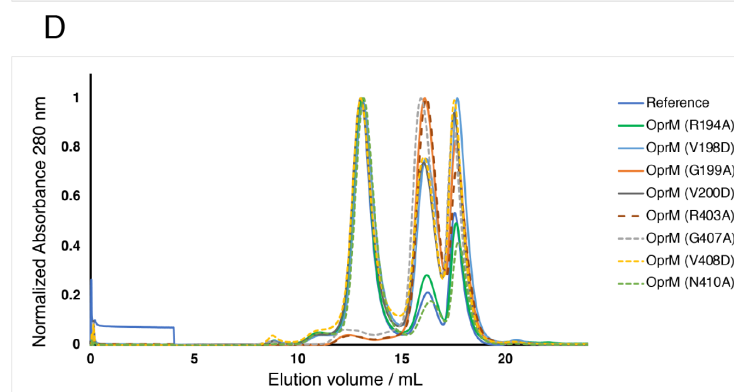
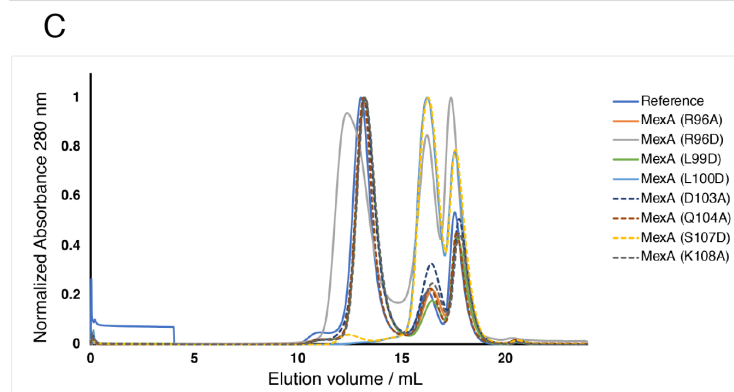
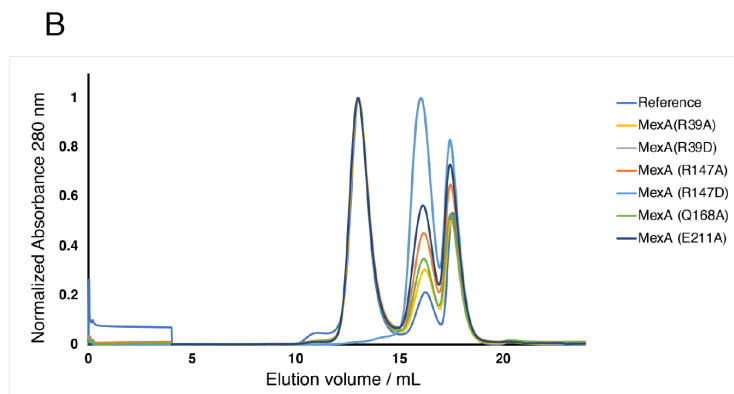
3.6.1.2 The *in vivo* survival assay

The genes of *mexA*, *mexB* and *oprM* were subcloned into the pMMB67HE vector. The mutants were prepared with a standard PCR method. The resultant plasmids were transformed into W3104 Δ *acrABD*. Bacterial cells were cultured overnight in 3 mL of LB medium supplemented with 100 μ g/mL of ampicillin (ABPC) at 37 °C. All of the cultures were adjusted to an OD_{590nm} of 1.0 with LB medium and then serially diluted with tenfold dilutions (10^{-1} ~ 10^{-6}). For each dilution series, 4 μ L of each strain was plated onto LB plates supplemented with 100 μ g/mL of ABPC and an additional antibiotic: none, 5 μ g/mL of chloramphenicol (CP), 25 μ g/mL of novobiocin (NOV), 5 μ g/mL of erythromycin (EM), 0.5 μ g/mL of minocycline (MINO), or rhodamine 6G (R6G). All plates were incubated at 37 °C overnight and then images were recorded.

3.6.2 Supplementary figures

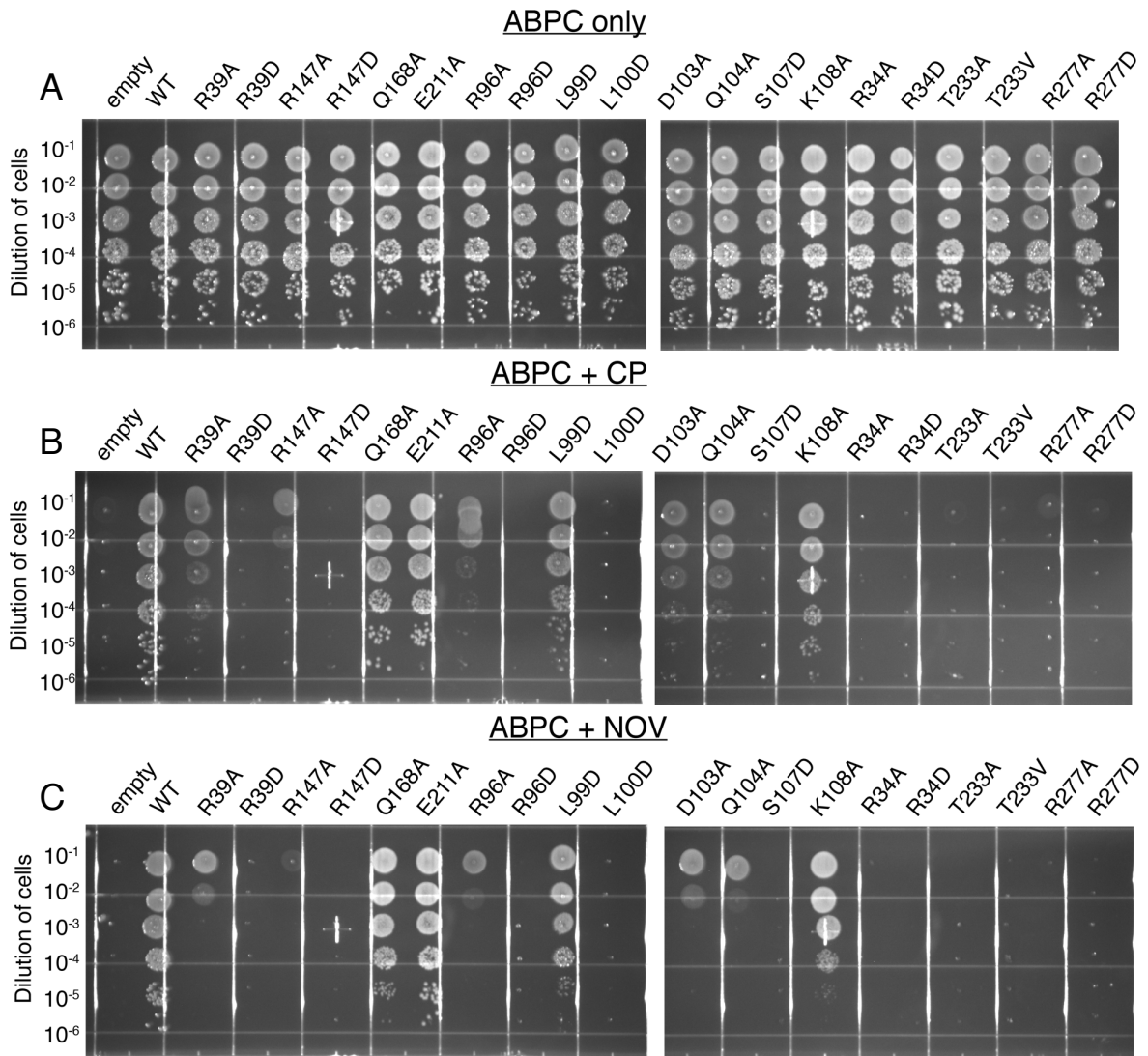
MexA-MexA interaction	MexA	R39A	○
		R39D	×
		R147A	○
		R147D	×
		Q168A	○
		E211A	○
MexA-OprM interaction	MexA	R96A	○
		R96D	△ ^{*1}
		L99D	○
		L100D	×
		D103A	○
		Q104A	○
		S107D	×
		K108A	○
	OprM	R194A	○
		V198D	○
		G199A	×
		V200D	○
		R403A	×
		G407A	×
		V408D	○
MexA-MexB interaction	MexA	R34A	×
		R34D	×
		T233A	×
		T233V	×
		R277A	×
		R277D	×

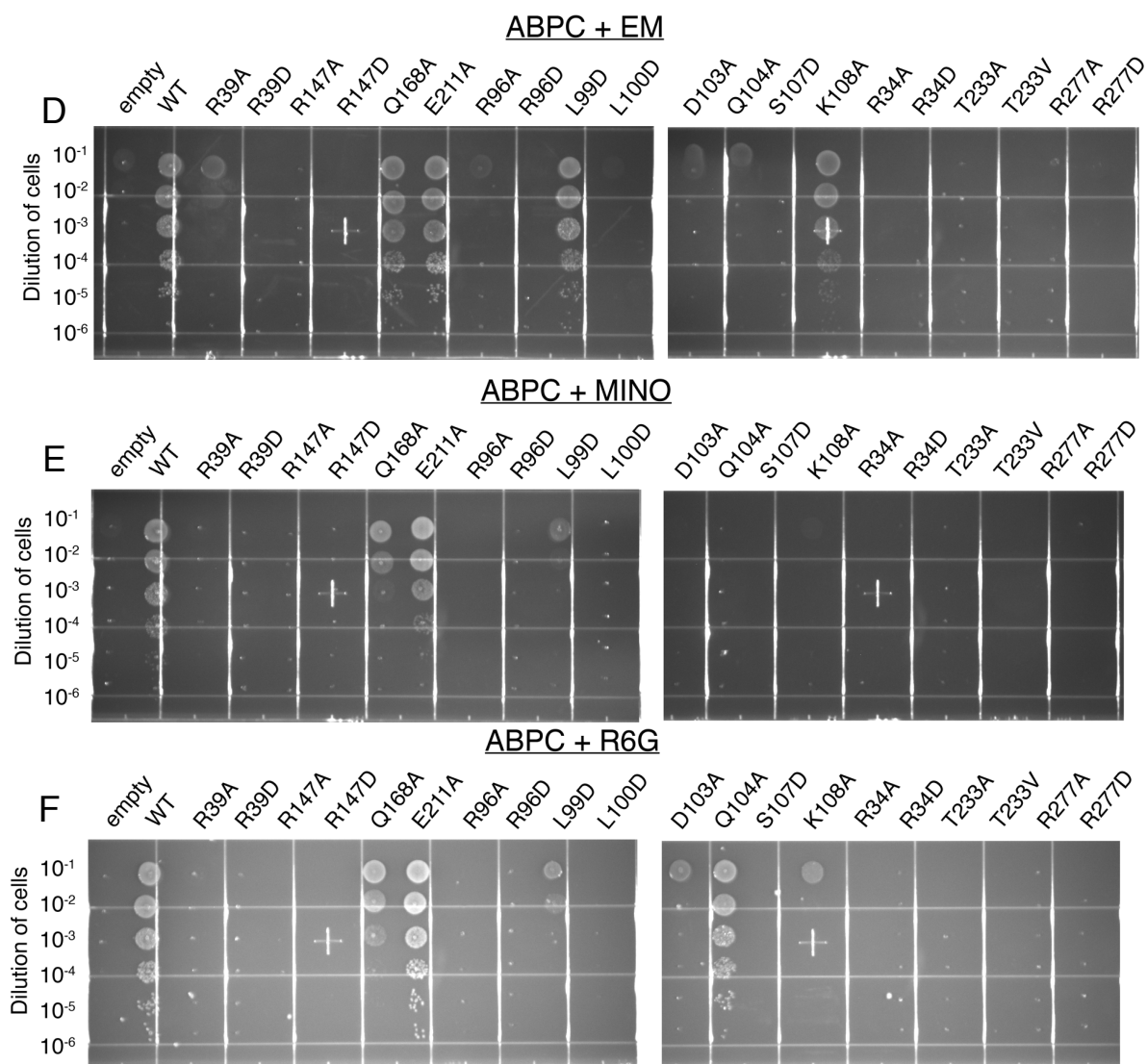
*1: The efficiency for complex formation was decreased.



Supplementary **Figure 1 Complex formation experiment with point mutation and SEC**

(A) Summary of the complex formation experiment. Leftmost panels show the interaction surfaces to which each residue is related. Middle left panels represent mutated proteins. Middle right panels show the type of mutation added to each residue. Rightmost panels show the results of complex formation. A circle indicates that the complex formed in the same way as the wild-type. An \times indicates that no complex was formed. A white triangle indicates that the efficiency of complex formation was reduced. A black triangle indicates that the stability of the reconstructed MexAB–OprM complex was reduced. (B)–(E) SEC chart of residues in MexA involved in the MexA–MexA interaction (B), the MexA–OprM interaction (C), residues in OprM (D), and residues in MexA involved in the MexA–MexB interaction (E).

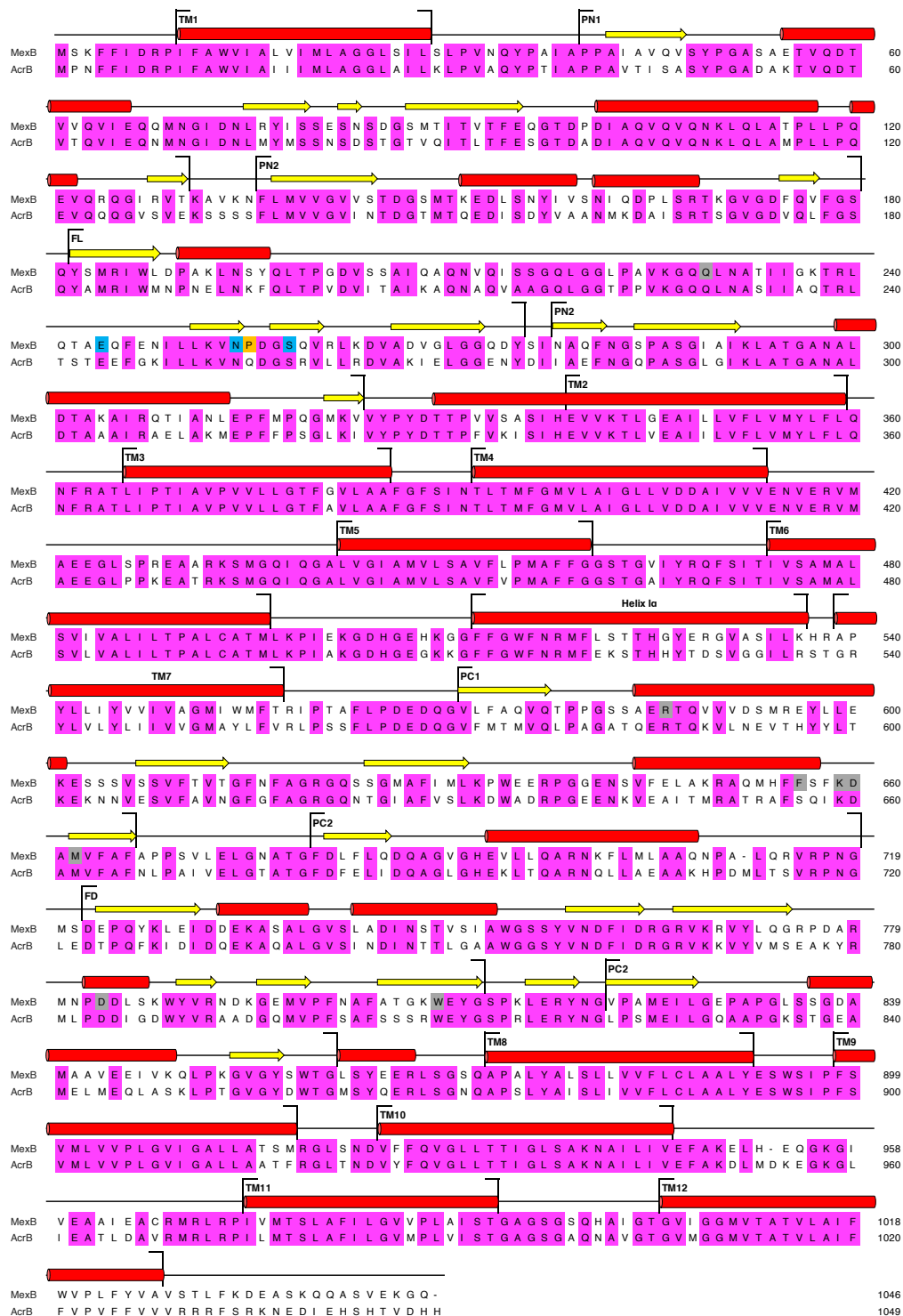




Supplementary Figure 2 The survival assay using MexA mutants

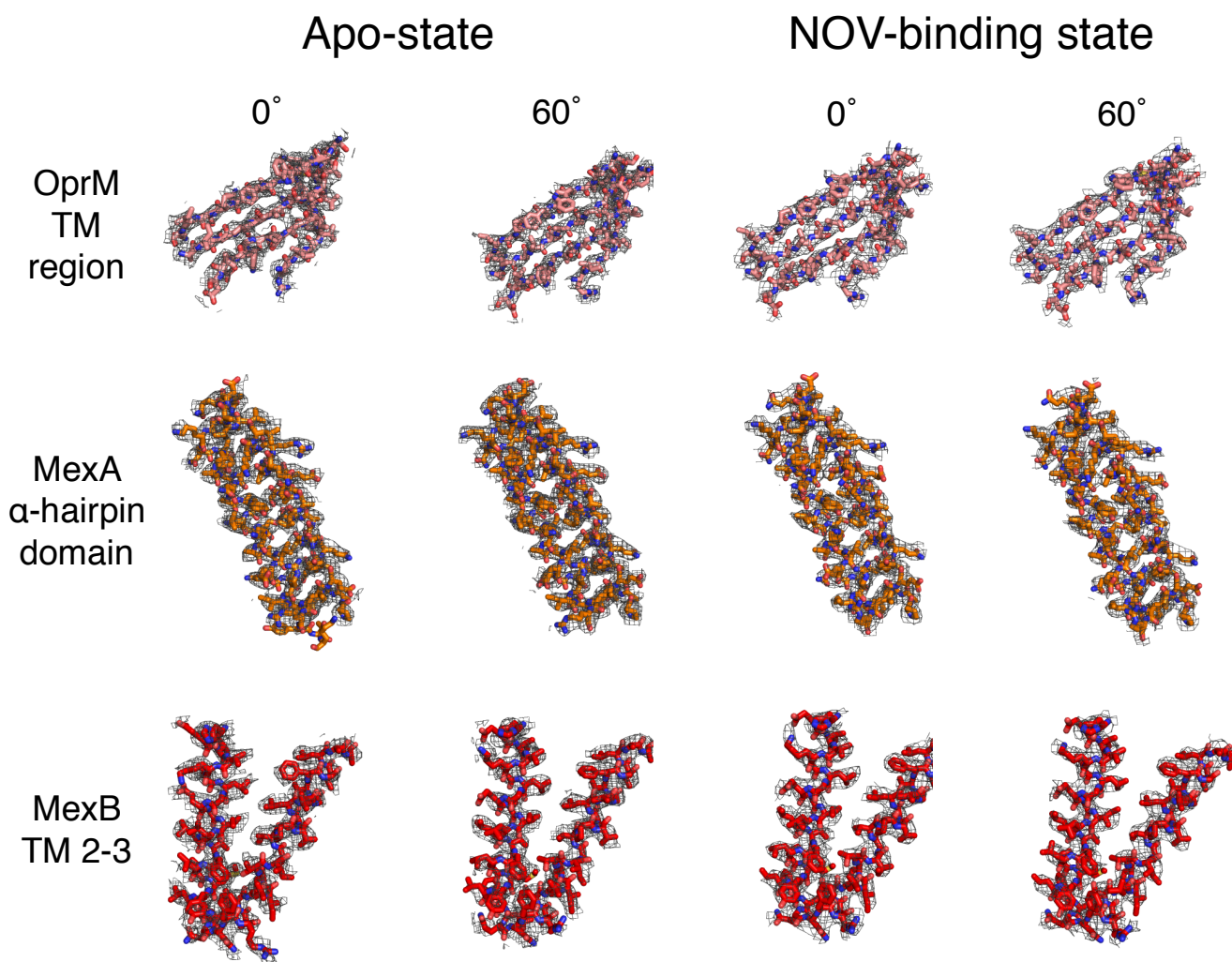
Representative images of serial dilutions of cells plated on LB agar supplemented with 100 µg/mL of ABPC and an additional antibiotic: none (A), CP (B), NOV (C), EM (D), MINO (E), or R6G (F). The top panels indicate residues in MexA which are mutated.

A



Supplementary Figure 3 Sequence alignment of multidrug efflux pumps

Sequence alignment of RND (A), MFP (B), and OMF (C) by Clustal Omega⁹⁵. Conserved residues are marked with magenta. Residues whose side chains are interact with other components are shown in blue. Residues whose main chains interact with other components are shown magenta. Residues marked with green and connectors represent interactions between the corresponding proteins. Yellow residues with connectors represent interactions within a protein. Gray markers represent residues that form the LC protomer–MexB interaction surface.



Supplementary Figure 4 Representative Cryo-EM maps and fitted models

Top panel: β -barrel domain in OprM (a.a. 87–96, 114–127, 299–310, and 321–331). Middle panel: α -hairpin domain in MexA (73–136). Bottom panel: transmembrane helixes 2 and 3 in MexB (a.a. 338–385). The two left columns show segments from the apo-state structure, and the two right columns show segments from the NOV-binding state structure. Leftmost and middle right columns represent the 0° state structure, and middle left and rightmost columns represent the 60° state structure.

References

1. Brenner, S. & Horne, R. W. A NEGATIVE STAINING METHOD FOR HIGH RESOLUTION. *B. B. A.* **34**, 103–110 (1959).
2. Henderson, R. & Unwin, P. N. T. Three-dimensional model of purple membrane obtained by electron microscopy. *Nature* **257**, 28–32 (1975).
3. Henderson, R. *et al.* Model for the Structure of Bacteriorhodopsin Based on High-resolution Electron Cryo-microscopy. *J. Mol. Biol.* **213**, 899–929 (1990).
4. Kenneth, A. T. & Robert, M. G. Electron Microscopy of Frozen Hydrated Biological Specimens. *J. Ultrastruct. Res.* **456**, 448–456 (1976).
5. Dubochet, J., Freeman, R. & Berriman, J. A. Electron microscopy of frozen water and aqueous solutions. *J. Microsc.* **128**, 219–237 (1982).
6. Wade, R. H. A brief look at imaging and contrast transfer. *Ultramicroscopy* **46**, 145–156 (1992).
7. Frank, J. AVERAGING OF LOW EXPOSURE ELECTRON MICROGRAPHS OF NON-PERIODIC OBJECTS. *Ultramicroscopy* **1**, 159–162 (1975).
8. Penczek, P., Radermacher, M. & Frank, J. Three-dimensional reconstruction of single particles embedded in ice. *Ultramicroscopy* **40**, 33–53 (1992).
9. Hoppe, W., Schramm, H. J., Sturm, M., Hunsmann, N. & Gaßmann, J. Three-Dimensional Electron Microscopy of Individual Biological Objects Part I . Methods. *Z. Naturforschdi.* **31a**, 645–655 (1976).

10. Mancini, E. J. *et al.* Cryo-Electron Microscopy Reveals the Functional Organization of an Enveloped Virus , Semliki Forest Virus. *Mol. Cell* **5**, 255–266 (2000).
11. Sachse, C. *et al.* High-resolution Electron Microscopy of Helical Specimens : A Fresh Look at Tobacco Mosaic Virus. *J. Mol. Biol.* **371**, 812–835 (2007).
12. Matadeen, R. *et al.* The Escherichia coli large ribosomal subunit at 7 . 5 Å resolution. *Structure* **7**, 1575–1583 (1999).
13. Connell, S. R. *et al.* Structure of the ribosome-bound cricket paralysis virus IRES RNA. *Nat. Struct. Mol. Biol.* **13**, 1092–1096 (2006).
14. Yu, X., Jin, L. & Zhou, Z. H. 3.88 Å structure of cytoplasmic polyhedrosis virus by cryo-electron microscopy. *Nature* **453**, 415–420 (2008).
15. Maki-yonekura, S., Yonekura, K. & Namba, K. Conformational change of flagellin for polymorphic supercoiling of the flagellar filament. *Nat. Struct. Mol. Biol.* **17**, 417–422 (2010).
16. Veessler, D. *et al.* Maximizing the potential of electron cryomicroscopy data collected using direct detectors. *J. Struct. Biol.* **184**, 193–202 (2013).
17. Scheres, S. H. W. A bayesian view on cryo-EM structure determination. *J. Mol. Biol.* **415**, 406–418 (2012).
18. Bartesaghi, A. *et al.* Atomic Resolution Cryo-EM Structure of Article Atomic Resolution Cryo-EM Structure of β-Galactosidase. *Struct. Des.* **26**, 848–856.e3 (2018).

19. Forsberg, O., Kimanius, D., Zivanov, J. & Nakane, T. New tools for automated high-resolution cryo-EM structure determination in RELION-3. *Elife* **7**, 1–22 (2018).
20. Merk, A. *et al.* Breaking Cryo-EM Resolution Barriers to Facilitate Article Breaking Cryo-EM Resolution Barriers to Facilitate Drug Discovery. *Cell* **165**, 1698–1707 (2016).
21. Bai, X. *et al.* An atomic structure of human γ -secretase. *Nature* **525**, 212–217 (2015).
22. Zernike, F. PHASE CONTRAST, A NEW METHOD MICROSCOPIC OBSERVATION OF TRANSPARENT OBJECTS. *Physica* **9**, 686–698 (1942).
23. Danev, R., Buijsse, B., Khoshouei, M., Plitzko, J. M. & Baumeister, W. Volta potential phase plate for in-focus phase contrast transmission electron microscopy. *Proc. Natl. Acad. Sci.* **111**, 15635–15640 (2014).
24. Khoshouei, M., Radjainia, M., Baumeister, W. & Danev, R. determined with the Volta phase plate. *Nat. Commun.* **8**, 1–6 (2017).
25. Kamgang, B. *et al.* A Newly Isolated Reovirus Has the Simplest Genomic and Structural Organization of Any Reovirus. *J. Virol.* **89**, (2015).
26. Grimes, J. M. *et al.* The atomic structure of the bluetongue virus core. *Nature* **395**, 470–478 (1998).
27. Reinisch, K. M., Nibert, M. L. & Harrison, S. C. Structure of the reovirus core at 3.6 Å resolution. *Nature* **404**, 960–967 (2000).

28. Nakagawa, A. *et al.* The Atomic Structure of Rice dwarf Virus Reveals the Self-Assembly Mechanism of Component Proteins. *Structure* **11**, 1227–1238 (2003).
29. Yu, X., Ge, P., Jiang, J., Atanasov, I. & Zhou, Z. H. Atomic Model of CPV Reveals the Mechanism Used by This Single-Shelled Virus to Economically Carry Out Functions Conserved in Multishelled Reoviruses. *Struct. Des.* **19**, 652–661 (2011).
30. Zhang, X. *et al.* Near-atomic resolution using electron cryomicroscopy and single-particle reconstruction. *Proc. Natl. Acad. Sci.* **105**, 1867–1872 (2008).
31. Hill, C. L. *et al.* The structure of a cypovirus and the functional organization of dsRNA viruses. *Nat. Struct. Mol. Biol.* **6**, 565–568 (1999).
32. Miyazaki, N. *et al.* Structural Evolution of Reoviridae Revealed by Oryzavirus in Acquiring the Second Capsid Shell. *J. Virol.* **82**, 11344–11353 (2008).
33. Okamoto, K. *et al.* The infectious particle of insect- borne totivirus-like Omono River virus has raised ridges and lacks fibre complexes. *Sci. Rep.* **6**, 1–14 (2016).
34. Ghabrial, S. A. Origin , Adaptation and Evolutionary Pathways of Fungal Viruses. *Virus Genes* **16**, 119–131 (1998).
35. Fichorova, R. N. & Nibert, M. L. Trichomonasvirus : a new genus of protozoan viruses in the family Totiviridae. *Arch. Virol.* **156**, 171–179 (2011).
36. Hagiwara, Y. *et al.* Subcellular localization of host and viral proteins associated with tobamovirus RNA replication. *EMBO J.* **22**, (2003).

37. Miyazaki, N. *et al.* Transcapsidation and the Conserved Interactions of Two Major Structural Proteins of a Pair of Phytoreoviruses Confirm the Mechanism of Assembly of the Outer Capsid Layer. *J. Mol. Biol.* **345**, 229–237 (2005).
38. McClain, B., Settembre, E., Temple, B. R. S., Bellamy, A. R. & Harrison, S. C. X-ray Crystal Structure of the Rotavirus Inner Capsid Particle at 3 . 8 Å Resolution. *J. Mol. Biol.* **397**, 587–599 (2010).
39. Iwasaki, K. *et al.* Pleomorphic Configuration of the Trimeric Capsid Proteins of Rice dwarf virus that Allows Formation of Both the Outer Capsid and Tubular Crystals. *J. Mol. Biol.* **383**, 252–265 (2008).
40. Wu, B. *et al.* Phytoreovirus T = 1 Core Plays Critical Roles in Organizing the Outer Capsid of T = 13 Quasi-equivalence. *Virology* **25**, 18–25 (2000).
41. ELIZABETH, A. H., TIMOTHY, F. B., PETER, T. L. & Roy, P. Three-Dimensional Reconstruction of Baculovirus Expressed Bluetongue Virus Core-like Particles by Cryo-Electron Microscopy. *Virology* **189**, (1992).
42. Zhu, Y., Hemmings, A. M., Iwasaki, K., Isogai, M. & Omura, T. Details of the Arrangement of the Outer Capsid of Rice Dwarf Phytoreovirus , as Visualized by Two-Dimensional Crystallography. **71**, 8899–8901 (1997).
43. Lepault, J. *et al.* Structural polymorphism of the major capsid protein of rotavirus. *EMBO J.* **20**, 1498–1507 (2001).
44. Petitpas, I. *et al.* Crystallization and Preliminary X-Ray Analysis of Rotavirus Protein VP6. *J. Virol.* **72**, 7615–7619 (1998).

45. Nakagawa, A., Miyazaki, N. & Higashiura, A. Hierarchical structure assembly model of rice dwarf virus particle formation. *Biophys. Rev.* **10**, 659–665 (2018).
46. Danev, R. & Nagayama, K. Transmission electron microscopy with Zernike phase plate. *Ultramicroscopy* **88**, 243–252 (2001).
47. Takahashi, Y., Tomiyama, M., Hibino, H. & Omura, T. Conserved primary structures in core capsid proteins and reassembly of core particles and outer capsids between rice gall dwarf and rice dwarf phyto-reoviruses. *J. Gen. Virol.* **75**, 269–275 (1994).
48. Omura, T., Morikawa, T., Inoue, H. & Y., S. Purification and Some Properties of Rice Gall Dwarf Virus, a New Phyto-reovirus. *Phytopathology* **72**, 1246–1249 (1982).
49. Cinelli, R. A. G. *et al.* The Enhanced Green Fluorescent Protein as a Tool for the Analysis of Protein Dynamics and Localization : Local Fluorescence Study at the Single-molecule Level. *Photochem. Photobiol.* **71**, 771–776 (2000).
50. Schneider, C. A., Rasband, W. S. & Eliceiri, K. W. NIH Image to ImageJ : 25 years of Image Analysis. *Nat. Methods* **9**, 671–675 (2012).
51. Hohn, M. *et al.* SPARX , a new environment for Cryo-EM image processing. *J. Struct. Biol.* **157**, 47–55 (2007).
52. Tang, G. *et al.* EMAN2 : An extensible image processing suite for electron microscopy. *J. Struct. Biol.* **157**, 38–46 (2007).
53. Mindell, J. A. & Grigorieff, N. Accurate determination of local defocus and specimen tilt in electron microscopy. *J. Struct. Biol.* **142**, 334–347 (2003).

54. Scheres, S. H. W. RELION : Implementation of a Bayesian approach to cryo-EM structure determination. *J. Struct. Biol.* **180**, 519–530 (2012).
55. Grigorieff, N. & Harrison, S. C. Near-atomic resolution reconstructions of icosahedral viruses from electron cryo-microscopy. *Curr. Opin. Struct. Biol.* **21**, 265–273 (2011).
56. Zheng, S. Q. *et al.* MotionCor2: Anisotropic correction of beam-induced motion for improved cryo-electron microscopy. *Nat. Methods* **14**, 331–332 (2017).
57. Zhang, K. Gctf: Real-time CTF determination and correction. *J. Struct. Biol.* **193**, 1–12 (2016).
58. Kimanius, D., Forsberg, B. O., Scheres, S. H. W. & Lindahl, E. Accelerated cryo-EM structure determination with parallelisation using GPUS in RELION-2. *Elife* **5**, 1–21 (2016).
59. Kucukelbir, A., Sigworth, F. J. & Tagare, H. D. Quantifying the local resolution of cryo-EM density maps. *Nat. Methods* **11**, 63–65 (2014).
60. Hagiwara, K. *et al.* The Amino-Terminal Region of Major Capsid Protein P3 Is Essential for Self-Assembly of Single-Shelled Core-Like Particles of Rice Dwarf Virus. *J. Virol.* **78**, 3145–3148 (2004).
61. Hosokawa, F., Danev, R., Arai, Y. & Nagayama, K. Transfer doublet and an elaborated phase plate holder for 120 kV electron-phase microscope. *J. Electron Microsc. (Tokyo)*. **54**, 317–324 (2005).

62. Symmons, M. F., Marshall, R. L. & Bavro, V. N. Architecture and roles of periplasmic adaptor proteins in tripartite efflux assemblies. *Front. Microbiol.* **6**, 1–20 (2015).
63. Delmar, J. A., Su, C.-C. & Yu, E. W. Bacterial Multidrug Efflux Transporters. *Annu. Rev. Biophys.* **43**, 93–117 (2014).
64. Venter, H., Mowla, R., Ohene-Agyei, T. & Ma, S. RND-type drug efflux pumps from Gram-negative bacteria: Molecular mechanism and inhibition. *Front. Microbiol.* **6**, 1–11 (2015).
65. Poole, K. Efflux-mediated multiresistance in Gram-negative bacteria. *Clin. Microbiol. Infect.* **10**, 12–26 (2004).
66. Schweizer, H. P. Efflux as a mechanism of resistance to antimicrobials in *Pseudomonas aeruginosa* and related bacteria: unanswered questions. *Genet Mol Res* **2**, 48–62 (2003).
67. Li, X. Z., Nikaido, H. & Poole, K. Role of MexA-MexB-OprM in antibiotic efflux in *Pseudomonas aeruginosa*. *Antimicrob. Agents Chemother.* **39**, 1948–1953 (1995).
68. Akama, H. *et al.* Crystal structure of the membrane fusion protein, MexA, of the multidrug transporter in *Pseudomonas aeruginosa*. *J. Biol. Chem.* **279**, 25939–25942 (2004).
69. Symmons, M. F., Bokma, E., Koronakis, E., Hughes, C. & Koronakis, V. The assembled structure of a complete tripartite bacterial multidrug efflux pump. *Proc. Natl. Acad. Sci.* **106**, 7173–7178 (2009).

70. Sennhauser, G., Bukowska, M. A., Briand, C. & Grütter, M. G. Crystal Structure of the Multidrug Exporter MexB from *Pseudomonas aeruginosa*. *J. Mol. Biol.* **389**, 134–145 (2009).
71. Nakashima, R. *et al.* Structural basis for the inhibition of bacterial multidrug exporters. *Nature* **500**, 102–106 (2013).
72. Akama, H. *et al.* Crystal structure of the drug discharge outer membrane protein, OprM, of *Pseudomonas aeruginosa*: Dual modes of membrane anchoring and occluded cavity end. *J. Biol. Chem.* **279**, 52816–52819 (2004).
73. Phan, G. *et al.* Structural and Dynamical Insights into the Opening Mechanism of *P. aeruginosa* OprM Channel. *Structure* **18**, 507–517 (2010).
74. Murakami, S., Nakashima, R., Yamashita, E., Matsumoto, T. & Yamaguchi, A. Crystal structures of a multidrug transporter reveal a functionally rotating mechanism. *Nature* **443**, 173–179 (2006).
75. Su, C.-C. *et al.* Structures and transport dynamics of a *Campylobacter jejuni* multidrug efflux pump. *Nat. Commun.* **8**, 171 (2017).
76. Du, D. *et al.* Structure of the AcrAB-TolC multidrug efflux pump. *Nature* **509**, 512–515 (2014).
77. Jeong, H. *et al.* Pseudoatomic Structure of the Tripartite Multidrug Efflux Pump AcrAB-TolC Reveals the Intermeshing Cogwheel-like Interaction between AcrA and TolC. *Structure* **24**, 272–276 (2016).
78. Wang, Z. *et al.* An allosteric transport mechanism for the AcrAB-TolC multidrug efflux pump. *Elife* **6**, 1–19 (2017).

79. Daury, L. *et al.* Tripartite assembly of RND multidrug efflux pumps. *Nat. Commun.* **7**, 1–8 (2016).
80. Scheres, S. H. W. *Processing of Structurally Heterogeneous Cryo-EM Data in RELION. Methods in Enzymology* **579**, (Elsevier Inc., 2016).
81. Singharoy, A. *et al.* Molecular dynamics-based refinement and validation for sub-5 Å cryo-electron microscopy maps. *Elife* **5**, 1–32 (2016).
82. Pettersen, E. F. *et al.* UCSF Chimera - A visualization system for exploratory research and analysis. *J. Comput. Chem.* **25**, 1605–1612 (2004).
83. Afonine, P. V. *et al.* Real-space refinement in PHENIX for cryo-EM and crystallography. *Acta Crystallogr. Sect. D Struct. Biol.* **74**, 531–544 (2018).
84. Adams, P. D. *et al.* PHENIX: A comprehensive Python-based system for macromolecular structure solution. *Acta Crystallogr. Sect. D Biol. Crystallogr.* **66**, 213–221 (2010).
85. Jakobi, A. J., Wilmanns, M. & Sachse, C. Model-based local density sharpening of cryo-EM maps. *Elife* **6**, 1–26 (2017).
86. Emsley, P., Lohkamp, B., Scott, W. G. & Cowtan, K. Features and development of Coot. *Acta Crystallogr. Sect. D Biol. Crystallogr.* **66**, 486–501 (2010).
87. Tribet, C., Audebert, R. & Popot, J.-L. Amphipols: Polymers that keep membrane proteins soluble in aqueous solutions. *Proc. Natl. Acad. Sci.* **93**, 15047–15050 (1996).

88. Xu, Y. *et al.* The tip region of the MacA α -hairpin is important for the binding to TolC to the Escherichia coli MacAB-TolC pump. *Biochem. Biophys. Res. Commun.* **394**, 962–965 (2010).
89. Kim, H. M. *et al.* Functional relationships between the AcrA hairpin tip region and the TolC aperture tip region for the formation of the bacterial tripartite efflux pump AcrAB-TolC. *J. Bacteriol.* **192**, 4498–4503 (2010).
90. Xu, Y. *et al.* Functional implications of an intermeshing cogwheel-like interaction between TolC and MacA in the action of macrolide-specific efflux pump MacAB-TolC. *J. Biol. Chem.* **286**, 13541–13549 (2011).
91. Xu, Y. *et al.* Funnel-like hexameric assembly of the periplasmic adapter protein in the tripartite multidrug efflux pump in gram-negative bacteria. *J. Biol. Chem.* **286**, 17910–17920 (2011).
92. Xu, Y. *et al.* Assembly and channel opening of outer membrane protein in tripartite drug efflux pumps of gram-negative bacteria. *J. Biol. Chem.* **287**, 11740–11750 (2012).
93. López, C. A., Travers, T., Pos, K. M., Zgurskaya, H. I. & Gnanakaran, S. Dynamics of Intact MexAB–OprM Efflux Pump: Focusing on the MexA–OprM Interface. *Sci. Rep.* **7**, 1–17 (2017).
94. Yum, S. *et al.* Crystal Structure of the Periplasmic Component of a Tripartite Macrolide-Specific Efflux Pump. *J. Mol. Biol.* **387**, 1286–1297 (2009).
95. Sievers, F. & Higgins, D. G. Clustal Omega. *Curr. Protoc. Bioinforma.* **2014**, 3.13.1–3.13.16 (2014).

96. Chovancova, E. *et al.* CAVER 3.0: A Tool for the Analysis of Transport Pathways in Dynamic Protein Structures. *PLoS Comput. Biol.* **8**, 23–30 (2012).

List of publications

Nakamichi, Y., Miyazaki, N., Tsutsumi, K., Higashiura, A., Narita, H., Murata, K. and Nakagawa, A. An assembly intermediate structure of Rice dwarf virus reveals a hierarchical outer capsid shell assembly mechanism. *Structure*. (in press)

Tsutsumi, K., Yonehara, R., Ikeda, E., Miyazaki, N., Maeda, S., Iwasaki, K., Nakagawa, A. and Yamashita, E. Structures of the wild-type MexAB–OprM tripartite pump reveal its complex formation and drug efflux mechanism. (under submission)